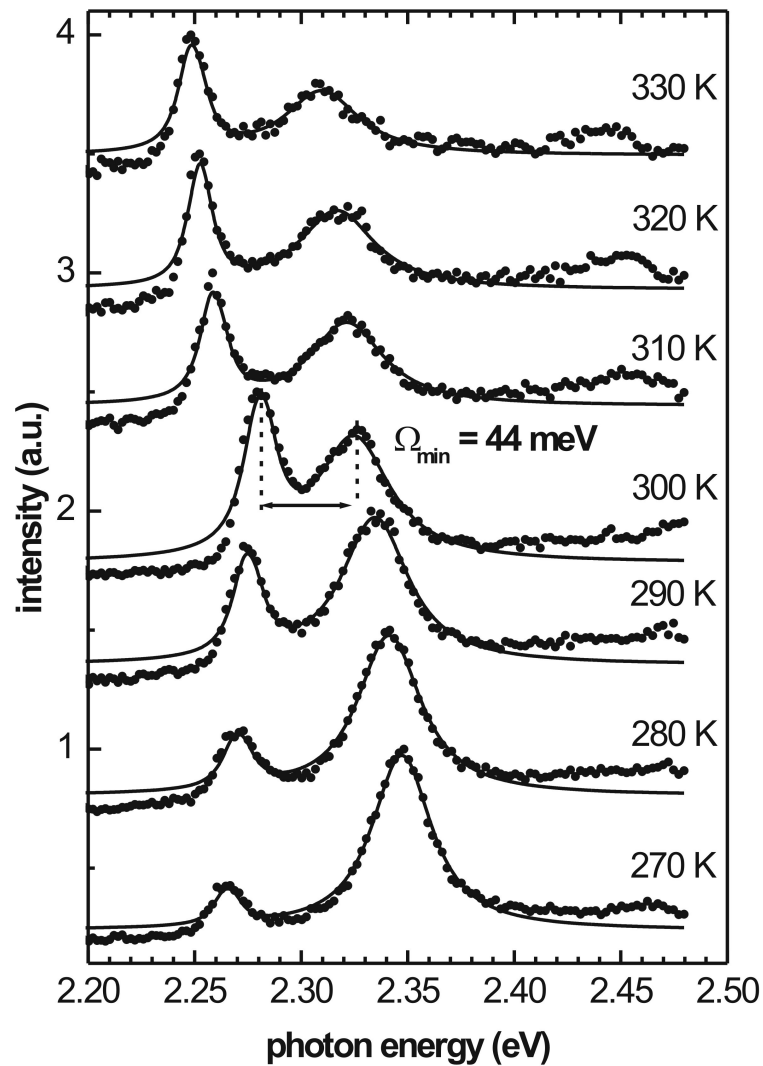


# Development and investigation of II-VI semiconductor microcavity structures



Alexander Pawlis

Amelgatzen, im Dezember 2003



# Development and investigation of II-VI semiconductor microcavity structures

Von der Fakultät für Naturwissenschaften  
der Universität Paderborn  
zur Erlangung des akademischen Grades eines

Doktor der Naturwissenschaften

genehmigte

**Dissertation**

von

**Alexander Pawlis**

Amelgatzen, im Dezember 2003



## Abstract

Due to the strong coupling interaction between photon and exciton in semiconductor microcavities, two new quantum mechanical eigenstates, the so-called polariton states are manifested and show extraordinary optical properties. One of these properties is an "anti-crossing" behavior of the coupled polariton dispersion with a minimum energy difference, the Rabi-splitting energy  $\Omega_{Rabi}$ , which is observed in the resonance between photon and exciton.

In this thesis I report on the observation and investigation of strong coupling between photonic and excitonic modes in ZnSe/(Zn,Cd)Se multi quantum well microcavities. The active layer, which is a ZnSe/(Zn,Cd)Se quantum structure, is grown by molecular beam epitaxy. The results of the optimization of crystallographical and optical properties of the ZnSe/(Zn,Cd)Se quantum structure as well as the implementation of a cavity length gradient are discussed in detail. The active layer is covered with polycrystalline dielectric Bragg-mirrors of ZnS/YF<sub>3</sub> or ZnSe/YF<sub>3</sub> and a high reflectivity  $R > 0.995$  in the blue and green spectral range is achieved.

A large room temperature Rabi-splitting energy of  $\Omega > 35$  meV has been measured in microcavities containing four ZnSe/(Zn,Cd)Se quantum wells as active layers. The "anti-crossing" behavior of the polariton modes has been demonstrated by reflectivity as well as photoluminescence investigations.

Therefore two different methods of microcavity resonance tuning have been performed. In reflectivity measurements the photonic mode has been tuned in resonance with the excitonic mode by varying the spot position on the sample in direction of the microcavity length gradient. In contrast to this, in temperature-dependent photoluminescence measurements the polariton dispersion is obtained by modifying the resonance condition between excitonic and photonic mode via the temperature shift of the quantum well transition energy.

All experimental results are in good agreement with the calculated polariton properties based on the quantum electrodynamical model of a coupled photon-exciton oscillator.



# Contents

<b>1</b>	<b>Introduction</b>	<b>11</b>
<b>2</b>	<b>Exciton-photon interaction in semiconductor microcavity structures</b>	<b>15</b>
2.1	Excitons in strongly coupled microcavities . . . . .	15
2.1.1	Strong and weak coupling in atomic cavities . . . . .	17
2.1.2	Strong coupling in quantum well microcavities . . . . .	18
2.1.3	Polariton dispersion – effective mass model for a coupled oscillator .	19
2.2	Simulation of the optical response of a microcavity . . . . .	21
2.2.1	The Transfer-Matrix model for a single layer . . . . .	21
2.2.2	Calculation of the complex refractive index dispersion . . . . .	22
2.3	Resonance tuning of microcavities to obtain the polariton dispersion . . . .	25
2.3.1	Angular dependent microcavity detuning . . . . .	25
2.3.2	Microcavity detuning with a cavity length gradient . . . . .	25
2.3.3	Temperature detuning in microcavity structures . . . . .	26
<b>3</b>	<b>Distributed Bragg-mirrors for II-VI microcavities</b>	<b>29</b>
3.1	Optical properties of ZnS/YF <sub>3</sub> dielectric Bragg-mirrors . . . . .	30
3.1.1	Structural properties of ZnS/YF <sub>3</sub> DBRs . . . . .	33
3.2	ZnSe and YF <sub>3</sub> Bragg-Mirrors . . . . .	37
3.2.1	Optical properties of ZnSe/YF <sub>3</sub> DBRs . . . . .	37
3.2.2	Structural properties of ZnSe/YF <sub>3</sub> Bragg-mirrors . . . . .	40

<b>4</b>	<b>ZnSe and (Zn,Cd)Se quantum structures for II-VI microcavities</b>	<b>45</b>
4.1	In-situ growth characterization of ZnSe/(Zn,Cd)Se quantum structures . . .	46
4.2	Investigation of (Zn,Cd)Se multi quantum wells . . . . .	49
4.2.1	Structural investigations of MQWs . . . . .	50
4.2.2	Optical properties of ZnSe/(Zn,Cd)Se MQWs . . . . .	57
4.3	ZnSe/(Zn,Cd)Se superlattice structures . . . . .	59
4.3.1	Structural properties of superlattice structures . . . . .	61
4.3.2	Photoluminescence investigation of SL structures . . . . .	68
<b>5</b>	<b>II-VI semiconductor microcavity structures</b>	<b>71</b>
5.1	The combination of Bragg-mirrors and active layer to complete microcavities	71
5.1.1	Experimental growth procedure of microcavity structures . . . . .	72
5.2	Investigation of a SL microcavity structure with ZnSe/YF <sub>3</sub> DBRs . . . . .	75
5.2.1	Measurement of the microcavity length gradient off-resonance . . . . .	76
5.2.2	Reflectivity measurements in resonance condition . . . . .	76
5.3	Room temperature Rabi-splitting in a MQW microcavity with ZnS/YF <sub>3</sub> DBRs . . . . .	81
5.3.1	Photoluminescence investigations of the MQW microcavity in res- onance condition . . . . .	84
5.3.2	Reflectivity measurements of the MQW-microcavity in resonance condition . . . . .	87
5.3.3	Calculation of the QW oscillator strength per unit area . . . . .	91
<b>6</b>	<b>Conclusions</b>	<b>93</b>
<b>7</b>	<b>Appendix</b>	<b>109</b>

# List of Abbreviations

<b>AFM</b>	<u>A</u> tom <u>i</u> c <u>F</u> orce <u>M</u> icroscopy
<b>BEP</b>	<u>B</u> eam <u>E</u> quivalent <u>P</u> ressure
<b>DBR</b>	<u>D</u> istributed <u>B</u> r <u>a</u> gg- <u>R</u> eflector
<b>FWHM</b>	<u>F</u> ull <u>W</u> idth at <u>H</u> alf <u>M</u> aximum
<b>LD</b>	<u>L</u> aser <u>D</u> iode
<b>LED</b>	<u>L</u> ight <u>E</u> mitting <u>D</u> evice
<b>MBE</b>	<u>M</u> olecular <u>B</u> eam <u>E</u> pitaxy
<b>ML</b>	<u>M</u> onolayer
<b>MQW</b>	<u>M</u> ulti <u>Q</u> uantum <u>W</u> ell
<b>MSEO</b>	<u>M</u> odified <u>S</u> ingle <u>E</u> ffective <u>O</u> scillator
<b>PL</b>	<u>P</u> hotoluminescence
<b>QD</b>	<u>Q</u> uantum <u>D</u> ot
<b>QW</b>	<u>Q</u> uantum <u>W</u> ell
<b>RHEED</b>	<u>R</u> election <u>H</u> igh <u>E</u> nergy <u>E</u> lectron <u>D</u> iffraction
<b>RMS</b>	<u>R</u> oot <u>M</u> ean <u>S</u> quare
<b>SL</b>	<u>S</u> uperlattice
<b>TE</b>	<u>T</u> ransversal- <u>E</u> lectric
<b>TEM</b>	<u>T</u> ransmission <u>E</u> lectron <u>M</u> icroscopy
<b>TM</b>	<u>T</u> ransversal- <u>M</u> agnetic
<b>UHV</b>	<u>U</u> ltra <u>H</u> igh <u>V</u> acuum
<b>VCSEL</b>	<u>V</u> ertical <u>C</u> avity <u>S</u> urface <u>E</u> mitting <u>L</u> aser



# 1 Introduction

Semiconductor QWs as part of microcavities allow to study the interconversion between excitons and photons, which in the strong coupling regime is manifested as a Rabi-splitting into two resonance features of the optical spectrum. The coupling between excitons and photons generates new quasi-particles known as polaritons. These particles have some extraordinary properties, which open up the possibility to develop new types of efficient light emitters or quantum processors [Ge1998, Ba2002].

After the first observation of polariton splitting in a Fabry-Perot microcavity (Weisbuch et. al. 1992) [We1992, We2000], the strong coupling regime of QW excitons was studied by various spectroscopy methods in III-V semiconductor microcavities with epitaxial grown DBRs [Kh1999, Bl1998] based on GaAs, AlAs and their alloys. Because the exciton binding energy as well as the oscillator strength of GaAs and its related materials is very small, most of the studies according to polariton effects are limited to the low temperature region up to 100 K. Some efforts have been performed to achieve strong coupling in III-V microcavities at room temperature in complicated microcavities containing up to 30 GaAs/(Al,Ga)As QWs, yielding a Rabi-splitting about 8 meV [Di2001].

For room temperature applications the Rabi-splitting must exceed the thermal energy of about 25 meV. Since the Rabi-splitting depends on the oscillator strength and the exciton binding energy, this condition is excellently satisfied with II-VI semiconductor based quantum structures.

André et al. [An2000] investigated CdTe MQW structures enclosed in (Cd,Mg)Te/(Cd,Mn)Te semiconductor Bragg-mirrors and achieved Rabi-splitting energies between 12 meV and

30 meV in microcavities containing up to 16 CdTe QWs. Kelkar et al. [Ke1995] reported a Rabi-splitting of 17.5 meV at 70 K and 10 meV at 175 K in a (Zn,Mg)(S,Se) microcavity with three (Zn,Cd)Se QWs as the resonant medium and dielectric SiO<sub>2</sub>/TiO<sub>2</sub> Bragg-mirrors.

The discussion about polariton based applications in future devices such as a polariton laser, has been opened up recently by Saba et al. [Sa2002, Ci2002]. They have measured parametric polariton amplification up to 220 K in a CdTe based MQW microcavity. The experimental observations demonstrate that the polariton amplification cut-off temperature is directly related to the exciton binding energy. ZnSe and CdSe combine a large Rabi-splitting energy and a high exciton binding energy up to 40 meV. Therefore ZnSe and (Zn,Cd)Se compounds are particularly suited for microcavity applications such as polariton amplification devices.

This work is focused on the development of semiconductor microcavity structures with ZnSe/(Zn,Cd)Se QWs as the active layer, which are enclosed in distributed Bragg-reflectors of ZnS/YF<sub>3</sub> or ZnSe/YF<sub>3</sub>, respectively. Furthermore such microcavities are investigated with various spectroscopic methods to demonstrate the existence of the strong coupling between photon and exciton at room temperature.

In the first chapter a short introduction is given about the theoretical background of the exciton-photon coupling in atomic as well as semiconductor microcavity structures.

Chapter 2 describes the development of distributed Bragg-reflectors of ZnS/YF<sub>3</sub> and ZnSe/YF<sub>3</sub>, respectively, which are grown by thermal evaporation. Because the maximum reflectivity in these Bragg-mirrors depends mainly on interface quality, surface roughness and refractive index difference, detailed investigations are performed by reflectivity as well as AFM measurements.

The main issue in Chapter 3 is the investigation of different MBE grown ZnSe/(Zn,Cd)Se MQW- and SL structures. I describe the efforts to maximize the number of QWs, which might be enclosed in a small resonator length (about 200 nm) before a significant degen-

---

eration of structural and optical properties of the active layer is observed.

In the last chapter of this thesis, both technologies, the Bragg-mirrors and the quantum structures are combined to complete microcavity structures, to investigate strong coupling effects at room temperature. The anticrossing behavior of the polariton dispersion is measured with different spectroscopic methods of microcavity detuning and a large room temperature Rabi-splitting energy of 40 meV is obtained in a four-fold ZnSe/(Zn,Cd)Se MQW microcavity.



# 2 Exciton-photon interaction in semiconductor microcavity structures

## 2.1 Excitons in strongly coupled microcavities

One of the most important and popular set of applications for semiconductors such as light emitting devices (LEDs and LDs) or photon detectors are based on the interaction of light and matter. When light is incident on a bulk direct band-gap semiconductor, it will be absorbed, if the photon energy is larger than the bandgap energy. Due to this absorption process free electron-hole pairs are generated.

Electron-hole pairs, which are spatially close together, the so-called excitons, are bound by the Coulomb force. The energy and momentum of these quasi-particles in the semiconductor material is conserved. Excitons can be scattered by collision with photons, crystal defects, free carriers or other excitons. The scattering enhances the recombination of electron-hole pairs, which leads to spontaneous photon emission or nonradiative recombination. In this case the excitons interact with a continuum of electromagnetic modes and can emit light in any direction and frequency within the emission linewidth, which results in an exponential decay of the generated excitons [Sa1974, Al1975].

The modification of the electromagnetic environment of a semiconductor exciton increases the possibility of resonant photon-exciton coupling. This can be realized, if the semiconductor is placed into a microcavity as illustrated in Fig. (2.1). In Fig. (2.1 **a.**) photon and exciton are uncoupled. By spontaneous exciton recombination a photon is emitted

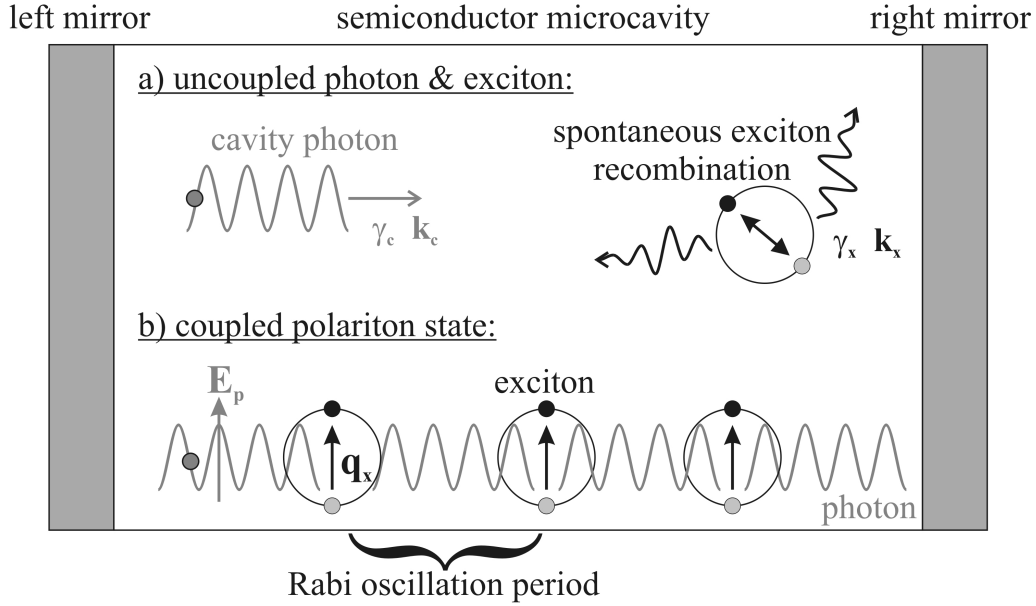


Figure 2.1: Cross-section drawing of a semiconductor microcavity structure. **a.)** The cavity photon with momentum  $k_C$  and linewidth  $\gamma_C$  as well as the exciton with  $k_X$  and  $\gamma_X$  respectively, are uncoupled. By spontaneous exciton recombination, a photon is generated and emitted without a preferred direction. **b.)** The electromagnetic environment of an exciton is modified by a resonantly incident photon. The electric field of the photon manipulates the exciton dipole momentum  $q_X$  and strong coupling occurs. The energy is periodically transferred between photon and exciton. This is manifested in the characteristic Rabi-oscillation frequency. The linear combinations of the photonic and excitonic eigenstates are the polariton modes.

without any preferred direction. The homogenous linewidth  $\gamma_X$  of the exciton transition results from the decay time of the generated radiation field. An uncoupled photon is confined in the microcavity structure and its lifetime is related to the homogenous linewidth  $\gamma_C$  of the resonator.

If the incident light is resonant with the exciton transition, the electric field of the photon interacts with the exciton dipole momentum  $q_X$  and creates an exciton polarization, which has the same  $\omega$  and  $k_C$  as the incident light [No1999]. Hence it follows that the coupled photon-exciton with a given  $\omega$  and  $k$  only can interact with a single mode of the radiation

field and its radiation dynamics is different from light emission of non resonant excitons. This effect is illustrated in Fig. (2.1 **b.**). During the interaction time of light field and exciton the energy oscillates between the given excitonic and photonic eigenstate: A photon is absorbed by the semiconductor and creates an exciton, which re-emits a photon and so on. The energy exchange of the coupled photon-exciton leads to two stationary states with the frequencies  $\omega_{up}$  and  $\omega_{lp}$ , the so-called normal modes, which are the linear combinations of electromagnetic and exciton polarization modes (i.e. the polariton modes) [Ho1958].

### 2.1.1 Strong and weak coupling in atomic cavities

In a microcavity with a single atom inside the occurrence of strong or weak coupling is directly related to the strength of the dipole interaction energy  $g$  as well as the linewidth of photon  $\gamma_C$  and exciton  $\gamma_0$ , respectively. For the case that the dipole interaction  $g < (\gamma_C, \gamma_0)$ , the dipole interaction time to manifest the strong coupling is larger than the decay time of the exciton as well as the lifetime of the photon in the resonator. Hence it follows that the microcavity operates in the weak coupling regime. Due to the modification of the mode density by the cavity confinement, the spontaneous emission is enhanced, if photonic mode and excitonic mode are in resonance and inhibited in the non resonant case [Be1994, Yo1995].

If  $g > (\gamma_C, \gamma_0)$ , the dipole interaction time is smaller than the lifetime of the photon and the decay time of the exciton. Then the microcavity operates in the strong coupling regime featuring the two polariton states with the average linewidth  $\gamma_{\pm} = \frac{1}{2} (\gamma_C + \gamma_0)$  [Ca1989]. If  $\gamma_C < \gamma_0$ , the polariton linewidth  $\gamma_{\pm}$  is smaller than the free space linewidth of the atomic transition and the spontaneous emission is inhibited. On the other hand  $\gamma_C > \gamma_0$  leads to an enhancement of the spontaneous emission.

The Rabi-oscillation frequency  $\Omega_{Rabi}$ , which is proportional to the energy exchange frequency during the strong coupling between the photonic and excitonic quantum state, is directly related to the coupling strength  $\hbar g$  and the frequency splitting between the upper

and lower polariton state  $\omega_{up}$  and  $\omega_{lp}$ ,

$$\Omega_{Rabi} = \omega_{up} - \omega_{lp}. \quad (2.1)$$

The probability of re-absorption of the photon by the atom in the strong coupling regime depends on the number of atoms in the ground state (i.e. the oscillator density). For  $N$  atoms in the microcavity the oscillator strength of the exciton transition is enhanced by a factor of  $N$ . Hence the Rabi-splitting energy  $\Omega_{Rabi}$  will increase by a factor of  $\sqrt{N}$ , which means that the strong coupling regime is achieved more easily with a large oscillator density in the microcavity [No1999]. Due to their increased oscillator density, QW excitons are particularly suited for the investigation of the strong coupling in semiconductor microcavities [We1992].

### 2.1.2 Strong coupling in quantum well microcavities

Due to the large density of oscillators in microcavities with QWs, one photon does not interact any more with one and the same exciton. Therefore the coupling strength is characterized by the QW oscillator strength per unit area  $\frac{f}{S}$ , instead of the dipole interaction  $g$ . Hence it follows that the Rabi-splitting energy  $\hbar\Omega_{Rabi}$  is given by

$$\hbar\Omega_{Rabi} = \hbar\sqrt{\frac{8cN_{QW}\gamma_X}{n_C L_{eff}}}, \quad (2.2)$$

where  $L_{eff} = L_c + L_{DBRs}$  is the effective microcavity length including the penetration depth of the electromagnetic wavefunction into the Bragg-mirrors and  $N_{QW}$  is the number of QWs [Ya2002]. The term

$$\gamma_X = \frac{e^2}{4\varepsilon_0 M_X^* c n_C} \frac{f}{S} \quad (2.3)$$

describes the decay rate of excitons in the QW ground state (i.e. lifetime broadening, similar to  $\gamma_0$  in atomic cavities) and is proportional to the oscillator strength per unit area [Sk1998].

### 2.1.3 Polariton dispersion – effective mass model for a coupled oscillator

In a microcavity containing a single QW, the photon-exciton coupling is described by the  $2 \times 2$  matrix Hamiltonian Eq. (2.4), where  $V = \frac{1}{2} \hbar \Omega_{Rabi}$  is the coupling potential and  $E_X(k)$  and  $E_C(k)$  are the dispersion relations (based on the effective mass model) of uncoupled exciton and photon, respectively.

$$\mathbf{H} = \begin{pmatrix} E_X(k) & V \\ V & E_C(k) \end{pmatrix} \quad (2.4)$$

The eigenvalues of the coupled oscillators are obtained by diagonalization of the Hamiltonian

$$E_{P\pm} = \frac{E_X(k) + E_C(k)}{2} \pm \frac{1}{2} \sqrt{(\hbar \Omega_{Rabi})^2 + (E_X(k) - E_C(k))^2}. \quad (2.5)$$

The in-plane exciton dispersion  $E_X(k)$  is described by the effective mass model

$$E_X(k) = E_0 + \frac{\hbar^2 k_{\parallel}^2}{2M_X^*}, \quad (2.6)$$

where  $M_X^*$  is the reduced effective mass of the exciton and  $E_0$  the QW ground state transition energy. The  $k_z = \frac{2\pi N}{L_C}$  of the photonic modes are confined by the resonator length  $L_C$  and  $N$  is the mode number. Therefore the photon dispersion in the cavity is given by

$$E_C(k_{\parallel}) = \frac{\hbar c}{n_C} \sqrt{\left(\frac{2\pi N}{L_C}\right)^2 + k_{\parallel}^2}. \quad (2.7)$$

The confined photon may also be associated to an effective mass  $M_C = \frac{\hbar n_C}{c L_C}$ , which is about five orders of magnitude smaller than the exciton effective mass  $M_X^*$  [An2000]. The dispersions of pure photon, pure exciton and the upper and lower polariton are shown in Fig. (2.2). They are calculated for a typical  $\lambda$ -sized (i.e.  $n_C * L_C = \lambda$ ) microcavity structure with one QW in its center and an emission wavelength of  $\lambda = 517$  nm (i.e.  $E_0 = 2.4$  eV).

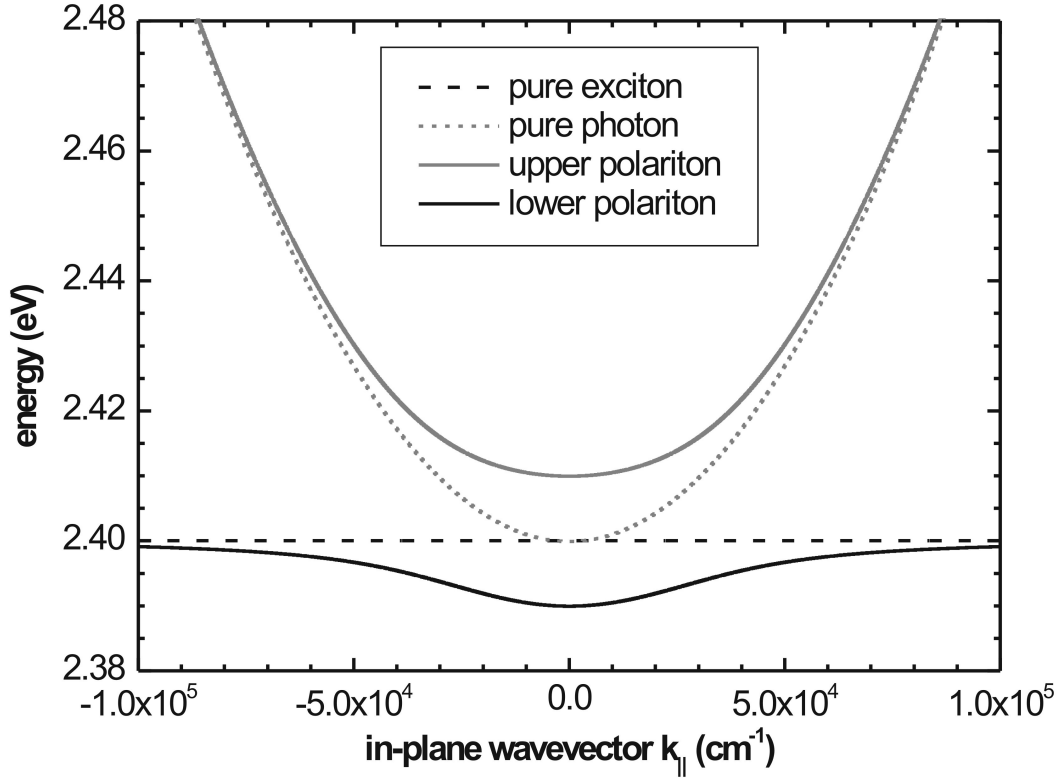


Figure 2.2: Calculated energy dispersion of photon (dotted grey curve), exciton (dashed black curve) and coupled polaritons (full curves in black and grey) as a function of the in-plane cavity wavevector  $k_{||}$ . The pure exciton dispersion is almost flat compared to the pure photon dispersion. Due to the strong coupling between photon and exciton, the degeneracy of both states is lifted near the resonance at  $k_{||} = 0$ . This results in a the splitting between the two polariton branches. The minimum splitting, which is the Rabi-splitting energy  $\hbar\Omega_{Rabi}$ , is obtained in the resonance.

The exciton dispersion is nearly flat on the scale of the photon dispersion. The resonance condition of the photonic and excitonic mode is fulfilled at  $k_{||} = 0$ . For large  $k_{||}$  the upper polariton is almost "excitonlike" and the lower polariton "photonlike", respectively. Near the resonance, the degeneracy of uncoupled photon and exciton is lifted due to the strong coupling interaction potential  $V$  and the anticrossing behavior of the polariton dispersion relation is observed. In the resonance condition the splitting between the polariton modes is minimal, yielding the Rabi-splitting energy  $\hbar\Omega_{Rabi}$ .

## 2.2 Simulation of the optical response of a microcavity

### 2.2.1 The Transfer-Matrix model for a single layer

The optical response of a semiconductor microcavity structure such as reflectivity, absorption and transmission can be calculated with the Transfer-Matrix model, which is based on the boundary conditions of the Maxwell equations. The behavior of an incident plane electromagnetic wave on the boundary between two different materials is illustrated in Fig. (2.3a.) [He1979].

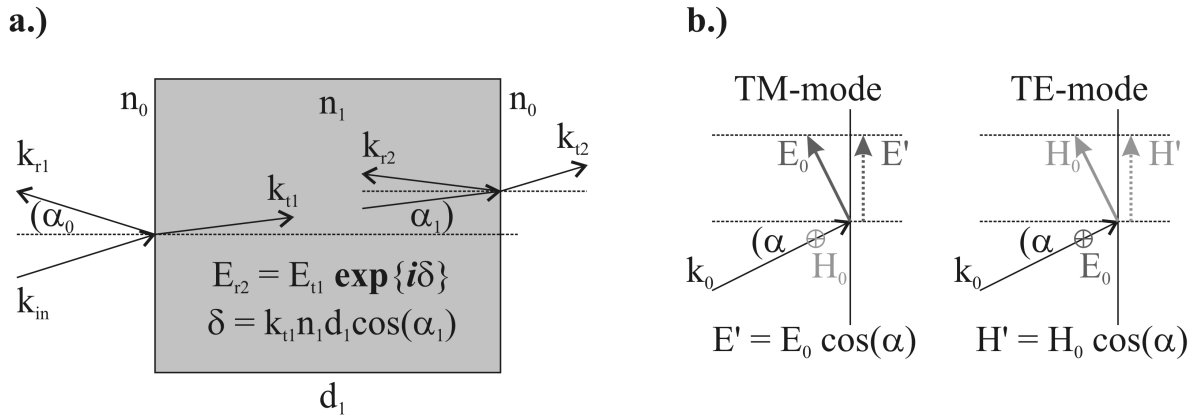


Figure 2.3: **a.)** An incident plane electromagnetic wave with the wavevector  $k_{in}$  is partially reflected and transmitted at the boundaries of a semiconductor material and its environment with the characteristic refractive indices  $n_1$  and  $n_0$ , respectively. During the propagation of the transmitted wave  $k_{t1}$  through the material with the length  $d_1$ , the electric field gets a phase shift  $\delta$ , which depends on the transmission angle  $\alpha_1$  and the refractive index  $n_1$ . **b.)** For variation of  $\alpha$ , the angle of incidence, the electric field of the TM-mode is modified, but the electric field of the TE-mode does not change with  $\alpha$ .

The plane wave with the wavevector  $k_{in}$  is partially reflected and transmitted at the boundaries of a semiconductor with the complex refractive index dispersion  $n_1$  and its surrounding medium  $n_0$ . The transversal component of the electric field must be steady on both sides of the boundaries. During the propagation of the transmitted part of the incident wave  $k_{t1}$  through the medium, the electric field is phase shifted by  $\delta = k_{t1} n_1 d_1 \cos(\alpha_1)$ . This shift depends on the length  $d_1$  and the refractive index  $n_1$  of the

material as well as the transmission angle  $\alpha_1$ . Since the transmission angle is related to the angle of incidence by the refractive law, it is possible to modify the phase shift in the material by variation of the angle of incidence. As shown in Fig. (2.3b.) the TE- and TM-polarization must be treated separately, due to their different symmetry with respect to the incidence angle. The electric field of the TM-mode is angular dependent, while the electric field of the TE-mode does not change with  $\alpha$ .

The electromagnetic field of the transmitted and reflected wave is directly linked to the electromagnetic field of the incident wave by the  $2 \times 2$  Transfer-Matrix  $M$  [Pa2000]

$$\begin{pmatrix} E_{in} \\ H_{in} \end{pmatrix} = \mathbf{M} \times \begin{pmatrix} E_{t2} \\ H_{t2} \end{pmatrix}. \quad (2.8)$$

For the single layer in Fig. (2.3) the characteristic matrix  $\mathbf{M}$  for TE and TM-polarization are defined as

$$\mathbf{M}_{\text{TE}} = \begin{pmatrix} \cos(\delta) & -\frac{\nu}{\gamma_1} \frac{\sin(\delta)}{\cos(\alpha_1)} \\ -\nu\gamma_1 \sin(\delta)\cos(\alpha_1) & \cos(\delta) \end{pmatrix}, \quad (2.9)$$

$$\mathbf{M}_{\text{TM}} = \begin{pmatrix} \cos(\delta) & -\frac{\nu}{\gamma_1} \sin(\delta)\cos(\alpha_1) \\ -\nu\gamma_1 \frac{\sin(\delta)}{\cos(\alpha_1)} & \cos(\delta) \end{pmatrix}, \quad (2.10)$$

where  $\gamma_1 = \sqrt{\frac{\epsilon_0}{\mu_0}} n_1$  describes the dielectric properties of the layer material.

For a typical microcavity structure including Bragg-mirrors and the active layers, each layer is assigned to a characteristic matrix  $\mathbf{M}_i$  and the optical response of the whole system is obtained by multiplying the single layer matrices according to their structural sequence.

## 2.2.2 Calculation of the complex refractive index dispersion

The accuracy of the Transfer-Matrix model to describe multilayer structures depends appreciable on the precise knowledge of the complex refractive index dispersion of the layer materials. All microcavity structures studied in this thesis are based on the materials ZnSe, ZnS and YF<sub>3</sub> for the dielectric mirrors as well as ZnSe/(Zn,Cd)Se QWs in the active

layer and GaAs as the substrate material, respectively. For the II-VI and III-V compounds the modified single effective oscillator (MSEO) method [Af1974] is appropriate for the calculation of the refractive index dispersion below the semiconductor bandgap.

The absorption near the bandgap is not negligible any more, since the typical emission energy of the ZnSe/(Zn,Cd)Se microcavities is between 2.2 eV and 2.6 eV (i.e. 564 nm and 477 nm). Therefore the MSEO method with excitons, which considers an additional broadening effect  $\gamma_X$ , is more appropriate [Ta1997]. In this formulation, the imaginary parts of the complex dielectric constant of the materials are approximated by a delta function with strength  $\frac{1}{2}\pi E_d$  at the energy  $E_0$  [We1971].

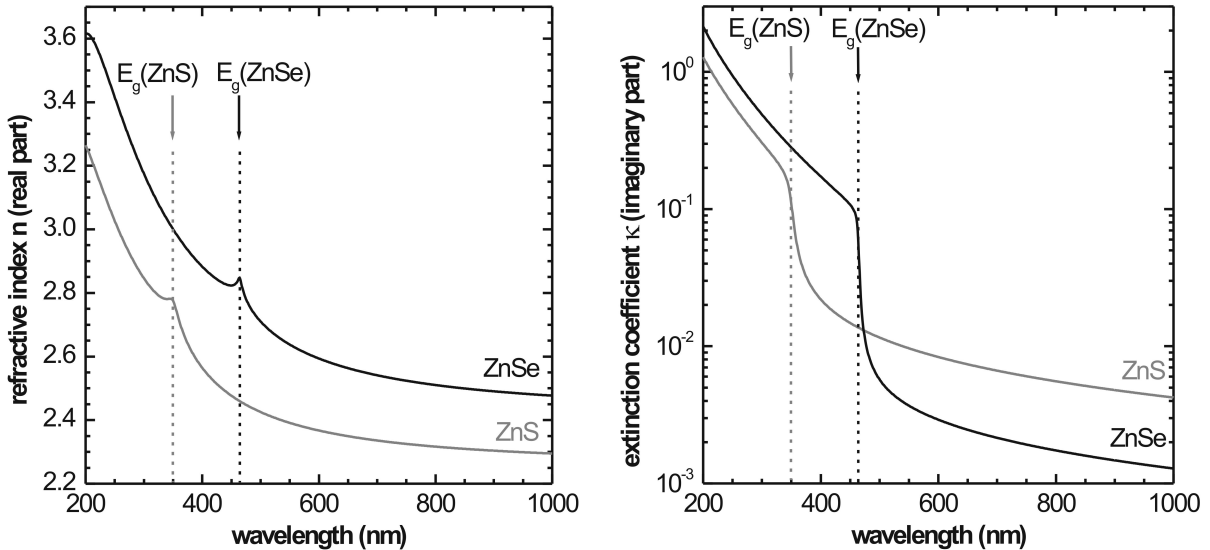


Figure 2.4: Calculated complex dielectric constant of the materials ZnS (grey curves) and ZnSe (black curves) separated in real (left side) and imaginary (right side) parts, respectively. **Left side:** Near the bandgap of the materials the exciton generation is taken into account by a Lorentzian lineshape with the exciton broadening  $\gamma_X$ . **Right side:** The extinction coefficient is modelled by a Delta function. Below the bandgap the absorption of both materials is negligible. The parameters of the complex dielectric constant of the materials are summarized in Tab. (2.1).

Fig. (2.4) shows the calculated refractive index dispersion of ZnS and ZnSe separated into real (left side) and imaginary part (right side). Near the bandgap of the materials the exciton contribution is considered by a Lorentzian lineshape in the real part of the

dielectric function. The absorption also increases near the bandgap. Below the bandgap the extinction coefficient of both materials is smaller than one percent.

material	$E_g$ (eV)	$E_0$ (eV)	$E_d$ (eV)	$\gamma_X$ (meV)
ZnSe	2.67 <sup>(1)</sup>	5.54 <sup>(2)</sup>	27.0 <sup>(2)</sup>	14 <sup>(1)</sup>
ZnS	3.54 <sup>(1)</sup>	6.36 <sup>(2)</sup>	26.1 <sup>(2)</sup>	70 <sup>(1)</sup>
GaAs	1.424 <sup>(1)</sup>	3.55 <sup>(2)</sup>	33.5 <sup>(2)</sup>	35 <sup>(2)</sup>

Table 2.1: Parameters for the calculation of the complex refractive index dispersions of ZnSe, ZnS and GaAs with the modified MSEO method. References: <sup>(1)</sup>experimental fits, this work and <sup>(2)</sup>[We1971].

The parameters for the calculation of the dielectric constant of all the materials, which are used in this thesis, are summarized in Tab. (2.1). The material YF<sub>3</sub> has a large bandgap energy and therefore no strong dispersion. The refractive index dispersion is approximated by

$$n(YF_3) = 1.417 \cdot \exp\left\{\frac{17}{\lambda - 206}\right\} \quad (2.11)$$

and the extinction coefficient is neglected [Pa2000].

For the calculation of the dielectric constant of the (Zn,Cd)Se QWs, the confined exciton contribution is included with a standard Lorentzian oscillator form

$$\epsilon(\omega) = \epsilon_B + \frac{4\pi f_{osz}\omega_0^2}{\omega_0^2 - \omega^2 - i\gamma_X\omega}, \quad (2.12)$$

where  $f_{osz}$  is the oscillator strength and  $\gamma_X$  is the inhomogeneous broadening of the QW transition [Tr1996].  $\omega_0$  is the transition frequency and the background refractive index of the QW material is included by  $\epsilon_B$ . Due to the fact that the QW dispersion is integrated into the Transfer-Matrix model, the light matter interaction between photon and exciton is considered. Hence it is possible to calculate reflectivity, transmission and absorption of a microcavity structure with the Transfer-Matrix model.

## 2.3 Resonance tuning of microcavities to obtain the polariton dispersion

For measurement and calculation of the anticrossing of the polariton dispersion relation in microcavities it is necessary to modify the resonance condition between the photonic and excitonic mode. Actually three methods may be used: Angular detuning, cavity length gradient detuning and temperature detuning, respectively.

### 2.3.1 Angular dependent microcavity detuning

In angular resolved reflectivity measurements the angle of incidence  $\alpha_{in}$  and the angle of detection ( $\alpha_d = -\alpha_{in}$ ) is varied from normal incidence. Due to the fact that the polariton dispersion Eq. (2.5-2.7) is directly related to  $k_{||}$ , a standing wave with a determined in-plane wavevector is excited in the microcavity. With increasing  $\alpha_{in}$  the cavity mode is shifted to higher energy, due to the additional  $k_{||}$  and can be tuned through the resonance with the QW transition. In the case of the angular detuning a polariton dispersion as shown in Fig. (2.2) is measured.

### 2.3.2 Microcavity detuning with a cavity length gradient

The energy of the photonic mode in the microcavity is tunable as a function of the spot position on the sample by including a thickness gradient during growth of the active layer. With the method of MBE growth such a wedged active layer is obtained with a special geometric construction of the vacuum chamber. The most important point is the alignment of the evaporation cells with respect to the sample position.

Fig. (2.5) depicts the geometric position of the zinc and selenium evaporation cell as well as the sample position in our MBE system. The cells are aligned radially symmetric right opposite to the sample. Due to the fact that the sample is centered in the chamber, the molecular beams of each material are tilted by the same angle  $\alpha$  with respect to the substrate normal  $y$ .

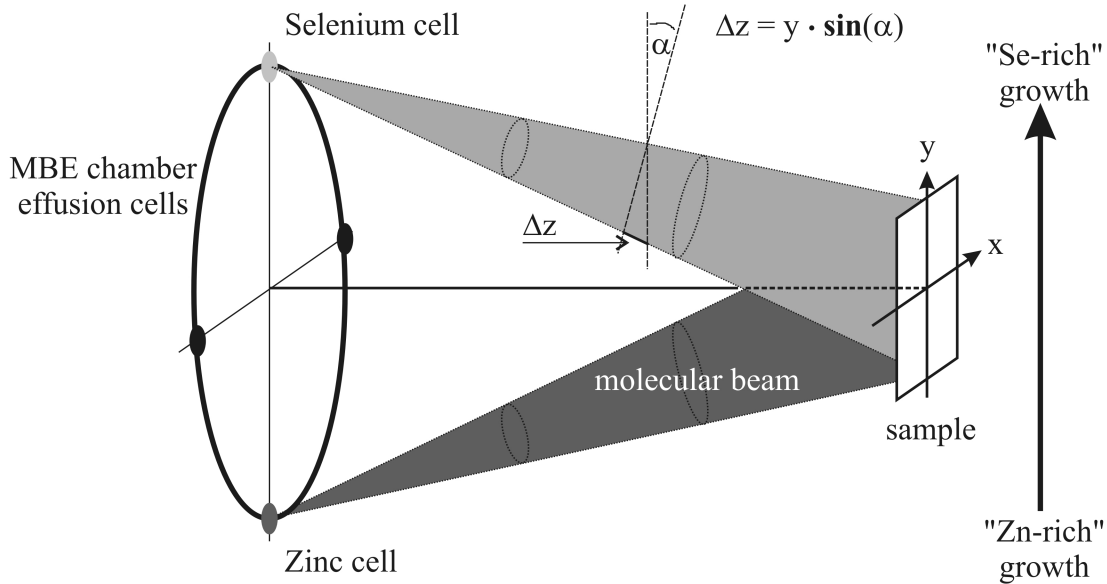


Figure 2.5: Alignment of the evaporation cells in our MBE chamber to implement growth gradient in the active layer. Due to the angular tilt  $\alpha$  of the zinc and selenium cell openings with respect to the substrate normal  $y$ , the molecular beam path length of both materials varies by  $\Delta z = y \cdot \sin(\alpha)$ . Therefore a molecular flux gradient along the  $y$ -axis of the sample is obtained.

This geometry results in a variation of the molecular beam path length  $\Delta z = y * \sin(\alpha)$ . The zinc and selenium cell are parallel to the  $y$ -axis of the sample. Therefore a maximum concentration gradient of zinc and selenium atoms on the sample surface is obtained and yields a growth gradient in the active layer in direction of the  $y$ -axis [Ar2003, Ba2003].

### 2.3.3 Temperature detuning in microcavity structures

The third possibility to modify the resonance conditions in microcavities is the temperature detuning as illustrated schematically in Fig. (2.6). The QW transition energy (dotted line) is shifted to lower energy with increasing temperature, due to the temperature dependence of the bandgap of barrier and QW material, respectively. The spot position on the sample and therefore the cavity mode energy (dashed line) is constant.

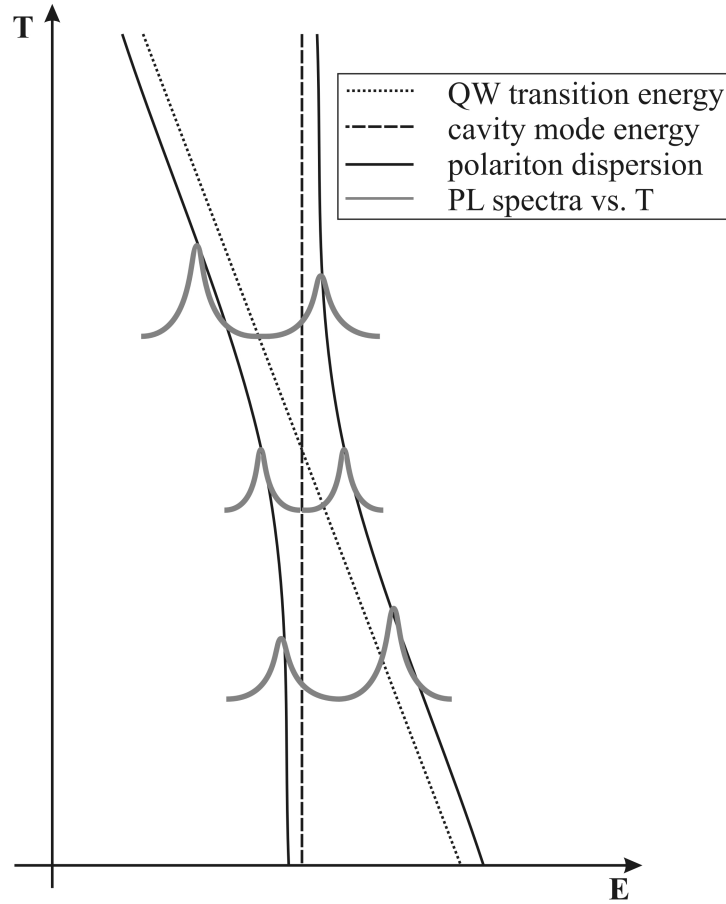


Figure 2.6: Principle of temperature detuning of a microcavity. The cavity mode energy (dashed line) is constant, while the QW transition energy (dotted line) shifts to lower energy with increasing temperature. From the PL spectra at certain temperatures, indicated by the grey curves, the temperature dependent polariton dispersion (black curves) are obtained.

The upper and lower polariton dispersion curves, Fig. (2.6), black curves, are obtained by measuring reflectivity or luminescence of the microcavity structure in a small temperature range near the resonance between photonic and excitonic mode. The grey curves, indicated in Fig. (2.6), schematically depict various PL spectra. The temperature dependence of the cavity mode is neglected and the QW transition energy shift is linear approximated. These assumptions are sufficiently fulfilled in ZnSe/(Zn,Cd)Se QWs in a temperature range between 250 K and 350 K.



# 3 Distributed Bragg-mirrors for II-VI microcavities

An important issue for the design of microcavity structures is the optimization of high reflectivity Bragg-mirrors for the photon confinement. In typical III-V structures based on GaAs, MBE grown AlAs/GaAs DBRs [Ba1995] are particularly suited on account of lattice matched growth on GaAs as well as a large refractive index difference of both materials in the near infrared spectral range.

For ZnSe based microcavity structures operating in the green spectral range, several II-VI materials and their alloys such as (Zn,Mg)(S,Se)/Zn(S,Se) [Uu1995] or ZnSe/MgS [Ta2000] are used as semiconductor DBRs. Despite the high structural quality of these mirrors, the refractive index difference is very small and leads to large stack numbers for the achievement of high reflectivity. Alternatively a large family of polycrystalline dielectric DBRs such as SiO<sub>2</sub>/TiO<sub>2</sub> ( $\Delta n \approx 1.0$ ) [Ke1995] have been recently used.

In this work dielectric DBRs of ZnS/YF<sub>3</sub> ( $\Delta n \approx 1.0$ ) and ZnSe/YF<sub>3</sub> ( $\Delta n \approx 1.3$ ) are optimized for the blue and green spectral range. Additionally to the large refractive index difference of these materials, the II-VI compounds ZnS and ZnSe are closely related to the cavity material with respect to the structural properties (i.e. thermal extension etc.). Furthermore YF<sub>3</sub> is a chemically stable anorganic compound with a small optical dispersion and a negligible absorption in the visible spectral range.

### 3.1 Optical properties of ZnS/YF<sub>3</sub> dielectric Bragg-mirrors

Several ZnS/YF<sub>3</sub> DBRs with four up to ten stack periods are grown on (001)-GaAs substrate by thermal evaporation. The reflectivity spectra are measured with a standard reflection measurement setup.

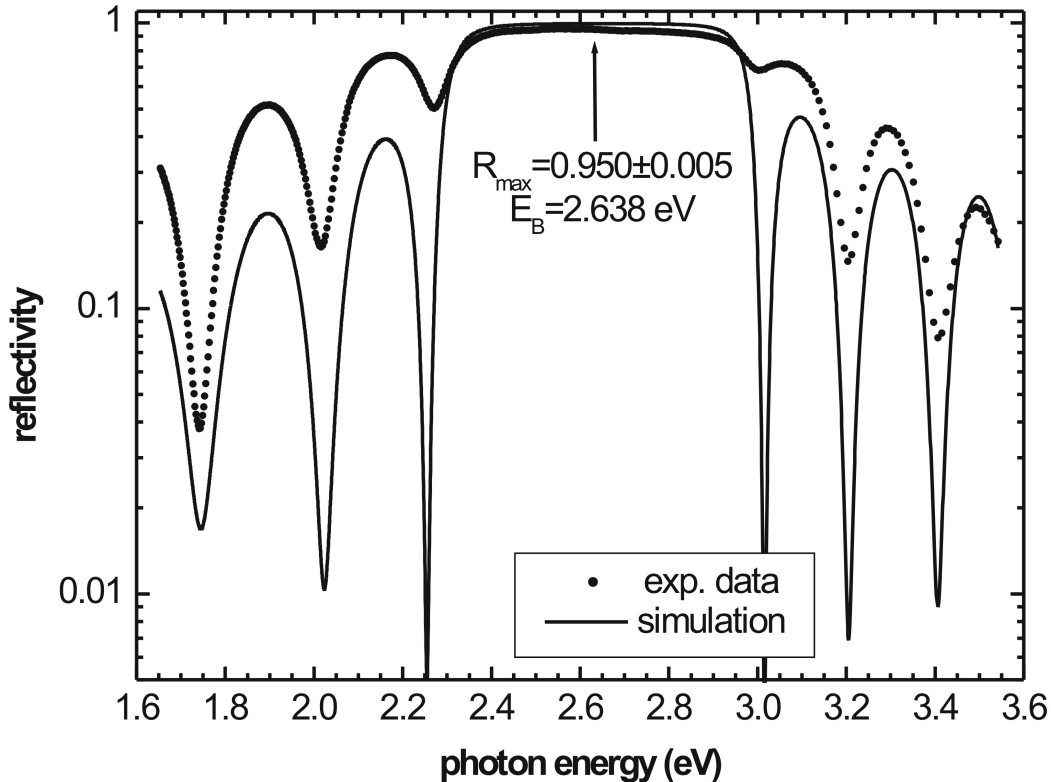


Figure 3.1: Reflectivity of the eight-fold stack of ZnS/YF<sub>3</sub> Bragg-mirror DBR-048 (dots) as a function of the photon energy. The theoretical reflectivity of the mirror (full curve) is calculated with the Transfer-Matrix model. The Bragg-wavelength  $\lambda_B$  and the refractive indices of both materials are used as simulation parameters. The experimental maximum reflectivity is about  $R_{max.} = 0.95$  at  $E_B = 2.638$  eV (i.e.  $\lambda_B = 470$  nm).

Fig. (3.1) shows the reflectivity spectrum (dots) of an eight-fold stack of ZnS/YF<sub>3</sub> DBRs on GaAs (sample DBR-048). The stop-band of the Bragg-mirror is clearly resolved between 2.4 eV and 2.9 eV, yielding a maximal reflectivity about  $0.950 \pm 0.005$  in its center. The experimental data are fitted with the Transfer-Matrix model (full curves) to obtain

the refractive index difference  $\Delta n$  between ZnS and YF<sub>3</sub> and the stop-band centrum (i.e. the Bragg-wavelength  $\lambda_B$ ).

In the stop-band region the simulated curve is in good agreement with the experimental data and the energetic position of the interference fringes are also matched. However, in the low energy region between 1.6 eV and 2.2 eV, the measured spectrum has a significantly larger reflectivity than it is calculated in the simulation. The reflectivity depends especially in that region mainly on the refractive index and absorption coefficient of the GaAs substrate, but does not influence the important mirror parameters.

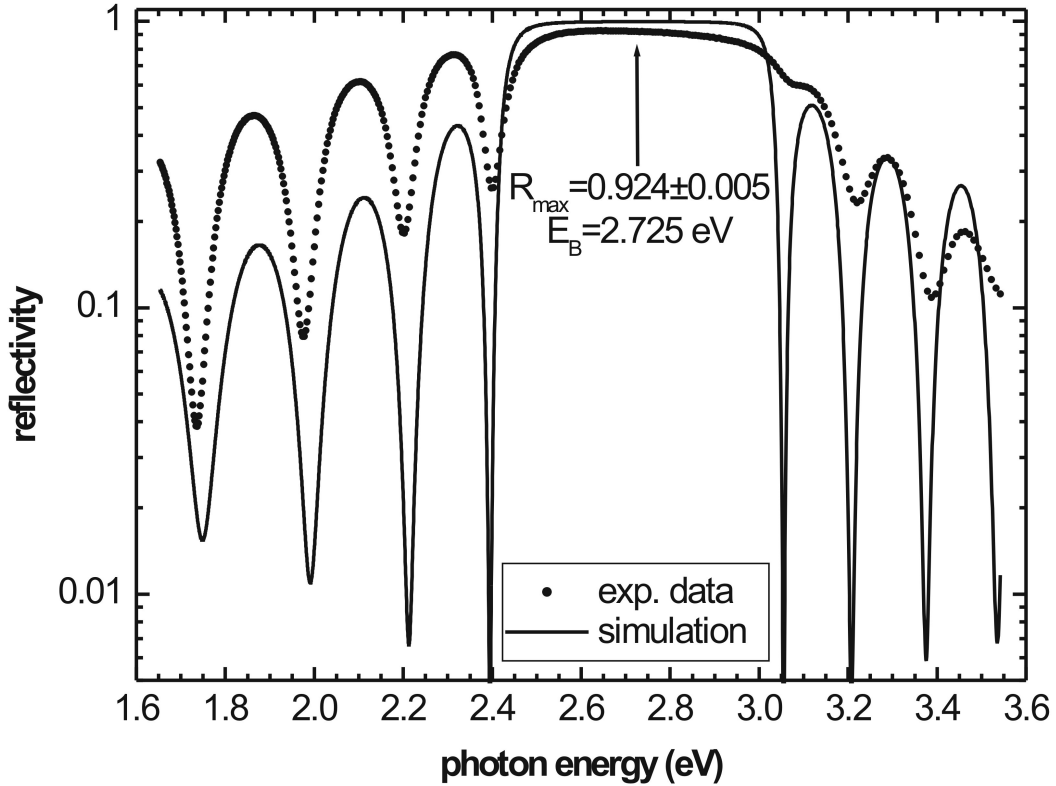


Figure 3.2: Reflectivity of the ten-fold stack Bragg-mirror DBR-045 (dots) and the calculated data (full curve) as a function of the photon energy. The experimental maximum reflectivity is about  $R_{\max.} = 0.924$  at  $E_B = 2.725 \text{ eV}$  (i.e.  $\lambda_B = 470 \text{ nm}$ ).

In Fig. (3.2) the reflectivity spectrum of the sample DBR-045 (dots), a ten-fold stack of DBRs, is illustrated. The full curve denotes the calculated data obtained by the

Transfer-Matrix simulation. The stop-band is shifted to higher energies compared to that of the spectrum of the eight-fold stack, but has a similar size and shape. The experimental maximum reflectivity of about  $0.924 \pm 0.005$  is significantly smaller compared to the reflectivity of the eight-fold stack. This fact reveals that the reflectivity of ZnS/YF<sub>3</sub> DBRs is limited by additional structural parameters and not only by the number of periods. A more detailed discussion of this observation is given in Sec. (3.1.1).

The fitting parameters, which are used for the Transfer-Matrix simulation, are summarized in Tab. (3.1). The six-, eight-, and ten-fold stack are deposited by thermal evaporation. In case of these mirrors the refractive index difference  $\Delta n(\lambda_B)$  between ZnS and YF<sub>3</sub> is significantly smaller than the theoretical value.

The five-fold stack of ZnS/YF<sub>3</sub> DBRs (see also Fig. (3.3)) is grown by electron beam assisted evaporation. The maximum reflectivity as well as the refractive index difference is in excellent agreement with the theoretical data. The lower refractive index difference in

periods	$R_{max.}$	$\lambda_B$ (nm)	$\Delta n(\lambda_B)$	$R_{theo.}$	$\Delta n_{theo.}$
6	0.930	487	0.58	0.990	0.97
8	0.950	470	0.64	0.996	1.03
10	0.924	455	0.55	0.998	1.05
5	0.979	508	0.96	0.987	1.01

Table 3.1: Experimental (left side) and theoretical (right side) parameters of different ZnS/YF<sub>3</sub> DBRs. The six-, eight- and ten-fold stacks are deposited by thermal evaporation of ZnS and YF<sub>3</sub>, the five-fold stack is grown by electron beam assisted evaporation of the materials.

the six- eight- and ten-fold stack of Bragg-mirrors indicates an interdiffusion between ZnS and YF<sub>3</sub> during the thermal evaporation process. This effect is amplified with increasing stack periods and growth time. Furthermore a dissociation of the binary ZnS and a change in the composition during evaporation has to be considered, due to the high vapor pressure of sulphur.

The measured and the simulated reflectivity spectrum of the five-fold stack are illustrated in Fig. (3.3). The stop-band is nearly rectangular and significantly larger compared to

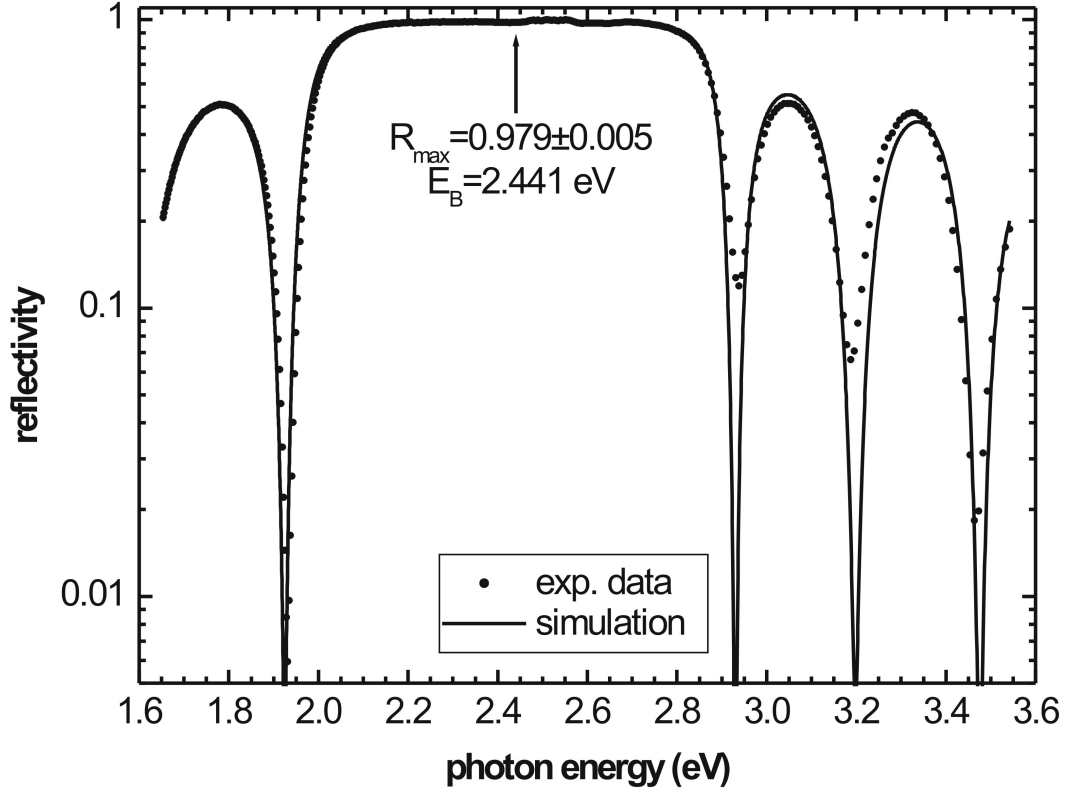


Figure 3.3: Reflectivity of a five-fold stack of ZnS/YF<sub>3</sub> Bragg-mirrors (dots) grown by electron beam assisted evaporation. The experimental maximum reflectivity is about  $R_{max.} = 0.979$  at  $E_B = 2.441$  eV (i.e.  $\lambda_B = 508$  nm). The stop-band size is larger than that of the eight- and ten-fold stack, revealing better interface quality and reduced interdiffusion between ZnS and YF<sub>3</sub>.

that of the eight- and ten-fold stack. Furthermore the five-fold stack has an increased maximum reflectivity of about  $R_{max.} = 0.979 \pm 0.005$ . This result reveals that no significant interdiffusion at the interfaces between ZnS and YF<sub>3</sub> or composition changes in the materials are observed, if the Bragg-mirrors are grown by electron beam assisted evaporation.

### 3.1.1 Structural properties of ZnS/YF<sub>3</sub> DBRs

The interface roughness and the surface structure of the DBRs is an important factor, which determines the Bragg-mirror quality. If the surface roughness increases with the

number of periods, the reflectivity is limited, due to scattering loss at the interfaces.

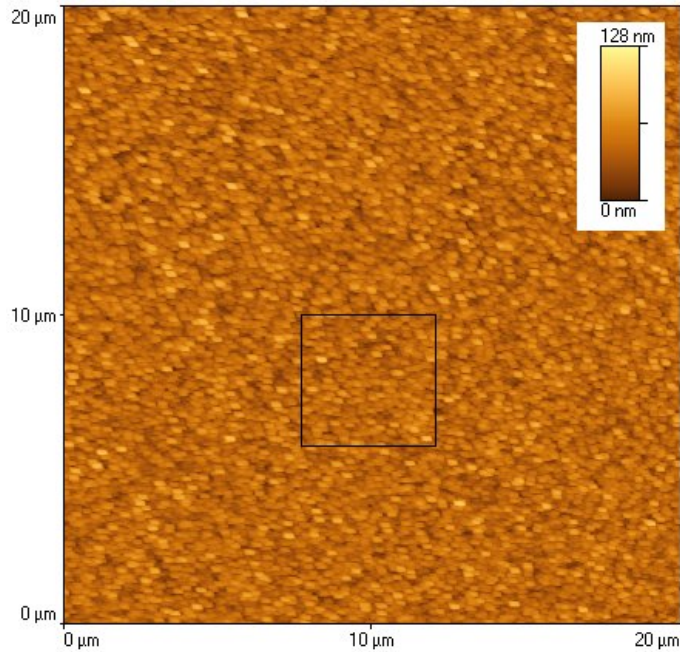


Figure 3.4: AFM picture of a  $20\ \mu\text{m} \times 20\ \mu\text{m}$  scan of the ZnS surface of sample DBR-034, a six-fold stack of ZnS/YF<sub>3</sub> DBRs. The figure illustrates a clear polycrystalline surface. The RMS roughness in the black frame is about  $16 \pm 1$  nm.

Fig. (3.4) shows the surface morphology of the top ZnS layer of a six-fold stack of ZnS/YF<sub>3</sub> Bragg-mirrors. The surface is measured in a  $20\ \mu\text{m} \times 20\ \mu\text{m}$  AFM scan directly after mirror deposition, to avoid a significant surface modification, due to oxidation in atmospheric environment. The picture illustrates a clear polycrystalline surface with cubic ZnS microcrystals of a size in the order of 400 nm. The RMS surface roughness, calculated in the small rectangular area, is about  $16 \pm 1$  nm.

Fig. (3.5) shows the RMS surface roughness (dots) of different DBRs with four up to ten pairs of ZnS/YF<sub>3</sub> mirrors. The surface roughness increases with the number of periods and yields that the mirror interface quality is reduced in larger stacks. The full curve describes a linear dependence between surface roughness and number of periods.

Hence the mode leakage (i.e. increased scattering loss of photons) limits the maximum

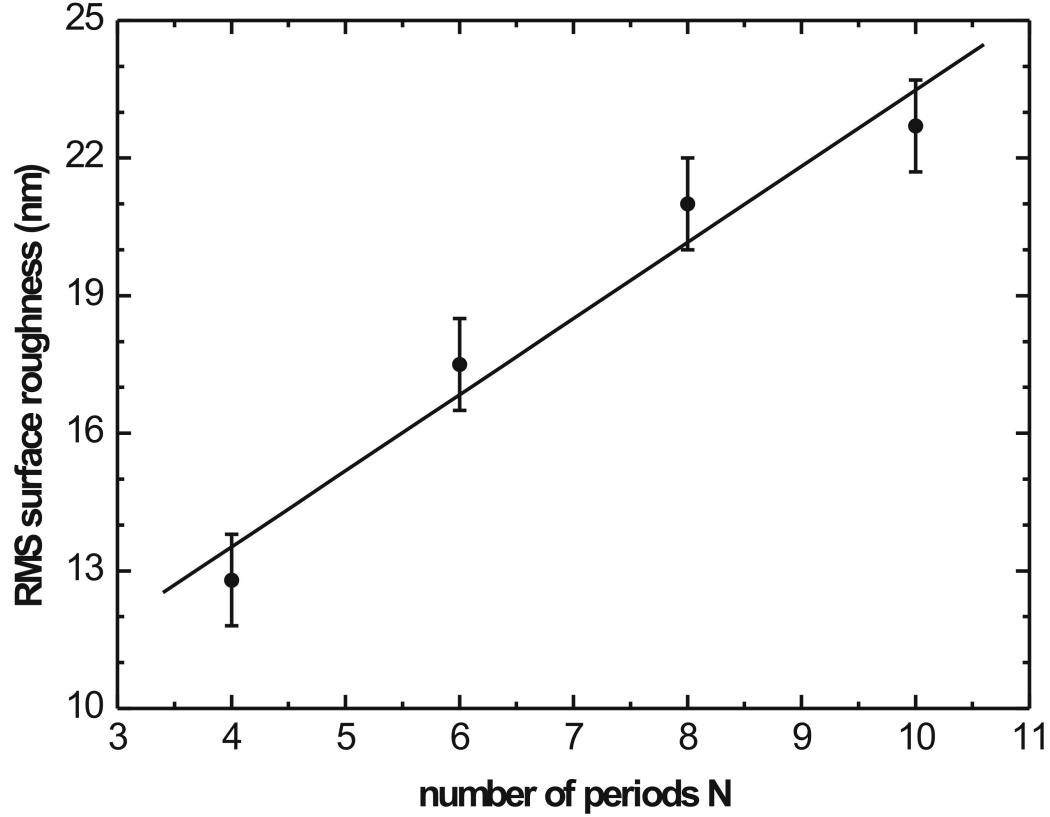


Figure 3.5: RMS surface roughness of several ZnS/YF<sub>3</sub> DBRs (dots) as a function of the number of stacks. The line graph depicts a linear dependence between surface roughness and number of periods.

reflectivity of ZnS/YF<sub>3</sub> Bragg-mirrors with a large number of periods. This fact is in good agreement with the reflectivity measurements in Sec. (3.1) and explains that the ten-fold stack DBR has a lower reflectivity than the eight-fold stack. Fig. (3.6) shows the experimental maximum reflectivity  $R_{exp.}(N)$  (dots) as well as the calculated maximum of reflectivity  $R_{theo.}(N)$  (grey curve) as a function of the number of Bragg-mirror periods  $N$  and assuming perfect planar interfaces.

The deviation between experimental and calculated data increases with the number of periods, due to the scattering loss at imperfect interfaces. The black curve depicts the calculated maximum reflectivity considering a scattering factor

$$\sigma = \frac{R_{exp.}}{R_{theor.}} = 1 - 0.007 * N, \quad (3.1)$$

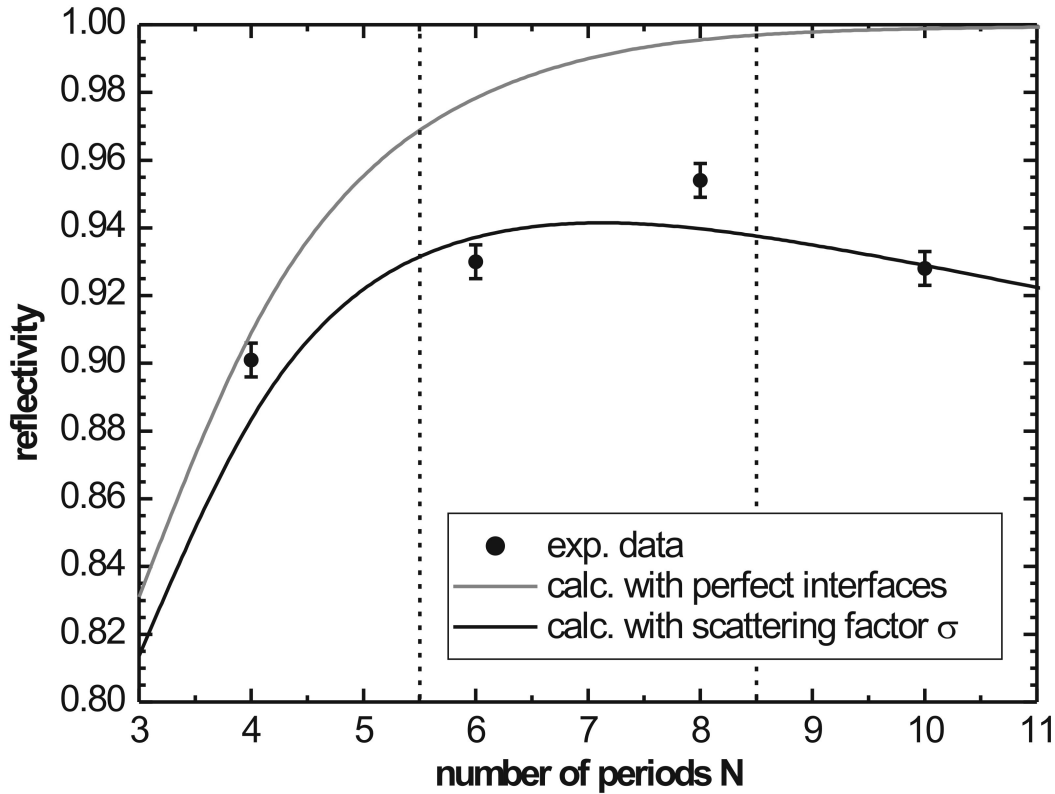


Figure 3.6: Maximum reflectivity of several ZnS/YF<sub>3</sub> DBRs as a function of the number of periods (dots). The full curves depict the calculated maximum reflectivity for planar interfaces without any scattering loss (grey curve) and for imperfect interfaces (black curve) including a scattering factor  $\sigma$ , which is proportional to the surface roughness, respectively.

which is proportional to the number of periods. This assumption is in good agreement with the experimental data and confirms the model that the maximum reflectivity of ZnS/YF<sub>3</sub> DBRs, grown by thermal evaporation of the binary materials, is limited by the interface roughness. The black dotted lines in Fig. (3.6) show that six-, seven- and eight-fold stacks of ZnS/YF<sub>3</sub> Bragg-mirrors have an adequately reflectivity for microcavity applications.

## 3.2 ZnSe and YF<sub>3</sub> Bragg-Mirrors

Due to the fact that the reflectivity of ZnS/YF<sub>3</sub> DBRs is limited by structural properties such as interface roughness and sulphur interdiffusion, alternatively Bragg-mirrors of the materials ZnSe and YF<sub>3</sub> are characterized in this section.

As shown in Fig. (2.4), the most important advantage of ZnSe/YF<sub>3</sub> DBRs is the larger refractive index difference compared to that of ZnS/YF<sub>3</sub> mirrors. Hence it follows that a larger reflectivity can be achieved with a smaller number of periods in the ZnSe/YF<sub>3</sub> mirrors. Furthermore the material sulphur is exchanged by selenium. This material has a vapor pressure, which is some orders of magnitude smaller compared to that of sulphur. Therefore the composition of the ZnSe vapor pressure is stabilized. Additionally to this interdiffusion between ZnSe and YF<sub>3</sub> during the mirror deposition is reduced.

The disadvantage of ZnSe/YF<sub>3</sub> mirrors is the increased absorption of light in ZnSe above its bandgap energy of about 2.72 eV. This can limit the maximum reflectivity in the blue spectral region.

### 3.2.1 Optical properties of ZnSe/YF<sub>3</sub> DBRs

For further improvement of the microcavity structures, several ZnSe/YF<sub>3</sub> DBRs are grown by thermal evaporation and also with processing parameters, which are comparable to that of the ZnS/YF<sub>3</sub> Bragg-mirrors. Fig. (3.7) depicts the measured and the theoretical reflectivity spectrum of the ten-fold stack of ZnSe/YF<sub>3</sub> Bragg-mirrors (DBR-219) grown on GaAs substrate. The experimental data show clear interference fringes and a well determined and rectangular shaped stop-band between 2.15 eV and 3.15 eV, yielding a good interface quality in the mirrors.

A clear reduction of the reflectivity which stems from the ZnSe bandgap absorption is measured above 2.65 eV. The maximum reflectivity of the ZnSe/YF<sub>3</sub> ten-fold stack is about  $R_{max.} = 0.999 \pm 0.005$  at  $E_B = 2.610$  eV (i.e.  $\lambda_B = 475$  nm). The reflectivity is significantly larger compared to that of the ZnS/YF<sub>3</sub> ten-fold stack mirror in Fig. (3.2).

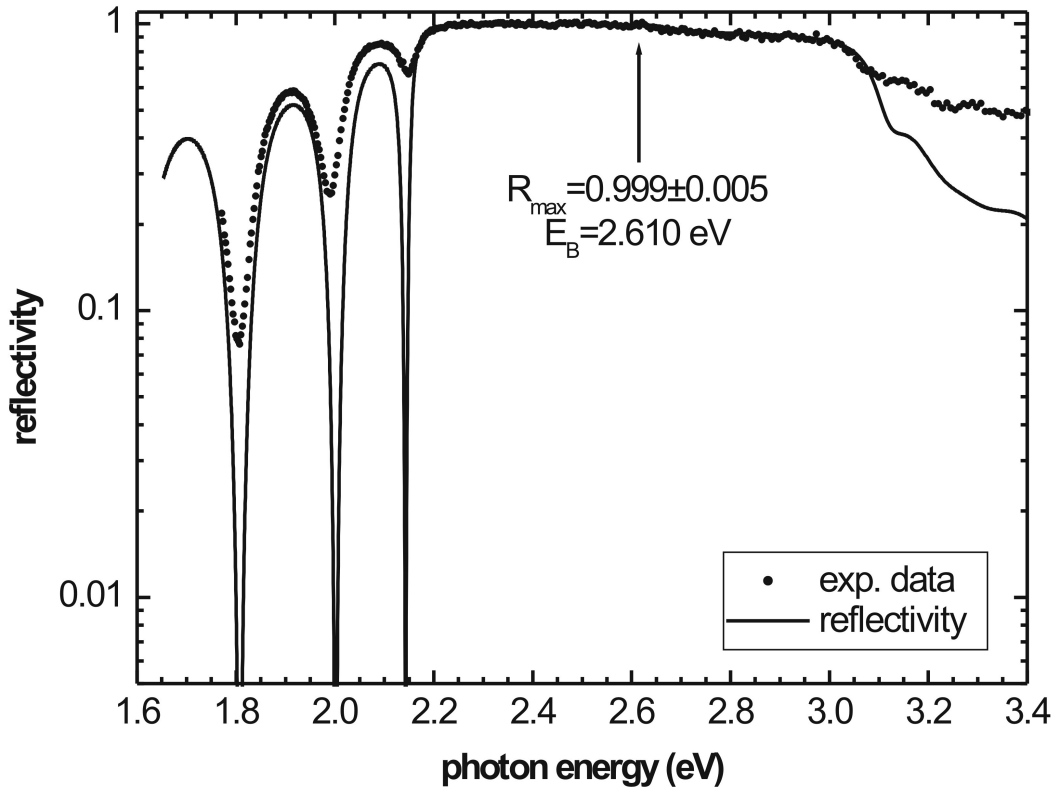


Figure 3.7: Reflectivity spectrum of the ten-fold stack of ZnSe/YF<sub>3</sub> Bragg-mirrors DBR-219 (dots) as well as the approved Transfer-Matrix calculation (full curve). The refractive indices of both materials and the Bragg-wavelength are used as simulation parameters. The maximum reflectivity is about  $R_{max.} = 0.999$  at  $E_B = 2.610$  eV (i.e.  $\lambda_B = 475$  nm). At energies larger than 2.65 eV the reflectivity is significantly reduced due to the ZnSe bandgap absorption.

The calculated reflectivity curve in Fig. (3.7) is in good agreement with the experimental data between 1.6 eV and 3.2 eV.

Despite that, the experimental measured reflectivity is above 3.2 eV larger than the calculated values. For the Transfer-Matrix simulation of the measured spectrum in Fig. (3.7) the refractive index dispersion of monocrystalline ZnSe has been used, but in polycrystalline ZnSe the absorption might be reduced.

The reflectivity spectrum of the five-fold stack of ZnSe/YF<sub>3</sub> DBRs (sample DBR-252) is illustrated in Fig. (3.8). The experimental measured reflectivity about  $R_{max.} = 0.993$  at

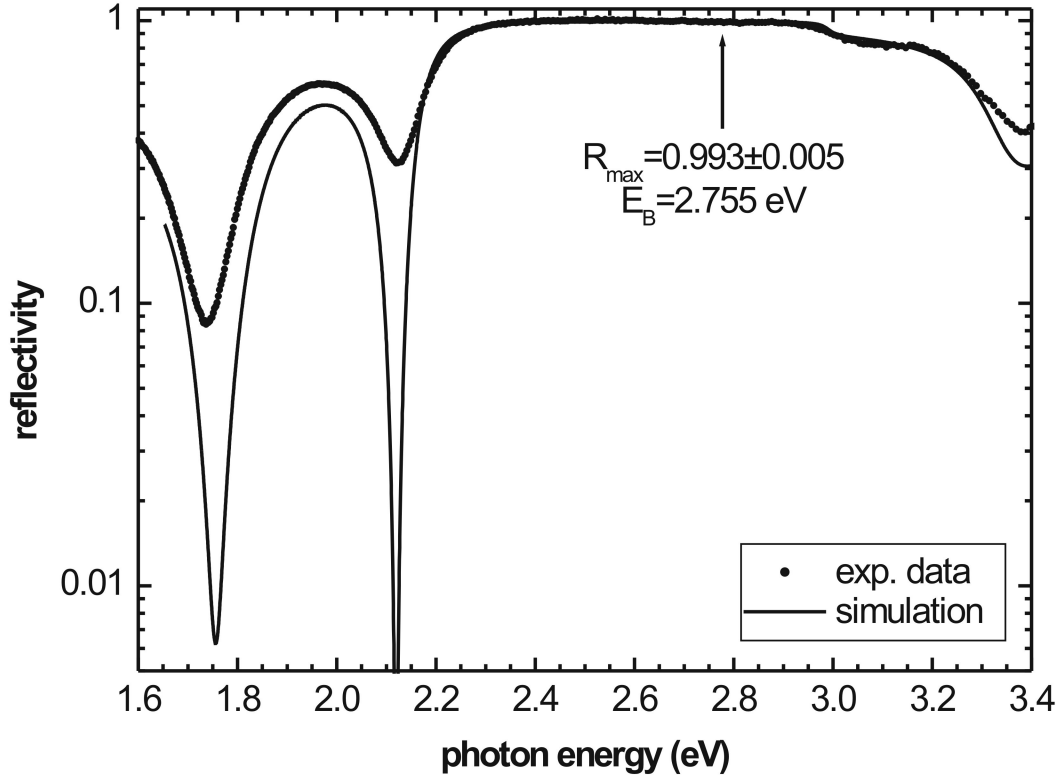


Figure 3.8: Reflectivity spectrum of the five-fold stack of ZnSe/YF<sub>3</sub> Bragg-mirrors DBR-252 (dots) and the calculated data (full curve). The experimental maximum of reflectivity is about  $R_{max.} = 0.993$  at  $E_B = 2.755$  eV (i.e.  $\lambda_B = 450$  nm). The ZnSe bandgap absorption has a significant influence on the reflectivity at energies larger than 2.85 eV. This value is shifted about ten percent to larger energies compared to that of the ten-fold stack Bragg-mirror.

$E_B = 2.755$  eV (i.e.  $\lambda_B = 450$  nm) is in good agreement with the simulation parameters and just slightly smaller compared to the reflectivity of the ten-fold stack DBR-219.

The fact that size and shape of the stop-band in both spectra is quite similar indicates that interdiffusion of the materials at the mirror interfaces is not increasing with the number of periods as it has been observed in the ZnS/YF<sub>3</sub> DBRs. The influence of ZnSe absorption on the reflectivity is measured in both mirrors, but in the five-fold stack the bandgap energy is shifted about ten percent to higher energies compared to the data of DBR-219. Since the bandgap energy is related to the crystal structure, the energy difference indicates

a fluctuation of the structural quality of the polycrystalline ZnSe layers.

periods	$R_{max.}$	$\lambda_B$ (nm)	$\Delta n(\lambda_B)$	$R_{theo.}$	$\Delta n_{theo.}$	$E_g(\text{ZnSe})$ (eV)
5	0.993	450	1.43	0.992	1.30	2.99
6	0.990	488	1.13	0.996	1.30	2.60
8	0.996	500	1.06	0.998	1.23	2.60
10	0.999	475	1.28	0.995	1.29	2.67

Table 3.2: Experimental (left side) and theoretical (right side) parameters of different ZnS/YF<sub>3</sub> DBRs. The mirrors are deposited by thermal evaporation of ZnSe and YF<sub>3</sub>. The bandgap energy of the polycrystalline ZnSe layers is considered in the Transfer-Matrix simulation and responsible for the reduction of the reflectivity in the stop-band.

The parameters used for the Transfer-Matrix simulation of the reflectivity of different ZnSe/YF<sub>3</sub> Bragg-mirrors are summarized in Tab. (3.2). The experimental maximum reflectivity is in every case larger than 0.99 and also in good agreement with the theoretical data. For five up to ten Bragg-mirror periods, no reduction of the reflectivity is observed, unlike it has been shown for ZnS/YF<sub>3</sub> DBRs in the previous section.

The refractive index difference between ZnSe and YF<sub>3</sub> differs slightly from the theoretical values, but has no clear decreasing trend. Therefore material interdiffusion between ZnSe and YF<sub>3</sub> does not depend on the number of mirror periods and is negligible. The bandgap energy, which has been extracted from the ZnSe refractive index dispersion, varies between 2.6 eV and 3.0 eV. This reveals that the structural quality of polycrystalline ZnSe is very sensitive to fluctuations of the mirror growth parameters.

Despite the increased absorption in ZnSe/YF<sub>3</sub> Bragg-mirrors near the ZnSe bandgap, the optical properties of thermal evaporated ZnSe/YF<sub>3</sub> DBRs are significantly improved compared to that of ZnS/YF<sub>3</sub> Bragg-mirrors.

### 3.2.2 Structural properties of ZnSe/YF<sub>3</sub> Bragg-mirrors

Hence the reflectivity of ZnSe/YF<sub>3</sub> DBRs is not decreasing in larger mirror stacks, the interface roughness, which is related to the surface roughness, is expected to be significantly

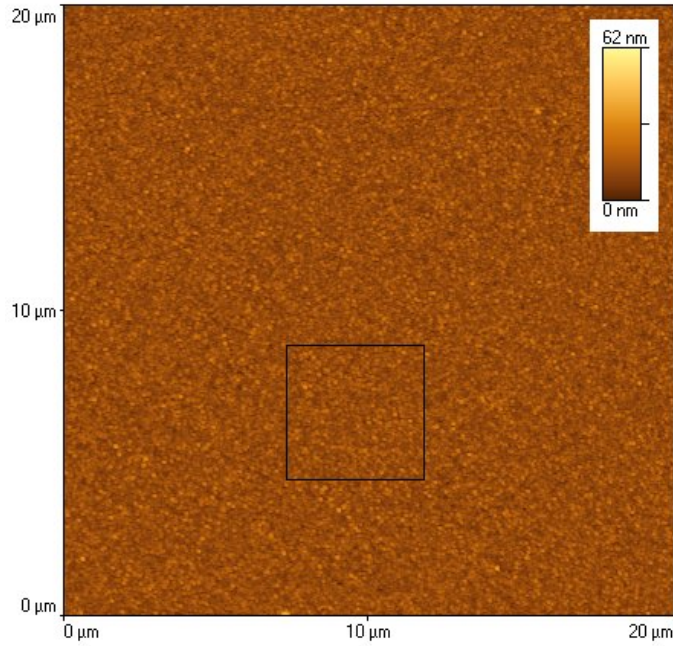


Figure 3.9: AFM picture of a  $20\ \mu\text{m} \times 20\ \mu\text{m}$  scan of the ZnSe surface of the ten-fold stack of ZnSe/YF<sub>3</sub> DBRs (sample DBR-215). The RMS surface in the black square region is about  $5 \pm 1\ \text{nm}$ , which is significantly smaller compared to the typical surface roughness of ZnS/YF<sub>3</sub> DBRs (about 10-20 nm).

smaller than the roughness of ZnS/YF<sub>3</sub> Bragg-mirrors.

Fig. (3.9) illustrates the AFM picture of a  $20\ \mu\text{m} \times 20\ \mu\text{m}$  scan on the ZnSe surface of the ten-fold stack of Bragg-mirrors DBR-215. The image is taken directly after the mirror deposition to avoid a significant surface modification due to oxidation in atmospheric environment. The surface is relatively plane and the RMS roughness is about  $5 \pm 1\ \text{nm}$ . This value is significantly smaller compared to the RMS roughness of ZnS/YF<sub>3</sub> Bragg-mirrors.

The RMS roughness and the maximum reflectivity of the ZnSe/YF<sub>3</sub> DBRs are summarized in Fig. (3.10). The black dots represent the experimental maximum of reflectivity of the different ZnSe/YF<sub>3</sub> DBRs. The full curve describes the reflectivity at  $\lambda_B = 480\ \text{nm}$  as a function of the number of periods and is calculated with the Transfer-Matrix model assuming perfect planer interfaces.

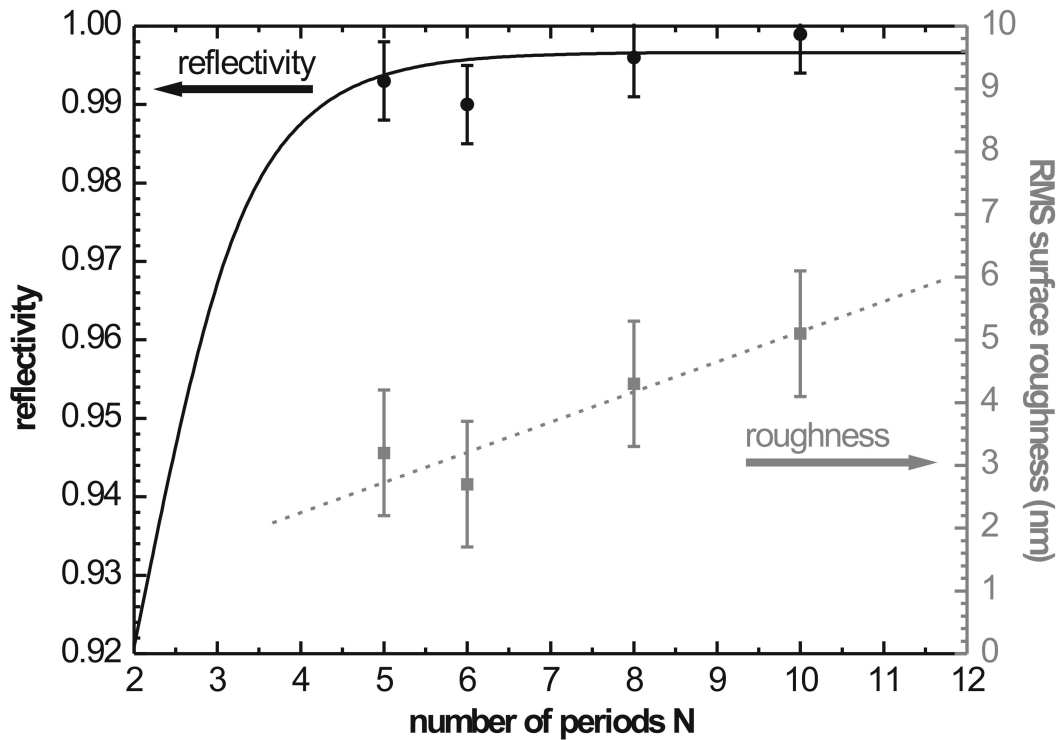


Figure 3.10: Reflectivity (left scale) and surface roughness (right scale) of different ZnSe/YF<sub>3</sub> DBRs as a function of the number of periods. The black curve describes the reflectivity of the mirrors calculated with a Bragg-wavelength of  $\lambda_B = 480$  nm and assuming perfect planar interfaces. The experimental results (black dots) are in excellent agreement with the theoretical data. The grey squares depict the RMS surface roughness of the DBRs measured by AFM. The dashed grey line denotes a linear increase of the RMS roughness with the number of stacks.

Experimental and theoretical data are in excellent agreement yielding that the interfaces between the materials are well determined. The reflectivity, calculated for a Bragg-wavelength of  $\lambda_B = 480$  nm and as a function of the number of periods, is significantly limited to  $R_{max.} = 0.9966$ , due to the ZnSe bandgap absorption.

The grey squares and the grey dashed line in Fig. (3.10) represent the RMS surface roughness of the ZnSe/YF<sub>3</sub> DBRs as a function of the number of periods. The surface roughness is about three times smaller compared to that of ZnS/YF<sub>3</sub> Bragg-mirrors. Despite that, it also shows a linear increase for larger stack periods, but no decrease of

the reflectivity is observed within the accuracy of the measurement system.

In conclusion, both Bragg-mirror systems are particularly suited for deposition on ZnSe based microcavity structures. In the green spectral region the ZnSe/YF<sub>3</sub> DBRs seem to be superior, due to their better structural quality and larger refractive index difference. In the blue spectral range the ZnS/YF<sub>3</sub> DBRs have the advantage of reduced absorption in the DBRs.



## 4 ZnSe and (Zn,Cd)Se quantum structures for II-VI microcavities

This chapter is focused on the development and optimization of the active layer in the microcavity structures. The II-VI semiconductor materials, especially ZnSe and CdSe, have been investigated intensively to develop optoelectronic devices in the blue and green spectral range [Ea1995]. Due to the fact that (001)-GaAs substrates are nearly lattice matched on ZnSe, dramatic advance of the crystallographic properties of ZnSe layers has been achieved by MBE growth.

Furthermore the exciton binding energy (about 30 meV [Gu1982]) and the oscillator strength of bulk ZnSe is significantly larger compared to that of other II-VI based semiconductors such as ZnTe or CdTe. Therefore the ZnSe and CdSe based materials are particularly suited for room-temperature applications of optoelectronic devices. First success to develop a room temperature VCSEL structure with (Zn,Cd)Se QWs enclosed in Zn(S,Se) barriers has been achieved in 1995 by Jeon et. al. [Je1995].

One of the most important points in this work is the adjustment of the (Zn,Cd)Se QW emission (i.e. the excitonic mode) to the cavity mode energy (i.e. photonic mode). The cavity mode depends on the resonator length and is manifested, after the active layer has been enclosed in the DBRs of ZnS/YF<sub>3</sub> or ZnSe/YF<sub>3</sub>, respectively.

Due to the fact that the strong coupling between excitonic and photonic mode is established only when the strong coupling conditions in Sec. (2.1.1) are fulfilled, another important step is the optimization of the QW luminescence with respect to the FWHM

of the transition energy. Last but not least the strain status of the (Zn,Cd)Se QWs has to be considered.

## 4.1 In-situ growth characterization of ZnSe/(Zn,Cd)Se quantum structures

The most common in-situ characterization of the crystallographic properties during MBE growth are RHEED-measurements. Due to the formation of two dimensional islands on a plane semiconductor surface during growth, the surface roughness changes periodically. The reflectivity is maximal, when the surface is fully covered with one monolayer of atoms and minimal for half coverage, respectively.

From the intensity oscillations of the specular spot (i.e. the reflected primary electron beam), the growth rate (i.e. the time, which is needed to grow one monolayer of atoms) is obtained and opens up the possibility to determine the thickness of the layer.

The optimized growth regime is obtained under slightly selenium rich conditions [Wo2000], hence then the metal flux will determine the growth rate. Furthermore the re-evaporation of selenium atoms from the surface is avoided, which results in an appreciable smooth surface.

Fig. (4.1) depicts the typical intensity oscillations of the specular spot after growth start of ZnSe on a atomically flat GaAs surface. The intensity oscillations of the specular spot are clearly visible and show a well defined periodicity. The damping stems from simultaneous growth of several monolayers at the same time. The average growth rate (GR), which is obtained from the oscillations in Fig. (4.1), is  $GR(\text{ZnSe}) = 0.29 \pm 0.01 \text{ ML}\cdot\text{s}^{-1}$ .

The calculation of the ZnSe growth rate from the growth oscillations is the most important aspect to determine the thickness of the ZnSe/(Zn,Cd)Se quantum structure and to fix the energetic position of the cavity mode. Analyzed in the concept of growth rate calculation from RHEED-oscillation measurements, the typical resonator length is about  $200 \pm 7 \text{ nm}$ . Therefore it is necessary to implement an additional thickness gradient in the structure to

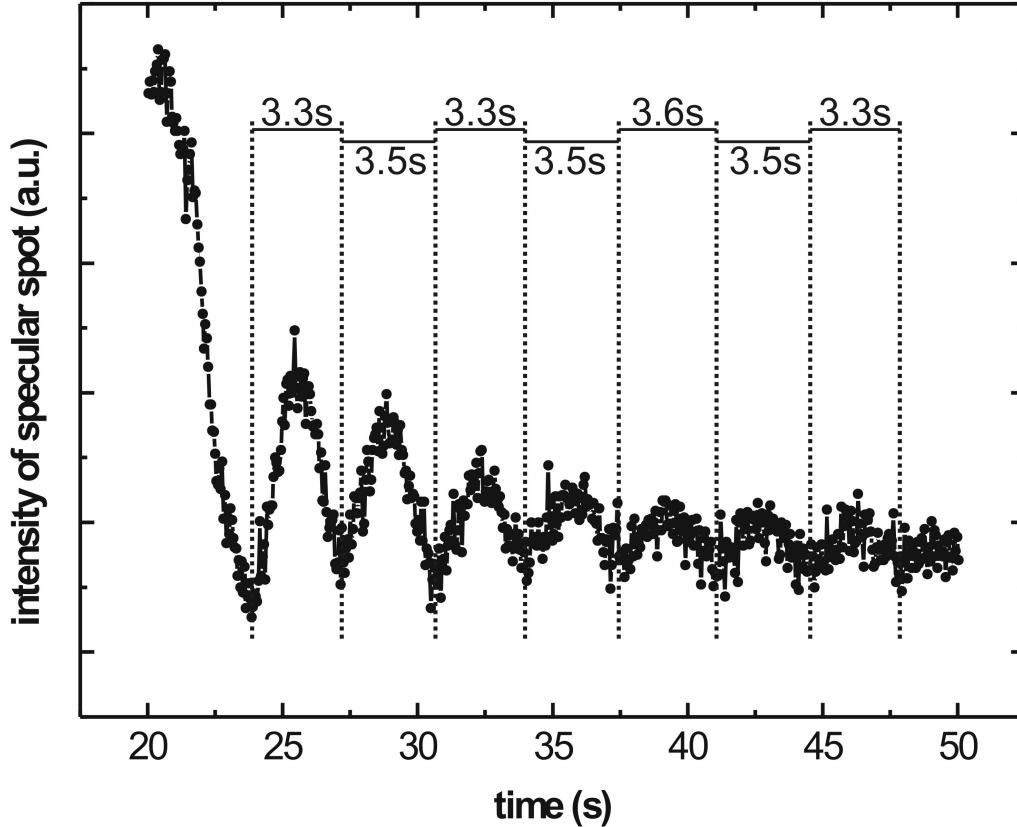


Figure 4.1: Intensity oscillations of the specular spot during deposition of ZnSe on a two dimensional plane GaAs surface. From the time difference between two minima or maxima of the intensity, respectively, the growth rate is determined. In this case the average growth rate is  $GR(\text{ZnSe}) = 0.29 \pm 0.01 \text{ ML}\cdot\text{s}^{-1}$ .

obtain a tunable cavity mode, which can be brought into resonance with the QW emission [We1992].

The transition energy of the ZnSe/(Zn,Cd)Se QWs is determined by the cadmium mole fraction as well as the thickness of the (Zn,Cd)Se layers. Therefore it is necessary to monitor the atomic flux of the zinc and the cadmium atoms, which are incorporated into the structure.

The RHEED intensity oscillations during the (Zn,Cd)Se QW growth are shown in Fig. (4.2). Due to the lattice mismatch of (Zn,Cd)Se on GaAs (about 2.5 % for a cadmium mole fraction of about 0.3), the oscillations are not as pronounced as in ZnSe and are also strongly

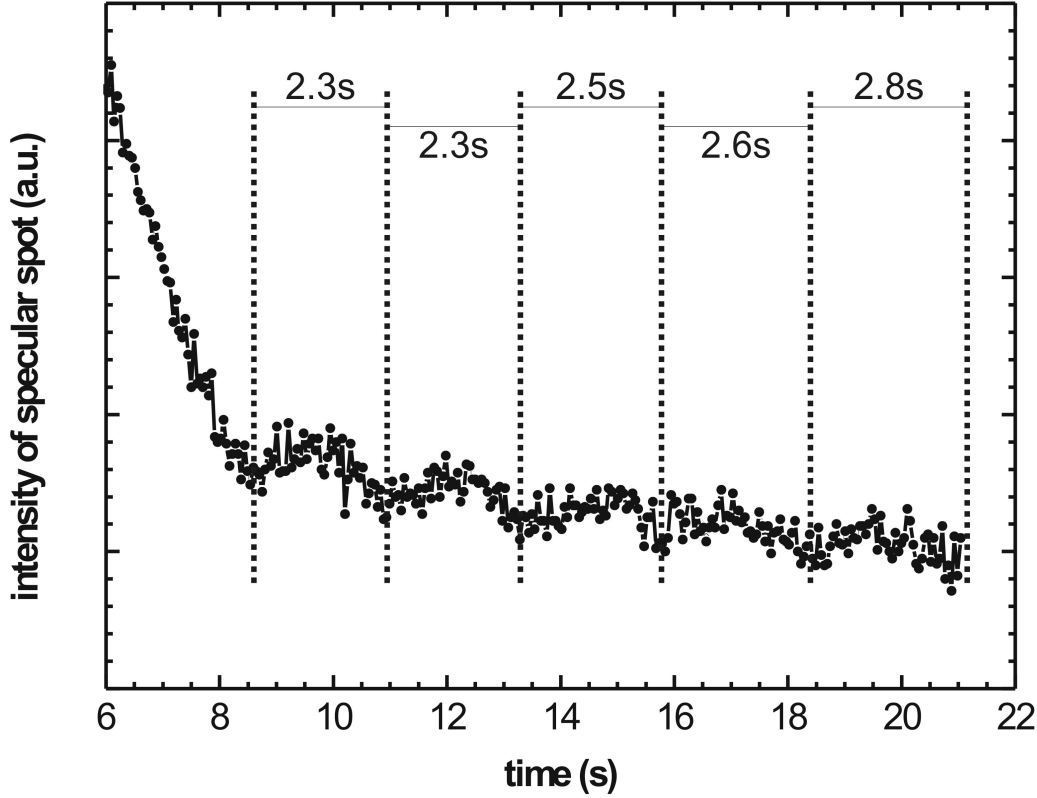


Figure 4.2: Intensity oscillations of the specular spot during deposition of a (Zn,Cd)Se QW. The oscillations are strongly damped and hardly resolved. The average growth rate is  $GR((\text{Zn,Cd})\text{Se}) = 0.37 \pm 0.05 \text{ ML}\cdot\text{s}^{-1}$ .

damped. The average (Zn,Cd)Se growth rate is  $GR(\text{ZnCdSe}) = 0.37 \pm 0.05 \text{ ML}\cdot\text{s}^{-1}$ . Therefore the thickness of the QW is obtained with an accuracy of  $\pm 0.5 \text{ nm}$ .

Hence the growth regime of ZnSe, CdSe and their alloys is connected to selenium rich conditions, the growth rate of the materials is limited by the amount of metal, which is incorporated into the growing surface. Therefore the Cd mole fraction in the QWs is obtained from the relative difference of the ZnSe and (Zn,Cd)Se growth rates

$$x(\text{Cd}) = \frac{GR(\text{ZnCdSe}) - GR(\text{ZnSe})}{GR(\text{ZnCdSe})}, \quad (4.1)$$

respectively. The dependence of the cadmium mole fraction from the Zn:Cd flux ratio

$\chi = \frac{BEP(Zn)}{BEP(Cd)}$  has been investigated in [Pa2000], yielding

$$x(Cd) = (1 + 1.15 * \chi)^{-1}. \quad (4.2)$$

Analyzed via the concept in Eq. (4.1) and Eq. (4.2), it is possible to calculate the growth time of the QWs, to achieve a well defined thickness and cadmium mole fraction, respectively.

## 4.2 Investigation of (Zn,Cd)Se multi quantum wells

For the optimal achievement of exciton-photon coupling in microcavities, it is necessary to include a maximum number of QWs into a resonator as short as possible. In this thesis the typical optical resonator length (ZnSe barriers plus QWs) is about  $n_C * L_C = 1 \lambda$ , where  $n_C$  and  $L_C$  are the refractive index and length of the cavity, respectively, and  $\lambda$  is the emission wavelength of the structure.

The active medium of the resonator is represented by the (Zn,Cd)Se QWs. These are placed near the antinodes of the standing wave in the microcavity, to achieve optimized interaction of photons and excitons.

Fig. (4.3) depicts a cross-section drawing of the two types of MQW structures, which are investigated in this section. The cavity length of about 192 nm (i.e.  $\lambda$ -resonator) is adapted to the QW emission in the green spectral range. The active layers are represented by (Zn,Cd)Se QWs enclosed in ZnSe barriers. The MQW structure on the left side in Fig. (4.3) contains two QWs in the center and also two QWs near the resonator edge. The double QW configuration on the right side in Fig. (4.3) contains only the two QWs in the center. If both structures are placed between Bragg-mirrors, the antinodes of the cavity mode are formed near the QWs and an optimal interaction of the photonic mode with the QW excitons is obtained. Due to the symmetry of both structures, the electric field distribution in each of the QWs is exactly the same.

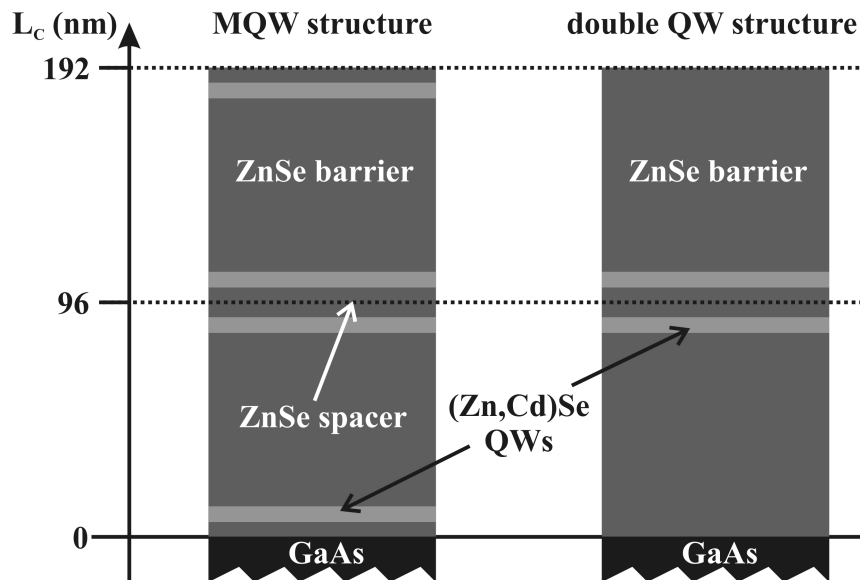


Figure 4.3: Cross-section drawing of a MQW structure with four (left side) and two (right side) (Zn,Cd)Se QWs, respectively. The resonator length of about 192 nm is adapted to the QW emission in the green spectral range. If both structures are enclosed between Bragg-mirrors, the electric field distribution is exactly the same in each of the QWs.

#### 4.2.1 Structural investigations of MQWs

Besides the in-situ RHEED-measurements described in Sec. (4.1), the MQW structures are characterized ex-situ by high resolution x-ray diffraction, to get detailed information about the structural parameters.

For detailed characterization of the strain state of a MQW structure similar to that in Fig. (4.3), left side, a reciprocal space map around the asymmetric GaAs-(224) Bragg-reflex has been measured. From such a measurement the reciprocal lattice parameters  $q_x$  and  $q_z$ , which are directly related to the lattice vectors in surface and growth direction, respectively, are extracted.

The reciprocal space map of the MQW structure McS-803 is shown in Fig. (4.4). The ZnSe Bragg-reflex is shifted to a lower  $q_x$  and  $q_z$  relatively to the GaAs reflex. This observation results from a tilt or a partial relaxation of the ZnSe. From the measurement

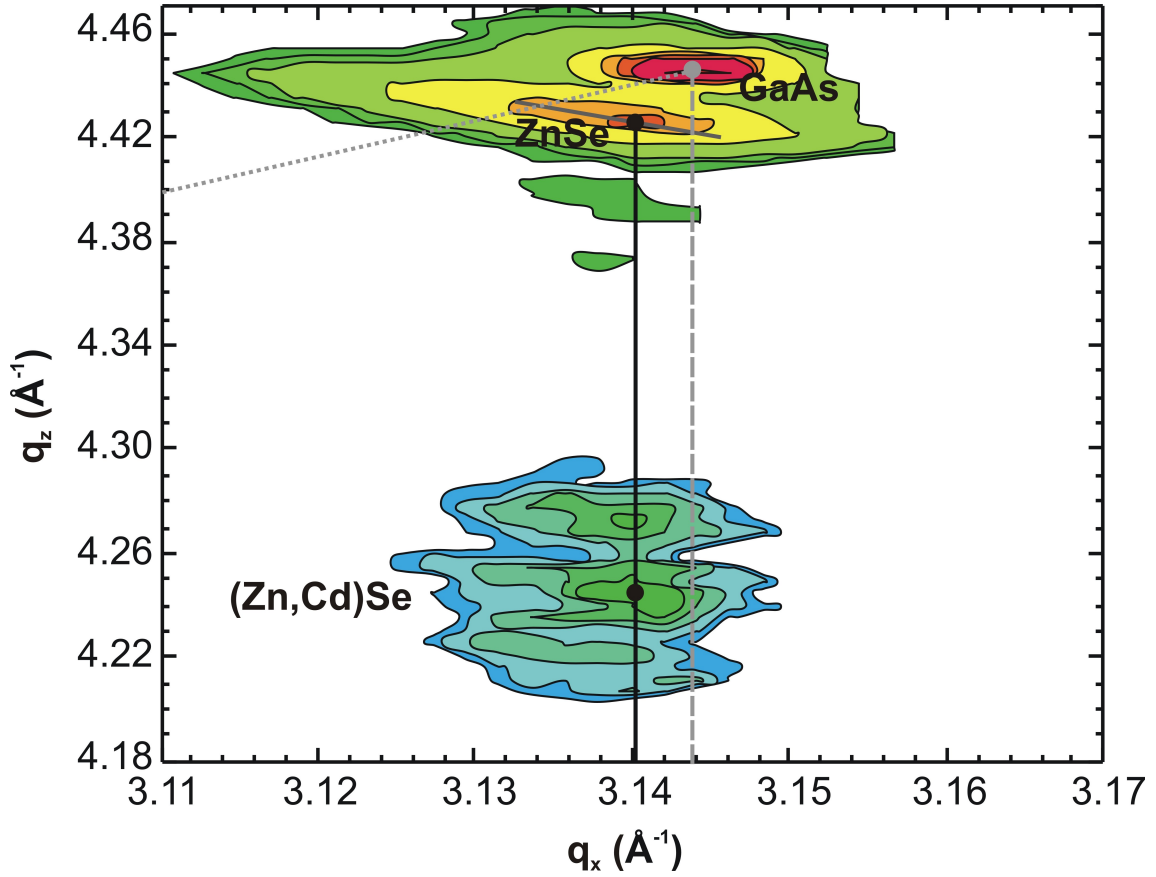


Figure 4.4: Reciprocal space map around the GaAs-(224) reflex of the MQW structure McS-803. The ZnSe reflex is observed on the dark grey line, which is the relaxation line for ZnSe. From the measured ZnSe peak position, the relaxation grade has been estimated of about 38 %. Furthermore the black line indicates that the (Zn,Cd)Se QWs are lattice matched on ZnSe.

of a symmetric reciprocal space map of the structure a tilt has been excluded, which denotes that the ZnSe layers are partial relaxed.

The dark grey line is the relaxation line for ZnSe. The points of intersection of the relaxation line with the dashed as well as the dotted grey line depict the peak position for fully strained and fully relaxed ZnSe on GaAs, respectively. From this geometric construction the relaxation of the ZnSe barriers has been estimated of about 38 %. The black line shows that the (Zn,Cd)Se QWs are lattice matched on ZnSe.

Hence now the strain state of the MQW structure McS-803 is well determined, the im-

portant structural parameters (i.e. thickness and mole fraction of the QWs as well as the cavity length) are obtained from the measurement of a symmetrical  $\omega - 2\theta$ -scan. Such a scan yields information about the lattice parameters in growth direction (i.e. perpendicular to the surface). With the full dynamical x-ray simulation theory [Kh2003, Pa2001] the measured spectrum is fitted by varying the lattice parameters of the materials as well as the thickness of (Zn,Cd)Se QWs and ZnSe barrier layers, respectively.

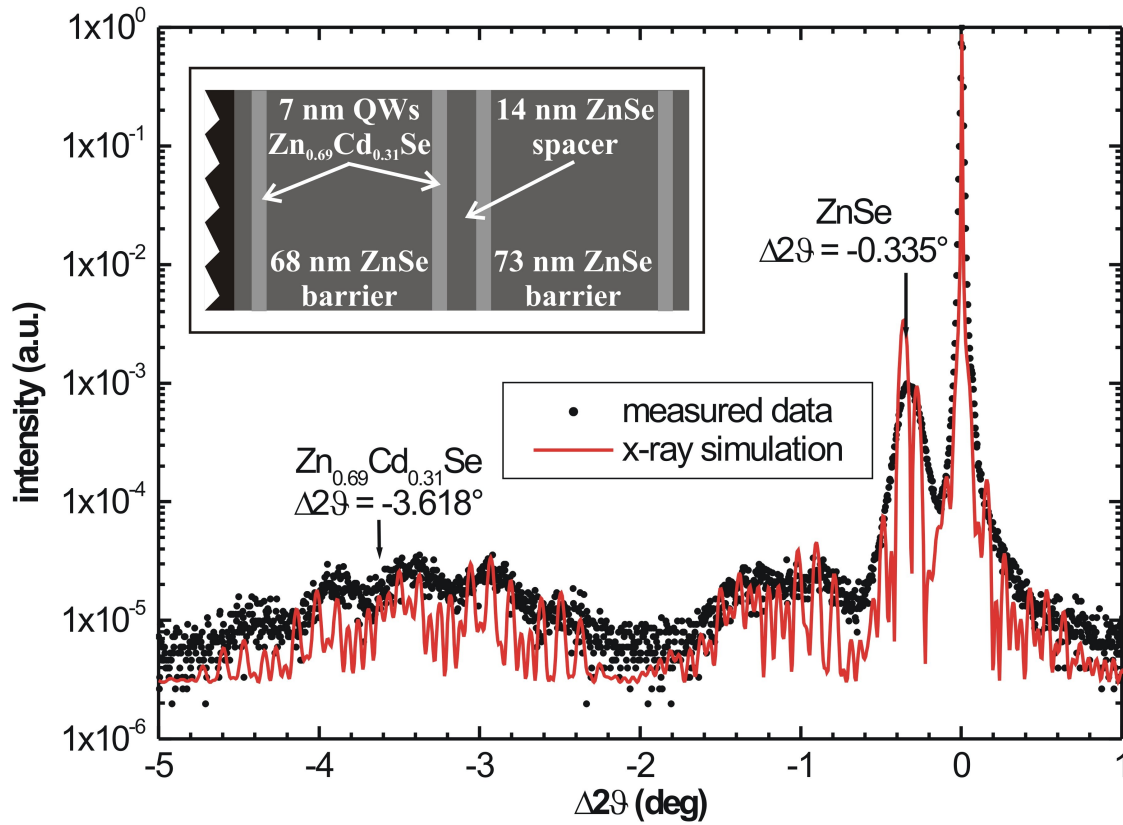


Figure 4.5: Symmetric  $\omega - 2\theta$ -scan of sample McS-803 (dots) measured relative to the GaAs-(004)-reflex. The red curve denotes the full dynamic x-ray diffraction simulation of the MQW structure. The GaAs and ZnSe peaks are clearly resolved, but the ZnSe peak is not superimposed by Pendellösung fringes as shown in the calculated data. The structural parameters of McS-803 in the small inset are obtained from the x-ray simulation (red curve).

Fig. (4.5) depicts the  $\omega - 2\theta$ -scan spectrum of the MQW structure McS-803 (dots) measured relative to the GaAs-(004) Bragg-reflex as well as the simulated data (red line).

The ZnSe reflex is clearly resolved at the relative angle  $\Delta 2\theta = -0.335^\circ$ , which is significantly smaller than that, calculated for a fully strained ZnSe layer on GaAs (i.e.  $\Delta 2\theta = -0.405^\circ$ ). This fact is in good agreement with the results in Fig. (4.4) and confirms the partial relaxation of the ZnSe. Furthermore no Pendellösung fringes are observed in the ZnSe reflex region of the measured spectrum, yielding a reduced crystallographic quality of the ZnSe barrier layers (i.e. dislocations at the GaAs/ZnSe heterointerface).

From a fit of the x-ray simulation to the experimental data. the structural properties of McS-803 are obtained. The results are illustrated in the small inset of Fig. (4.5). The (Zn,Cd)Se reflex has been estimated at  $\Delta 2\theta = -3.618^\circ$ , resulting in a cadmium mole fraction of  $x(\text{Cd}) = 0.31 \pm 0.02$ . Furthermore the (Zn,Cd)Se reflex is superimposed by Pendellösung fringes, from which a periodicity of  $22 \pm 1$  nm is obtained. The experimental results are in good agreement with the simulation data, yielding a QW thickness of  $d(\text{QW}) = 7.0 \pm 0.5$  nm and a ZnSe spacer layer thickness of  $14.0 \pm 0.5$  nm between the central QWs. For the two ZnSe barrier layers a thickness of  $68 \pm 5$  nm and  $73 \pm 5$  nm has been assumed in the calculation.

The crystallographic quality of the MQW structure is investigated by measuring a symmetric  $\omega$ -scan (the so-called "rocking-curve") of the (004)-reflex of ZnSe. The FWHM value of the peak in such a spectrum is directly related to the distribution of the in-plane lattice parameter. Due to the relaxation of an epitaxial layer, the dislocation density in the structure increases and results in a larger FWHM value of the Bragg-reflex in the  $\omega$ -scan spectrum.

Fig. (4.6) illustrates the  $\omega$ -scan spectrum of the MQW structure McS-1072, which has similar structural parameters as McS-803. The peak intensity is measured as a function of the relative difference  $\Delta\omega$  from the (004)-ZnSe Bragg-angle. The FWHM value of the peak is about  $\Delta\omega = 11.1 \pm 0.1$  arcmin, which is significantly larger than the FWHM value of fully strained ZnSe structures on GaAs (about 1 - 3 arcmin) [Wo1995].

The observations in Fig. (4.4) and Fig. (4.6) corroborate that the relaxation is induced

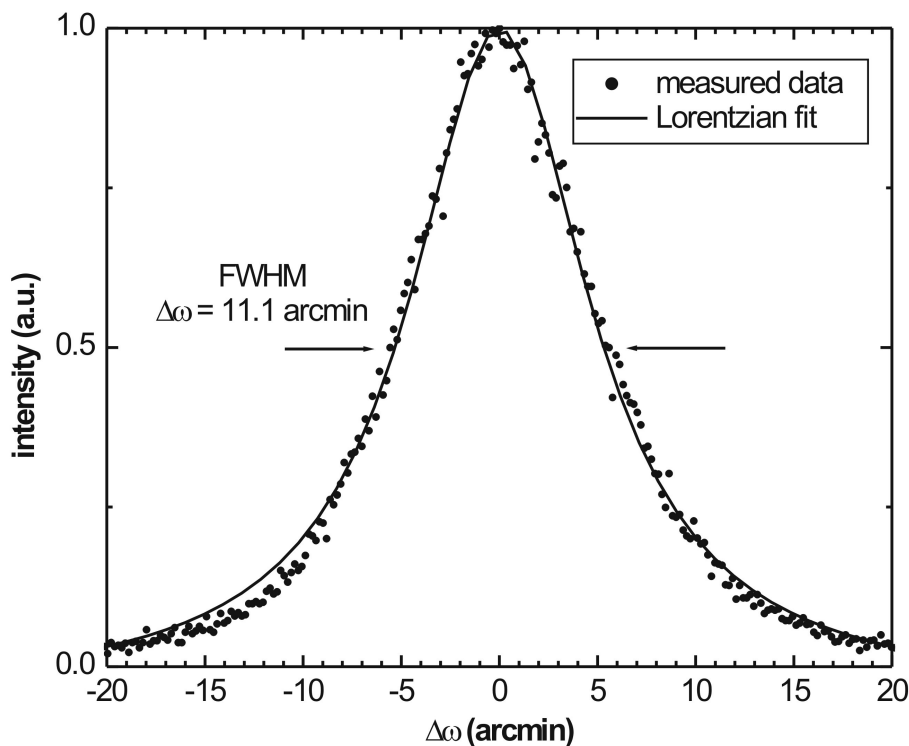


Figure 4.6: Symmetric  $\omega$ -scan of the (004)-reflex of ZnSe in the MQW structure McS-1072 (dots). The intensity distribution is measured as a function of the relative difference  $\Delta\omega$  from the ZnSe-(004) Bragg-angle. The FWHM value of  $\Delta\omega = 11.1 \pm 0.1$  arcmin is obtained by a Lorentzian fit (full curve) of the measured data.

during growth of the first ZnSe barrier layer and the dislocation density in the structure is increased. The strain energy near the GaAs/ZnSe heterointerface is unequivocally increased, due to the placement of the first (Zn,Cd)Se QW and accelerates the relaxation in the subsequent ZnSe barrier layer.

The influence of strain relaxation in the ZnSe barrier layers is reduced in a double QW structure. The design of such a structure is illustrated in Fig. (4.3), right side. In contrast to the MQW structure, the two (Zn,Cd)Se QWs near the GaAs/ZnSe interface and the ZnSe/air boundary are skipped.

The symmetrical  $\omega - 2\theta$ -scan of the double QW structure McS-775 (dots) measured around the GaAs-(004)-reflex is illustrated in Fig. (4.7). The relative angular difference

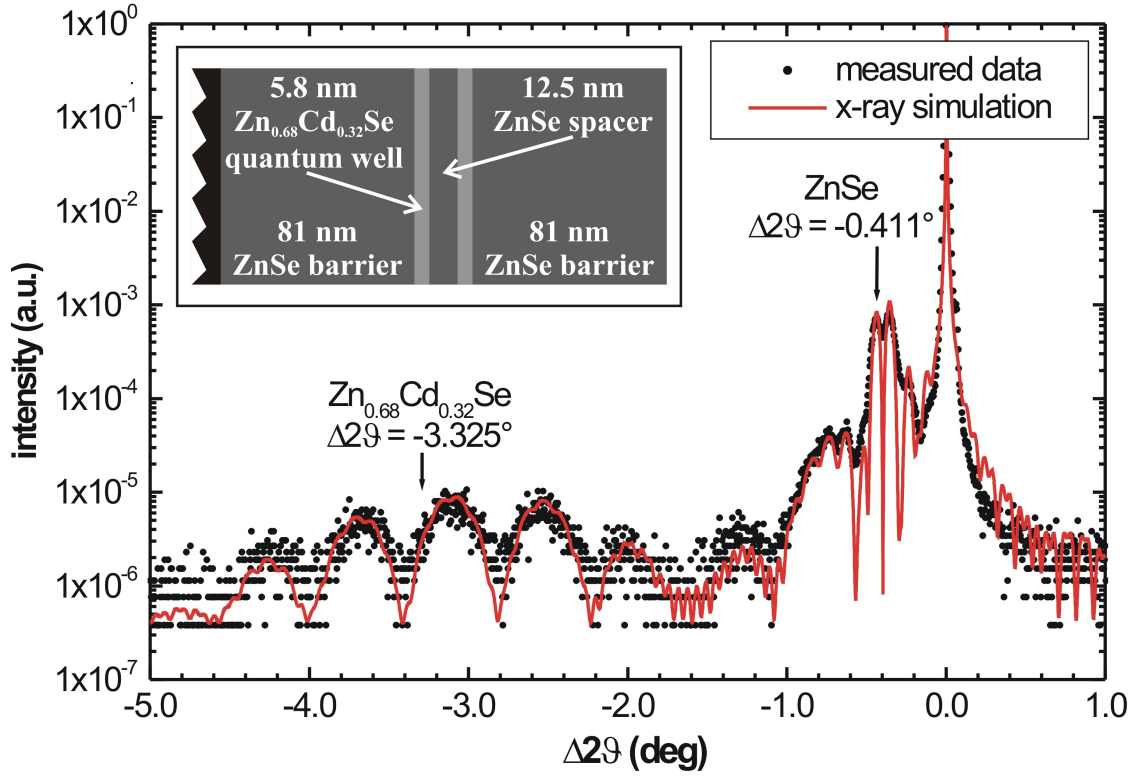


Figure 4.7: Symmetric  $\omega - 2\theta$ -scan of sample McS-775 (dots) measured relative to the GaAs-(004)-reflex. The red curve denotes the full dynamic x-ray diffraction simulation of the double QW structure. The GaAs and ZnSe peaks are clearly resolved and the ZnSe as well as the (Zn,Cd)Se peaks are superimposed by Pendellösung fringes. The structural parameters of McS-775 in the small inset are obtained from the x-ray simulation.

of the ZnSe- and GaAs-reflex in the x-ray spectrum is about  $\Delta 2\theta = -0.411^\circ$ . A comparison of this value with the data in Fig. (4.5) shows that the ZnSe layers in both structures have a different strain state. This observation has been analyzed via the concept of asymmetric reciprocal space maps in various similar double QW structures, yielding that the ZnSe layers as well as (Zn,Cd)Se QWs are fully strained on the GaAs substrate.

The angular position of the (Zn,Cd)Se reflex is calculated at  $2\theta = -3.325^\circ$  from the simulation parameters. Both, the ZnSe and the (Zn,Cd)Se peaks are superimposed by significant Pendellösung fringes, yielding the improved interface quality between the

materials in the fully strained double QW structure. The results, which are summarized in the small inset in Fig. (4.7), are obtained by simulation (red curve) of the measured x-ray spectrum (dots). The thickness of the QWs is about  $5.8 \pm 0.5$  nm with a cadmium mole fraction of  $x(\text{Cd}) = 0.32 \pm 0.02$ . The thickness of the ZnSe barriers is about  $81 \pm 2$  nm with a spacer layer of  $12.5 \pm 0.5$  nm between the central QWs.

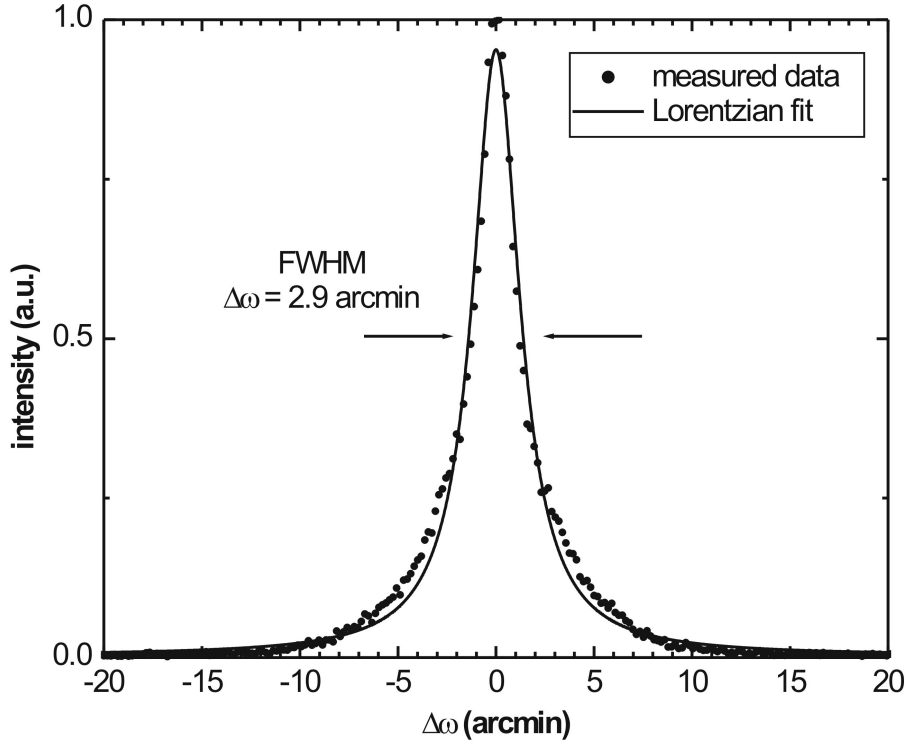


Figure 4.8: Symmetric  $\omega$ -scan of the ZnSe-(004)-reflex of the double QW structure McS-775 (dots). The intensity distribution is measured as a function of the relative difference  $\Delta\omega$  from the ZnSe-(004) Bragg-angle. The FWHM value of  $\Delta\omega = 2.9 \pm 0.1$  arcmin is obtained by a Lorentzian fit (full curve) of the measured data.

The  $\omega$ -scan of the double QW structure is illustrated in Fig. (4.8). In this case also the intensity distribution of the (004)-ZnSe reflex has been measured as a function of the relative angular difference  $\Delta\omega$  (dots), to get information about the crystallographic quality. From the Lorentzian fit of the measured spectrum (full curve) a FWHM value of  $\Delta\omega = 2.9 \pm 0.1$  arcmin is obtained. This value is significantly smaller compared to

the FWHM value of the  $\omega$ -scan spectrum in Fig. (4.6), which has been measured on the MQW structure.

This result shows that the crystallographic quality of the fully strained double QW structure is at least four times better than that of the MQW configuration with partial relaxed ZnSe barriers. Despite this structural advantage, the polariton splitting is reduced by a factor of two in a double QW microcavity, hence the number of QWs determines the Rabi-splitting energy.

### 4.2.2 Optical properties of ZnSe/(Zn,Cd)Se MQWs

Due to the fact that the transition energy and the FWHM of the QW emission mainly determines the conditions for the observation of the strong coupling, the optical properties of the (Zn,Cd)Se QWs are as important as the structural parameters.

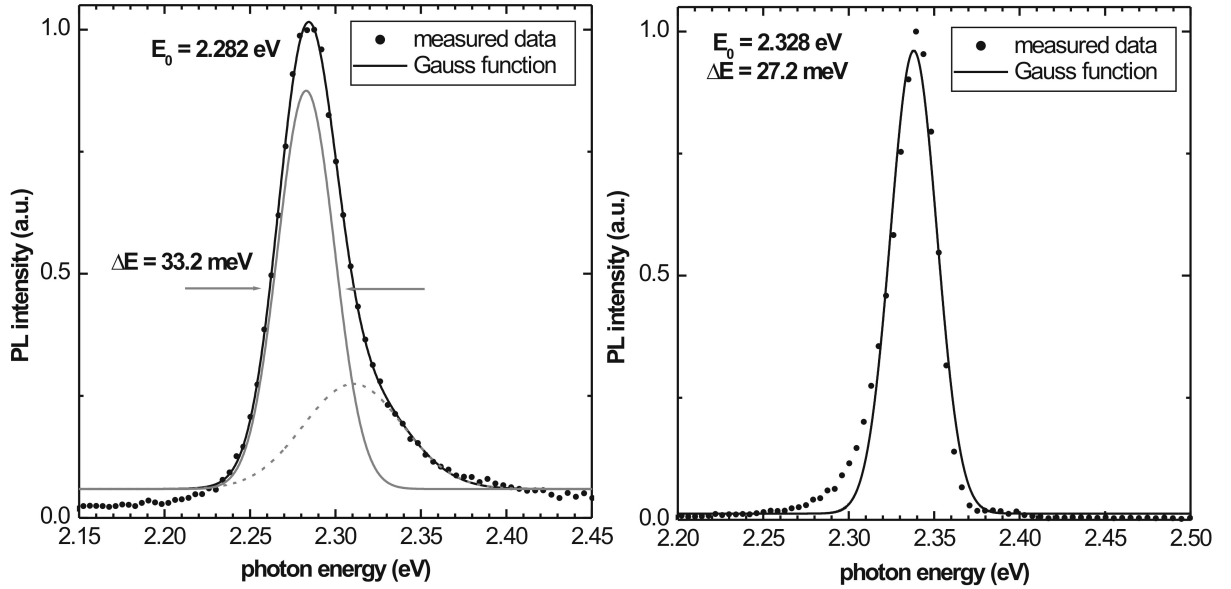


Figure 4.9: PL spectra of the MQW structure McS-1072 at room temperature (left side) and 4.3 K (right side), respectively. **Left side:** The measured spectrum (dots) is fitted with two Gaussian functions, where the full grey curve depicts the QW transition at  $E_0 = 2.282 \text{ eV}$  with an emission FWHM of about 33 meV. The dotted grey curve considers the thermal luminescence broadening. **Right side:** At 4.3 K a QW transition at  $E_0 = 2.328 \text{ eV}$  with a FWHM of about 27 meV is observed.

The PL spectra of the MQW structure McS-1072 are summarized in Fig. (4.9) at room temperature (left side) and liquid helium temperature (right side), respectively. The room temperature spectrum (dots) is fitted with two Gaussian functions, where the full grey curve depicts the homogenous QW transition at  $E_0 = 2.282$  eV with an emission FWHM of about 33 meV. The dotted grey curve considers luminescence broadening due to thermal activation of transitions between higher quantum states and has a FWHM value of about 58 meV.

In the low temperature PL spectrum on the right side in Fig. (4.9) a QW transition at  $E_0 = 2.328$  eV with a FWHM of about 27 meV is observed. This value reflects the inhomogeneous broadening in the structure due to fluctuations of strain, thickness and cadmium mole fraction of the QWs. The typical low temperature luminescence FWHM of high quality ZnSe/(Zn,Cd)Se QWs is about 8-12 meV [Se2000]. The luminescence is shifted about 46 meV to higher energy compared to the room temperature emission.

Fig. (4.10) depicts the PL spectra of the double QW structure McS-772 as described in the small inlay in Fig. (4.7) at room temperature (left side) as well as at 5 K (right side), respectively. The room temperature spectrum (dots) is fitted with two Gaussian functions (grey curves). The FWHM of the QW transition, which is about 23 meV, is clearly smaller than it has been measured on the MQW structure. The FWHM of the second peak (dotted grey curve), which reflects the thermal broadening, is about 66 meV. This value is in good agreement with the PL data of the MQW structure in Fig. (4.9).

Considering time dependent fluctuations of the metal fluxes during MBE processing, the cadmium mole fraction of the outer QWs in the MQW structure might deviate from the mole fraction of the central QWs, which are grown in a small time interval of about five minutes. This fact results in an increased emission linewidth compared to the double QW structure, in which only the two central QWs contribute to the luminescence.

The low temperature PL spectrum of the double QW structure is illustrated on the right side of Fig. (4.10) as well as the Gaussian fit function. The QW transition at  $E_0 = 2.483$  eV has a linewidth with a FWHM of about 9 meV, which is significantly smaller compared

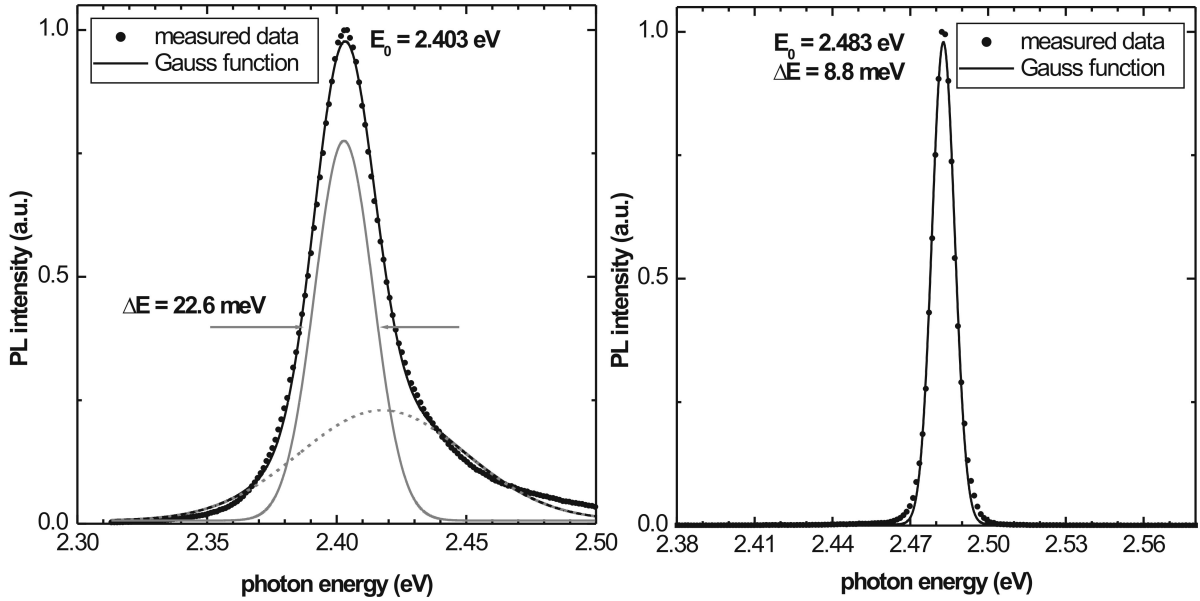


Figure 4.10: PL spectra of the double QW structure McS-772 at room temperature (left side) and 4.3 K (right side), respectively. **Left side:** The measured spectrum (dots) is fitted with two Gaussian functions. The full grey curve represents the QW transition at  $E_0 = 2.403$  eV with an emission FWHM of about 23 meV. The second peak (dotted grey curve) considers the thermal broadening effect. **Right side:** At 4.3 K a homogenous transition peak at  $E_0 = 2.483$  eV with a FWHM of about 9 meV is observed.

to the transition FWHM value in the low temperature spectrum of the MQW structure. This observation reveals that the inhomogeneous broadening of the emission is significantly reduced in case of the double QW structure. Considering the structural properties of the MQW structure, as described in Sec. (4.2.1), the additional inhomogeneous broadening of the PL emission results from the partial relaxation of the active layer.

### 4.3 ZnSe/(Zn,Cd)Se superlattice structures

In Sec. (4.2.1) and Sec. (4.2.2) it has been shown that MQW structures with four QWs arranged as indicated in Fig. (4.3), left side, are influenced by the partial relaxation of the ZnSe barriers. This aspect results in an increased inhomogeneous broadening of the luminescence. This effect is reduced in a fully strained double QW structure, but yields

the disadvantage that the number of QWs in the microcavity is reduced by a factor of two.

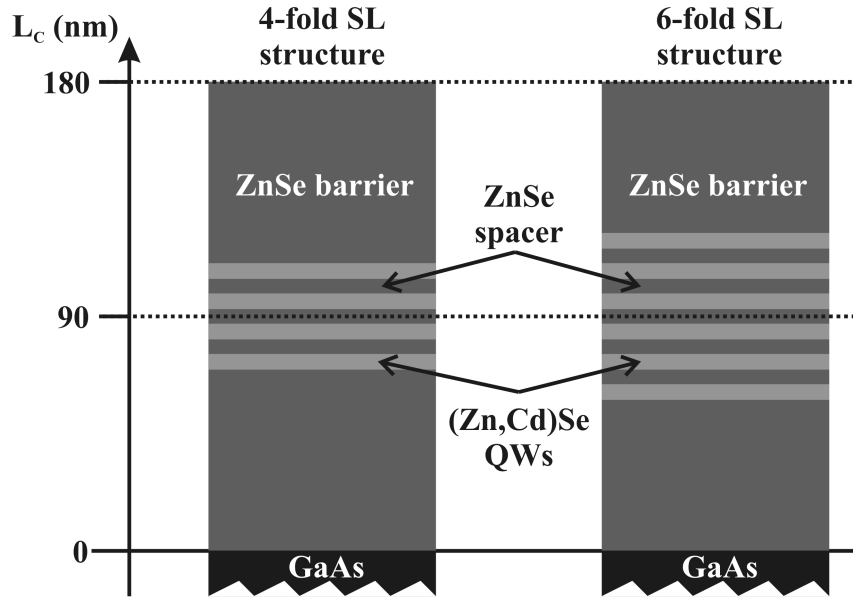


Figure 4.11: Cross-section drawing of typical SL structures with four (left side) and six (right side) (Zn,Cd)Se QWs, respectively, as a superlattice. The resonator length of about 180 nm is adapted to the QW emission in the blue-green spectral range. The thickness of (Zn,Cd)Se QWs and ZnSe barriers is reduced to diminish the strain energy in the structure.

Therefore the design of the active layers is modified as it is illustrated in Fig. (4.11). Firstly the number of QWs in the center of the structure is increased and secondly the thickness of the (Zn,Cd)Se QWs as well as the ZnSe spacer layers is reduced. In this case a better crystal quality might be achieved, due to the absence of a large strain field near the sensitive GaAs/ZnSe heterointerface and the ZnSe barrier relaxation is inhibited. Furthermore the compact arrangement of the QWs promise a better reproducibility of their structural parameters (i.e. thickness and cadmium mole fraction) and the strain is distributed homogenously along all QWs.

Nevertheless, an increase of the PL transition linewidth, due to QW coupling in the SL structure has to be considered. Additionally to this, the exciton distribution in the QWs

with respect to the photonic field distribution is different. In the SL microcavities the outer QWs have a weaker coupling to the photonic mode, due to their increased distance from the antinodes of the standing wave.

### 4.3.1 Structural properties of superlattice structures

Fig. (4.12) shows an asymmetric reciprocal space map around the GaAs-(224)-reflex of the four-fold SL structure McS-851, similar to that, which is described in Fig. (4.11), left side. The ZnSe Bragg-reflex as well as the superlattice peaks SL 0 and SL-1 are well

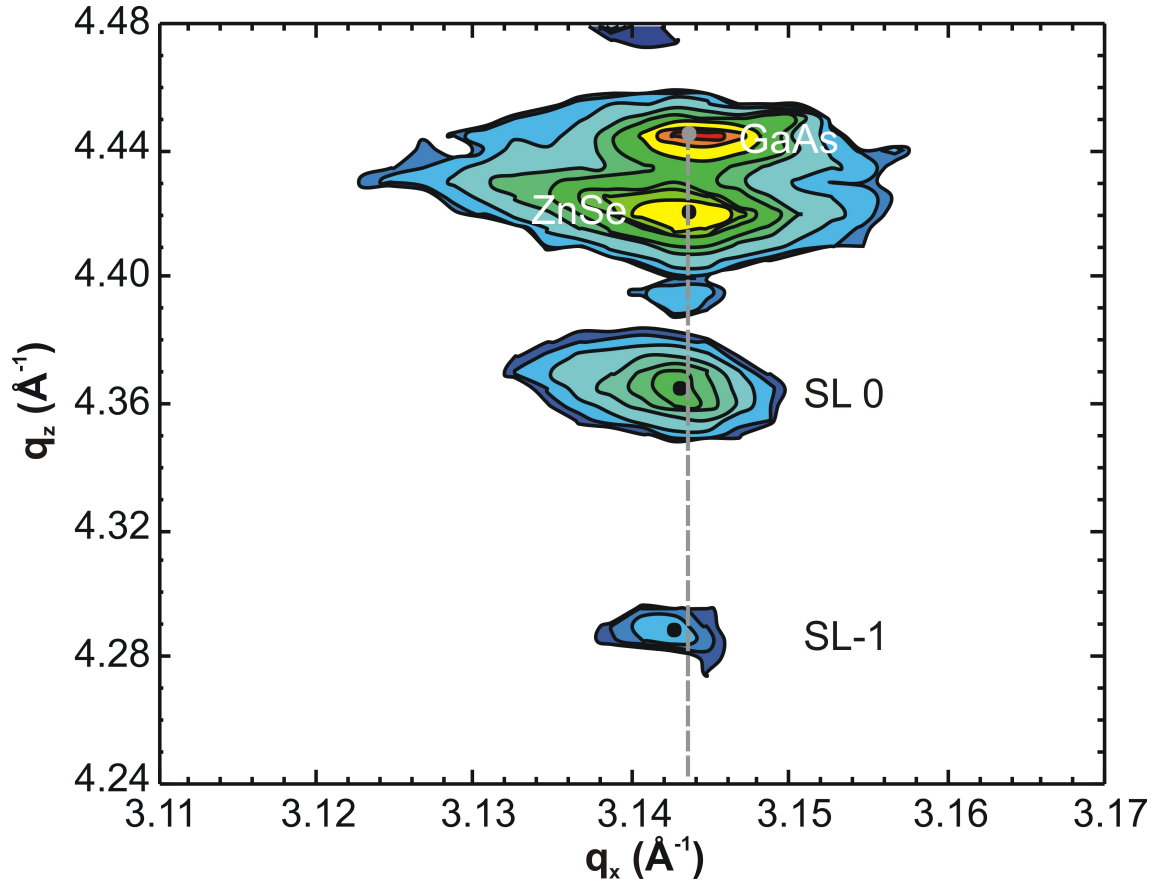


Figure 4.12: Reciprocal space map around the GaAs-(224)-reflex of the SL structure McS-851. The ZnSe reflex is observed on the grey line, which indicates the  $q_x$  lattice vector in reciprocal space for a fully strained lattice on GaAs. The superlattice peaks SL-1 and SL 0 are also clearly resolved at the same  $q_x$  as the ZnSe reflex.

resolved in the reciprocal space map. The grey dashed line indicates the  $q_x$  lattice vector in reciprocal space, yielding that the ZnSe barriers as well as the QWs and the spacer layers are fully strained on the GaAs substrate.

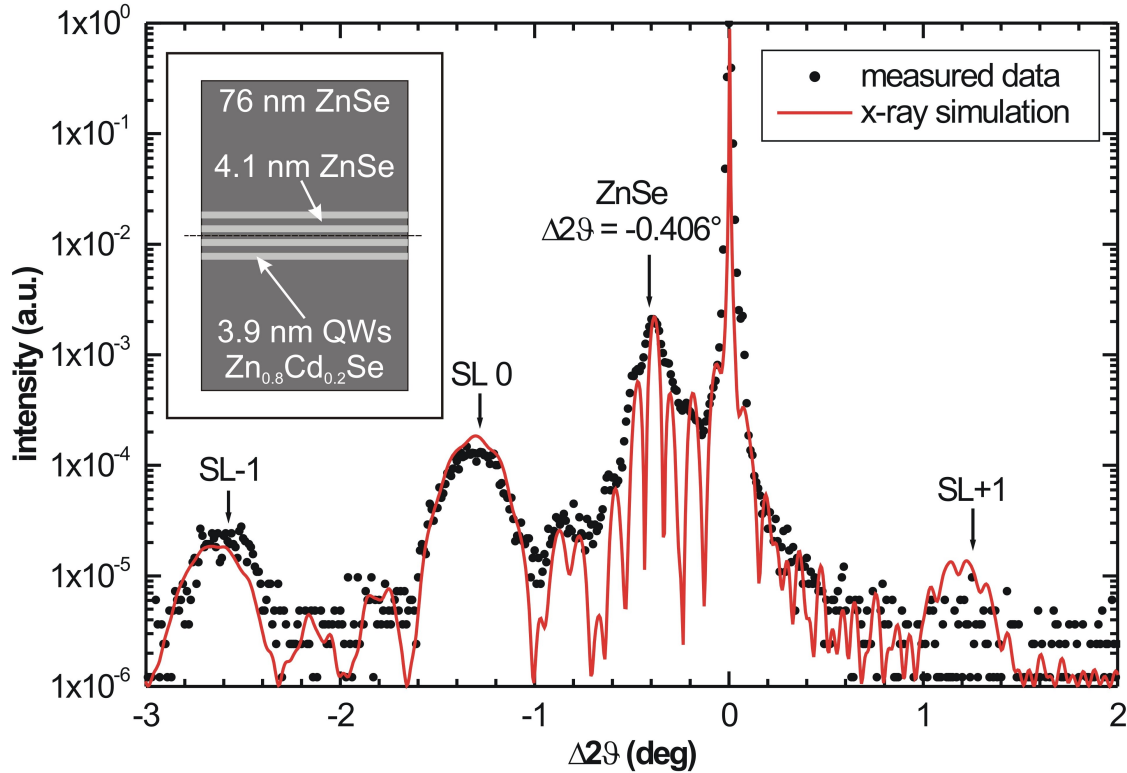


Figure 4.13: Symmetric  $\omega - 2\theta$ -scan of the SL structure McS-851 (dots) with four QWs. The scan is measured relative to the GaAs-(004)-reflex. The ZnSe peak is resolved at  $\Delta 2\theta = -0.406^\circ$  and also three superlattice peaks (SL+1, SL 0 and SL-1) are observed in the spectrum. From their relative angular distance, a superlattice period of 8.0 nm is estimated. The important structural parameters are extracted from the full dynamical x-ray diffraction simulation (red curve) of the measured spectrum and summarized in the cross-section drawing in the small inset.

Hence the ZnSe layers as well as the (Zn,Cd)Se QWs are fully strained on GaAs, the important structural parameters are obtained from a symmetric  $\omega - 2\theta$ -scan. Fig. (4.13) shows the  $\omega - 2\theta$ -scan of the SL structure McS-851 (dots) with four QWs measured relative to the GaAs-(004)-reflex. The relative angular difference between the ZnSe- and the GaAs-(004)-reflex is about  $\Delta 2\theta = -0.406^\circ$ . This value is in good agreement with

the relative angular position of fully strained ZnSe on GaAs (i.e.  $\Delta 2\theta = -0.405^\circ$ ) and confirms the results of Fig. (4.12).

From the Pendellösung fringes, which superimpose the ZnSe peak in the spectrum, a ZnSe barrier layer size of  $76 \pm 2$  nm is estimated. The three additional Bragg-reflexes SL-1, SL 0 and SL+1 stem from the periodicity of the (Zn,Cd)Se superlattice. The relative angular position of SL 0 is directly related to the composition of the (Zn,Cd)Se layers as well as the thickness ratio between the ZnSe spacer and the (Zn,Cd)Se QWs [Kh2003]. From the relative angular distance between the superlattice peaks, the periodicity of the structure (i.e. the sum of the thickness of ZnSe spacer and (Zn,Cd)Se QW is obtained.

The x-ray simulation spectrum (red curve) in Fig. (4.13) yields the best fit to the experimental data, An accurate characterization of the structural properties of sample McS-851 is performed. The structural properties are summarized in the small inlay in Fig. (4.13). The thickness of the (Zn,Cd)Se QWs is about  $3.9 \pm 0.2$  nm with a cadmium mole fraction of  $0.20 \pm 0.01$ , and the thickness of the ZnSe spacer layers between the QWs is about  $4.1 \pm 0.2$  nm.

One of the important features of the x-ray spectrum in Fig. (4.13) are the Pendellösung fringes in the ZnSe reflex. These fringes indicate a good interface quality between ZnSe barriers and QWs and are as well resolved as in the spectrum of the double QW structure in Fig. (4.7).

Fig. (4.14) illustrates the  $\omega$ -scan spectrum (dots) of McS-851. The intensity is measured as a function of the relative angular difference from the ZnSe-(004)-reflex Bragg-angle. The spectrum is fitted with a Lorentzian function and a FWHM value of  $\Delta\omega = 1.9 \pm 0.1$  arcmin is obtained.

The  $\omega$ -scan FWHM value of McS-851 is about half an order of magnitude smaller than that of the partial relaxed MQW structure McS-803. This result corroborates the improved crystallographic quality of the SL structure, which is fully strained on the GaAs substrate. Due to the fact, that thickness and cadmium mole fraction of the QWs are reduced in McS-851, the  $\omega$ -scan FWHM value is in fact significantly smaller than that of the fully

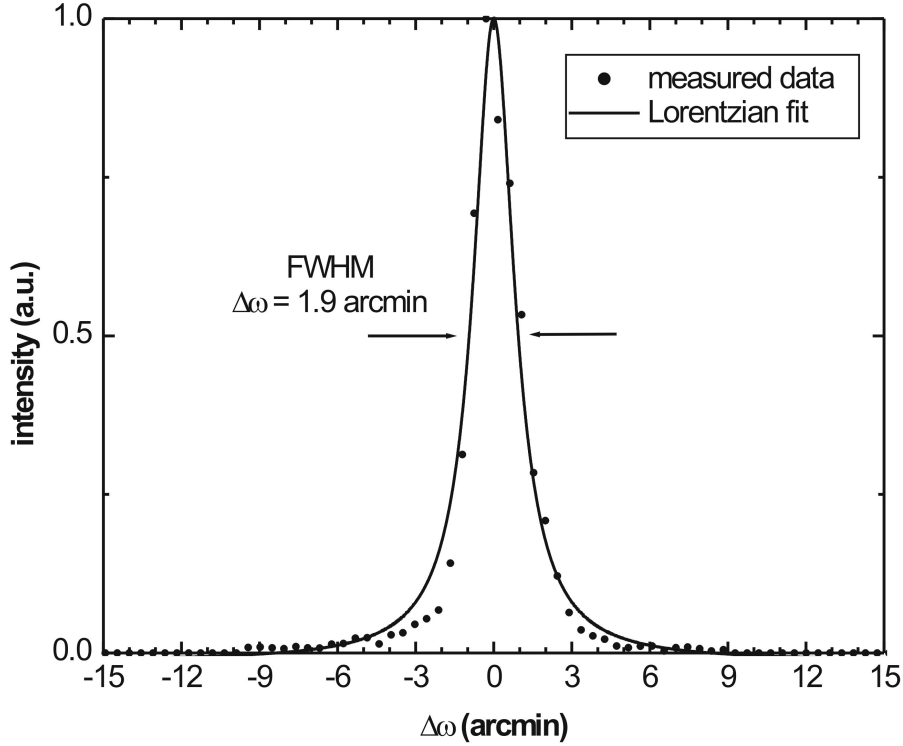


Figure 4.14: ZnSe-(004)-reflex  $\omega$ -scan of the SL structure McS-851 (dots). The intensity distribution is measured as a function of the relative difference  $\Delta\omega$  from the ZnSe Bragg-angle. The FWHM value of  $\Delta\omega = 1.9 \pm 0.1$  arcmin is obtained by a Lorentzian fit (full curve) of the measured data.

strained double QW structure McS-775.

The most important parameter regarding the SL configuration is the number of QWs, which can be integrated in the active layer, to increase the oscillator density and therefore the Rabi-splitting in a SL microcavity. Analyzed via this concept, a significant reduction of the crystallographic quality, which results from a relaxation of the QWs might be observed. In case of the MQW structure the number of QWs is limited by four, as shown in the previous section.

The  $\omega - 2\theta$ -scan spectrum of the six-fold SL structure McS-1014 (dots) measured relative to the GaAs-(004)-reflex is illustrated in Fig. (4.15). The relative angular difference between the ZnSe- and the GaAs-(004) Bragg-reflex is about  $\Delta 2\theta = -0.403^\circ$ . The comparison of this value with the data of McS-851 in Fig. (4.13) and Fig. (4.12) shows

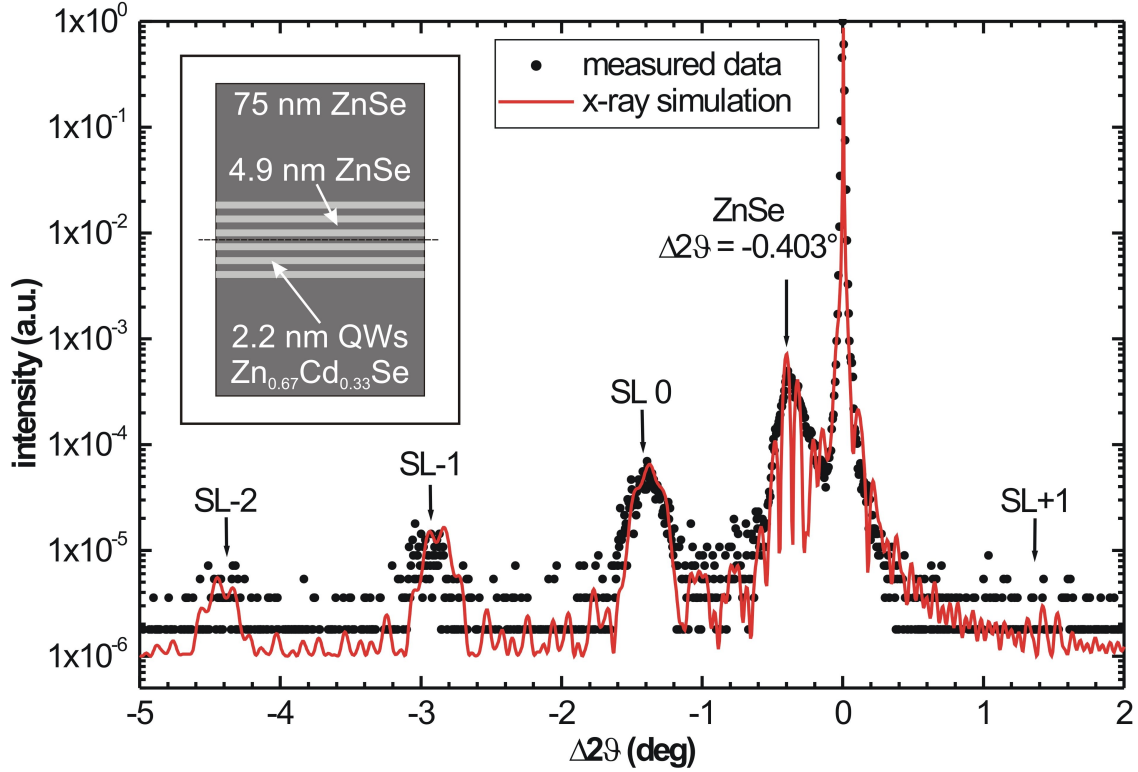


Figure 4.15: ZnSe-(004)-reflex  $\omega - 2\theta$ -scan of the six-fold SL structure McS-1014. The ZnSe peak is measured at  $\Delta 2\theta = -0.403^\circ$ , yielding fully strained barrier layers. Furthermore four superlattice peaks (SL+2, SL+1, SL 0 and SL-1) are resolved in the spectrum. A superlattice period of 7.1 nm and a cadmium mole fraction of about 0.33 is estimated from the relative angular distance of the SL peaks. The structural parameters of McS-1014, which are summarized in the inset, are performed by the x-ray diffraction simulation (red curve).

that McS-1014 is also fully strained on the GaAs substrate. Despite that, the typical Pendellösung fringes, which superimpose the ZnSe peak in the four-fold SL structure, are scarcely resolved in Fig. (4.15).

The structural parameters of McS-1014 are extracted from the x-ray simulation (red curve) of the  $\omega - 2\theta$ -scan spectrum (dots) and summarized in the small inset in Fig. (4.15). Four superlattice peaks are clearly resolved in the measured data and a superlattice period of  $7.1 \pm 0.1$  nm is obtained. The cadmium mole fraction of  $0.33 \pm 0.01$  is calculated from the relative angular position of the SL 0 reflex.

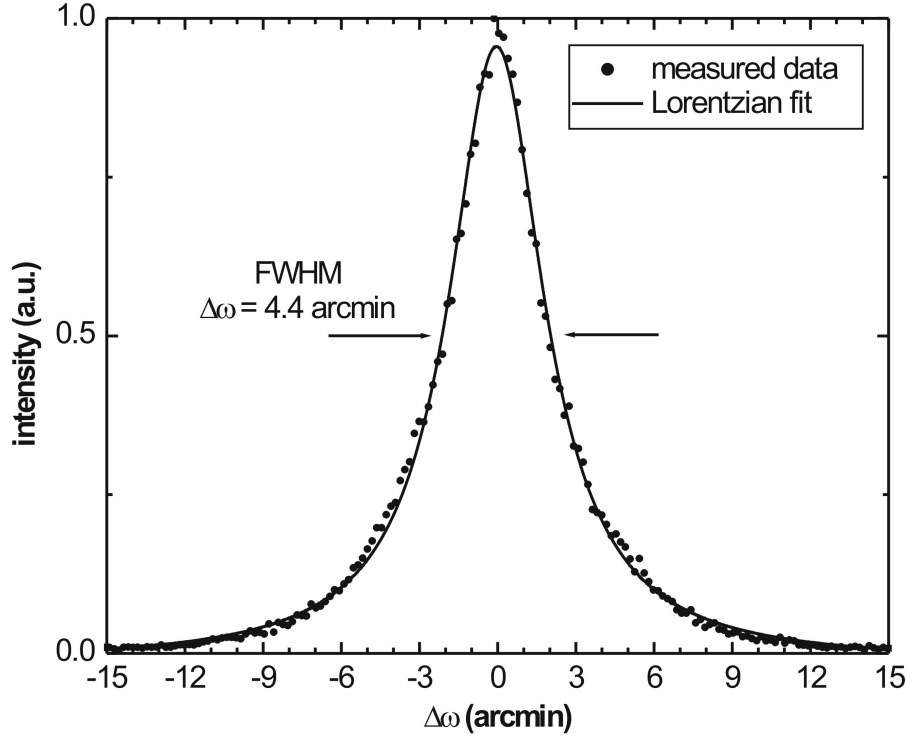


Figure 4.16: ZnSe-(004)-reflex  $\omega$ -scan spectrum of the six-fold SL structure McS-1014 (dots). The intensity distribution is measured as a function of the relative difference  $\Delta\omega$  from the ZnSe Bragg-angle. The FWHM value of  $\Delta\omega = 4.4 \pm 0.1$  arcmin is obtained by a Lorentzian fit (full curve) of the measured spectrum.

Fig. (4.16) depicts the ZnSe-(004)-reflex  $\omega$ -scan spectrum of the six-fold SL structure McS-1014. The spectrum is fitted by a Lorentzian function and a FWHM value of  $\Delta\omega = 4.4 \pm 0.1$  arcmin is obtained, which is about a factor of two larger than that of the four-fold SL structure in Fig. (4.14). This result is consistent with the degradation of the interface quality (reduction of the Pendellösung fringes), which is observed in the  $\omega - 2\theta$ -scan spectrum in Fig. (4.15). The reduced interface quality of McS-1014 stems from the substantial increased cadmium mole fraction ( $x(\text{Cd}) = 0.33$ ) compared to that of McS-851 ( $x(\text{Cd}) = 0.20$ ). The increased cadmium mole fraction in McS-1014 ensures a better exciton confinement at room temperature.

The  $\omega$ -scan spectrum FWHM value of the six-fold SL sample is about 50 % larger

in comparison to the data of the double QW structure McS-775 in Fig. (4.8), despite similar structural properties according to cadmium mole fraction and the entire thickness of all (Zn,Cd)Se QWs. Nevertheless, the investigation of several SL structures clearly shows an improvement of the structural quality compared to that of the MQW samples. Additionally to this, it is possible to increase the number of QWs up to six in the SL structures.

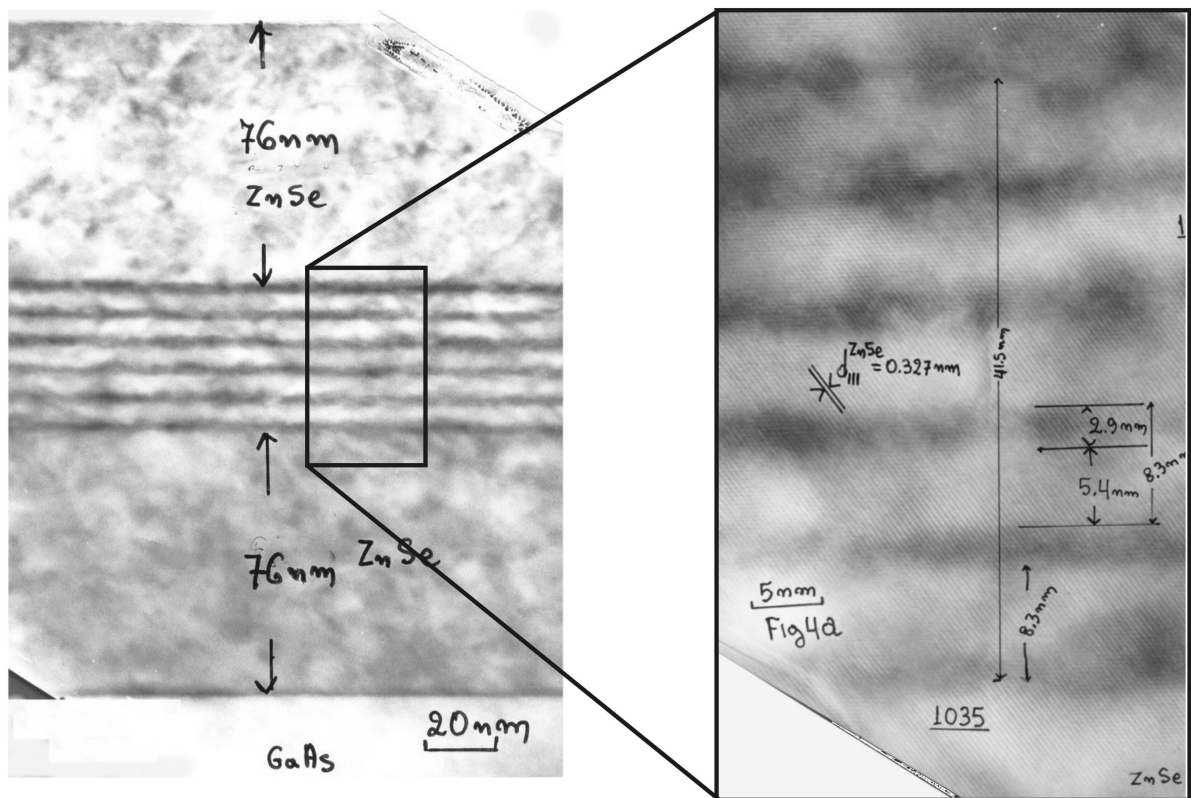


Figure 4.17: Cross section TEM-picture of a six-fold SL structure McS-1035. **Left side:** Overview of the whole structure. The six (Zn,Cd)Se QWs (dark color) are sandwiched between 76 nm ZnSe barriers. The strain contrast reveals excellent homogeneity of the QWs and spacer layers. **Right side:** Detailed view of the QW superlattice region in atomic resolution. The superlattice period is about 8.3 nm divided up into 2.9 nm QWs and 5.4 nm ZnSe spacers. The strain contrast reveals slightly fluctuations of thickness and cadmium mole fraction of the QWs.

Fig. (4.17) depicts a cross-section TEM-picture of the six-fold SL structure McS-1035.

On the left side the strain contrast of the whole structure is resolved. The dark regions are the six (Zn,Cd)Se QWs enclosed in 76 nm ZnSe barriers (bright regions). The picture demonstrates the excellent uniformity of the crystallographic structure. On the right side of Fig. (4.17) the SL region is illustrated in atomic resolution. Slightly fluctuations of the strain contrast reveal small variations in thickness and cadmium mole fraction of the (Zn,Cd)Se QWs on atomic scale.

The superlattice period is about 8.3 nm divided up into 2.9 nm (Zn,Cd)Se QWs and 5.4 nm ZnSe spacers in between. From the MBE growth parameters of the structure a barrier thickness of 73 nm, a QW thickness of 2.5 nm and a ZnSe spacer thickness of 5.0 nm is obtained. These values are in excellent agreement with the real structural parameters measured on the TEM investigations.

### 4.3.2 Photoluminescence investigation of SL structures

Hence a coupling of the QWs has to be considered in the SL structures, the optical properties are different compared to that of MQW structures. For the estimation of the (Zn,Cd)Se QW transition energy, the finite barrier model for fully strained QWs is used, yielding an excellent agreement between PL data and structural properties [Pa2001]. The penetration depth of the electron and hole wavefunction in the ZnSe barrier layers is estimated of about 2.5-4.0 nm for typical QW configurations with a cadmium mole fraction of 0.20-0.38 as well as a QW thickness of 3-5 nm.

The PL spectra (dots) of the four-fold SL structure McS-851 at room (left side) as well as at low temperature (right side) are illustrated in Fig. (4.18). The room temperature spectrum is fitted by two Gauss functions to consider the QW transition (full grey curve) at  $E_0 = 2.526$  eV and additionally thermal activation of transitions between higher quantum states (dotted grey curve). The FWHM value of about  $\Delta E = 23$  meV of the room temperature luminescence is nearly equal to that of the uncoupled double QW structure in Fig. (4.10).

In contrast to this, the low temperature PL transition in Fig. (4.18), right side, is observed

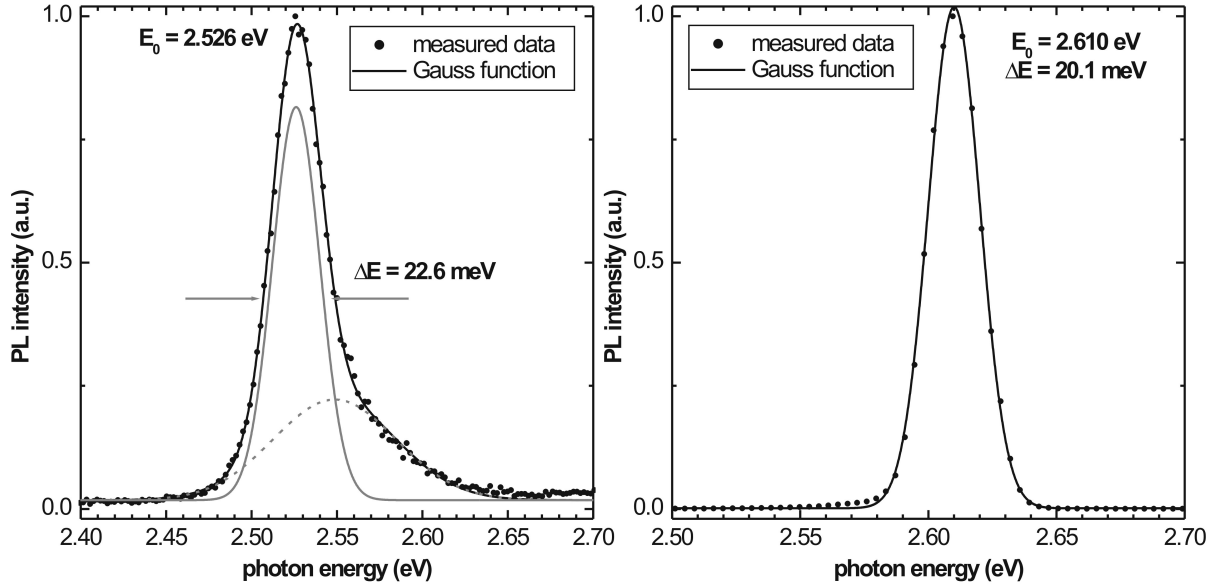


Figure 4.18: PL spectra (dots) of the four-fold SL structure McS-851 at room temperature (left side) and 4.3 K (right side), respectively. **Left side:** The measured spectrum is fitted with two Gauss functions, to consider the QW transition (full grey curve) as well as thermal luminescence broadening (dotted grey curve). The best fit yields a transition energy of  $E_0 = 2.526$  eV with a FWHM value of about  $\Delta E = 23$  meV. **Right side:** At 4.3 K the PL spectrum is fitted by one Gaussian function. The QW transition is observed at  $E_0 = 2.610$  eV with a FWHM value of about  $\Delta E = 20$  meV.

at  $E_0 = 2.610$  eV with a FWHM value of about  $\Delta E = 20$  meV. This FWHM value is about two times larger compared to that of the double QW structure. This fact confirms an increase of the luminescence broadening, due to the QW coupling in the SL structure.

Fig. (4.19) depicts the PL spectra measured at the six-fold SL structure McS-1014. The PL measurements show results similar to that of the four-fold SL structure McS-851, although the cadmium mole fraction and the number of QWs is increased in McS-1014. At room temperature the luminescence transition energy is  $E_0 = 2.470$  eV with a slightly larger FWHM value of about  $\Delta E = 24$  meV. Both effects, a lower luminescence energy and an increased FWHM value, respectively, stem from the increased cadmium mole fraction of the QWs in the six-fold SL sample.

The low temperature PL spectrum Fig. (4.19), right side, is fitted with a Gauss function,

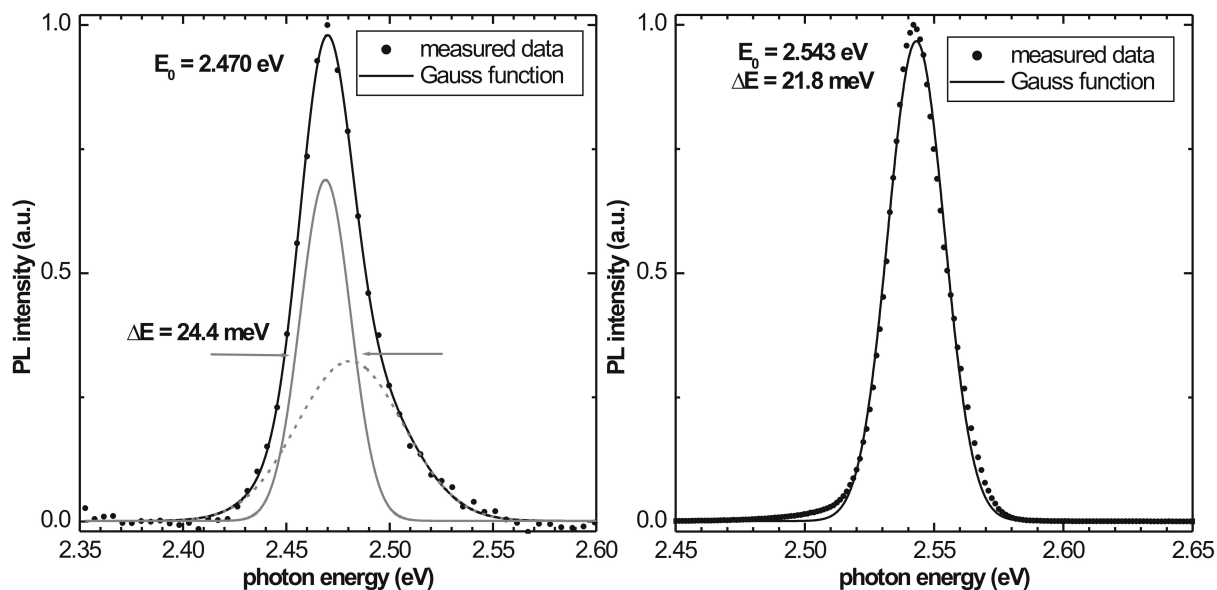


Figure 4.19: PL spectra (dots) of the six-fold SL structure McS-1014 at room temperature (left side) and 4.3 K (right side), respectively. **Left side:** The measured spectrum is fitted with two Gauss functions (grey curve), the best fit yields a transition energy of  $E_0 = 2.470$  eV with a FWHM value of about  $\Delta E = 24$  meV. **Right side:** At 4.3 K the PL spectrum is fitted by one Gauss function, yielding a transition energy of  $E_0 = 2.543$  eV with a FWHM value of  $\Delta E = 22$  meV.

yielding a transition energy of  $E_0 = 2.543$  eV with a FWHM value of  $\Delta E = 21.8$  meV. The luminescence FWHM value is in good agreement with the results of the low temperature luminescence of the four-fold SL structure.

Despite the reduced crystallographic quality of the six-fold SL structure (see also Fig. (4.14) and Fig. (4.16)), the luminescence properties of both SL structures are equivalent. This observation yields that at least up to six QWs are successfully included into SL structures without any significant degradation of the structural and the optical properties.

# 5 II-VI semiconductor microcavity structures

## 5.1 The combination of Bragg-mirrors and active layer to complete microcavities

In the previous two chapters the optimization of ZnS/YF<sub>3</sub> and ZnSe/YF<sub>3</sub>-Bragg mirrors as well as the design of the active layer containing up to six ZnSe/(Zn,Cd)Se QWs has been reported. The main focus of this section is the combination of Bragg-mirrors and active layer to a complete microcavity, which opens up the possibility to investigate the photon-exciton interaction. Main efforts have been performed to measure the strong coupling and especially the polariton anticrossing behavior in such microcavities at room temperature.

Fig. (5.1) shows a cross-line drawing of a ZnSe based microcavity structure with four (Zn,Cd)Se QWs in the center as the active layer, a six-fold stack of ZnSe/YF<sub>3</sub> Bragg-mirrors on the front side and an eight-fold stack on the rear side, respectively. The microresonator is optimized to emission at  $\lambda = 517$  nm, which results in a resonator length of about  $L_C = \frac{\lambda}{n_C} = 190$  nm. The thickness gradient of the cavity, which is exaggeratedly drawn in Fig. (5.1), is about  $\Delta L_C = 1\% \text{ mm}^{-1}$ .

The reflectivity of this structure can be calculated with the Transfer-Matrix model described in Sec. (2.2) as a function of the cavity length. The spectra are illustrated in

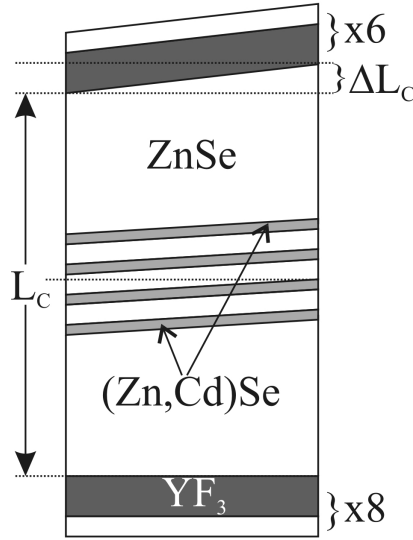


Figure 5.1: Cross-section drawing of a typical ZnSe/(Zn,Cd)Se SL structure with four QWs in the center as well as an eight-fold stack of ZnSe/ $YF_3$  DBRs rear mirror and a six-fold stack of DBRs front mirror, respectively.  $\Delta L_C$  is the cavity thickness gradient, which is implemented during growth of the active layer with the nominal resonator length  $L_C$ .

Fig. (5.2) (full curves). With decreasing cavity length, the photonic mode (indicated by the grey line) shifts to higher energy, while the QW transition energy (black dashed line) is constant. Due to the strong coupling, the absorption peaks (full curves) show an anticrossing behavior. The anticrossing of the polariton peaks is indicated in Fig. (5.2) by the dashed lines with black (upper polariton) and white (lower polariton) circles. When the cavity mode and the QW transition energy are in resonance, the energy difference between upper and lower polariton is minimal and equal to the Rabi-splitting energy, which is about  $\Omega_{Rabi} = 64$  meV in this calculation.

### 5.1.1 Experimental growth procedure of microcavity structures

The fabrication of the microcavity structure is divided into five steps. First the active layer of ZnSe/(Zn,Cd)Se QWs is grown by MBE and afterwards characterized by x-ray

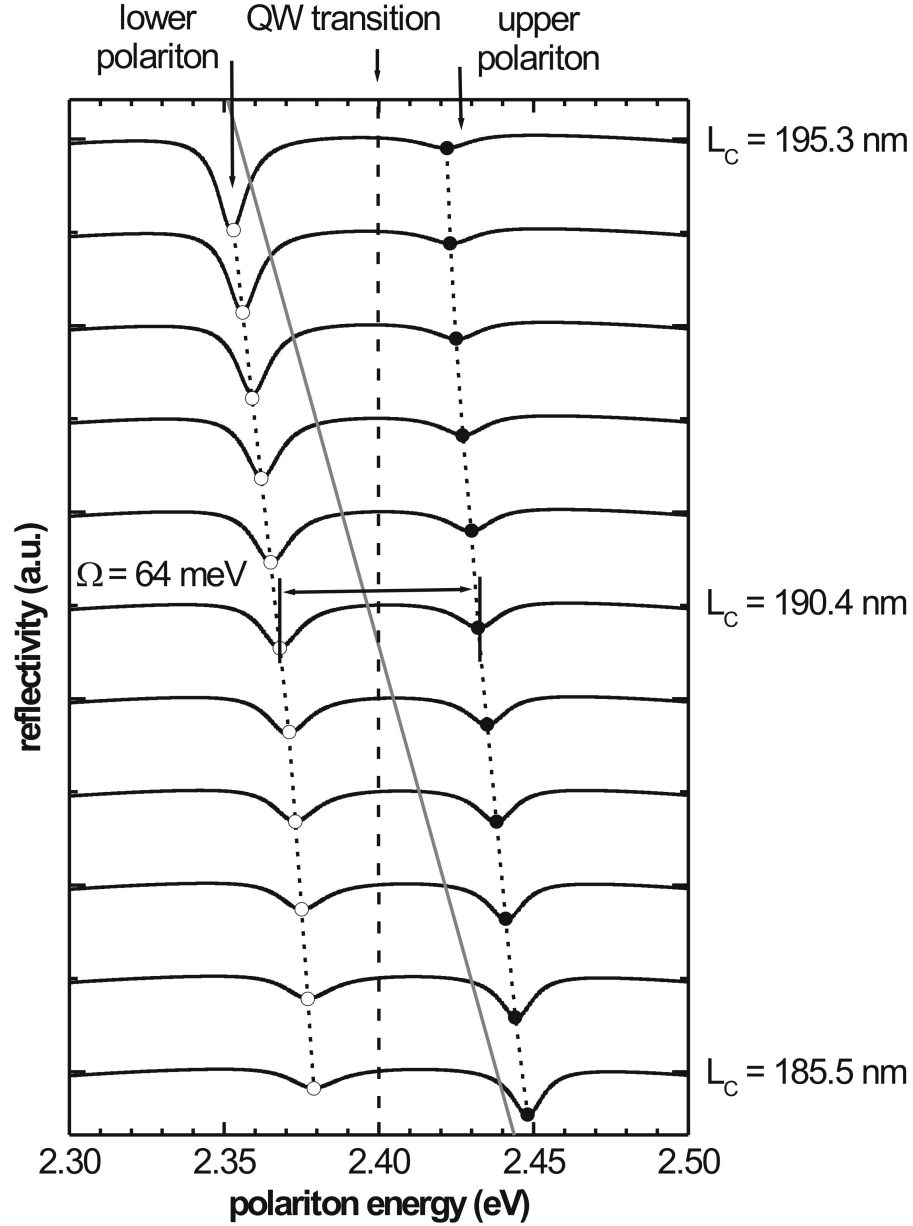


Figure 5.2: Reflectivity spectra (full curves) of the microcavity structure as a function of  $L_C$ . Due to the thickness gradient, the cavity mode shifts to higher energy (grey line), while the QW transition energy is constant (black dashed line). The strong coupling is manifested in the anticrossing behavior of the two absorption peaks (dotted lines with white and black circles). The minimum splitting energy between the lower and the upper polariton peak is about  $\Omega_{Rabi} = 64$  meV.

diffraction and PL, to obtain the important structural parameters.

After that the sample is transferred into a evaporation chamber to deposit the first Bragg-mirror, which is a stack of eight pairs of ZnSe/YF<sub>3</sub> or ZnS/YF<sub>3</sub>, respectively. In a third step the "flip-chip"-technology is used to fix the sample with the mirrored surface on glass substrate by using epoxy glue.

After this procedure, the most complicated preparation step, the selective wet etching of the GaAs substrate, is performed. An appropriate solution of 82 ml NaOH (1M) and 18 ml H<sub>2</sub>O<sub>2</sub> (35 %) is used. The typical etch rate in GaAs is about 100-150  $\mu\text{m h}^{-1}$ .

Experimental results have shown, that the epitaxial ZnSe layer might be exposed up to 10 min to the etching solution. During this time no significant reduction of the layer thickness but a slight increase of the surface roughness (about 8 nm after 10 min) is observed [Ar2003]. After the substrate removal process has been performed, the microcavity is completed by deposition of a six-fold stack of ZnSe/YF<sub>3</sub> or ZnS/YF<sub>3</sub> DBRs.

The critical point of the substrate removal process is the relaxation of the epitaxial ZnSe layer. This has to be considered, because the active layer is strained on the GaAs substrate. Fig. (5.3) depicts a microscope picture of a four-fold SL structure after the selective wet etching process. The GaAs (brown color) is completely removed in the center of the sample and the active layer (orange) is uncovered.

The spontaneous relaxation of the active layer leads to the formation of horizontal and vertical microcracks in the preferred (110) and (-110) crystallographic direction. Then the etch solution penetrates through this cracks into the interface between the active layer and the first Bragg-mirror. The green region in the center of Fig. (5.3) shows the Bragg-mirror surface. In this region the active layer was washed away by the etch solution.

The damage in the active layer is significantly reduced in case of partial or fully relaxed structures [Ar2003]. Nevertheless, in the previous chapter it has been shown that fully strained SL structures have significantly better optical and structural properties than the partial relaxed MQW structures. However, further optimization of the substrate removal process has to be performed.

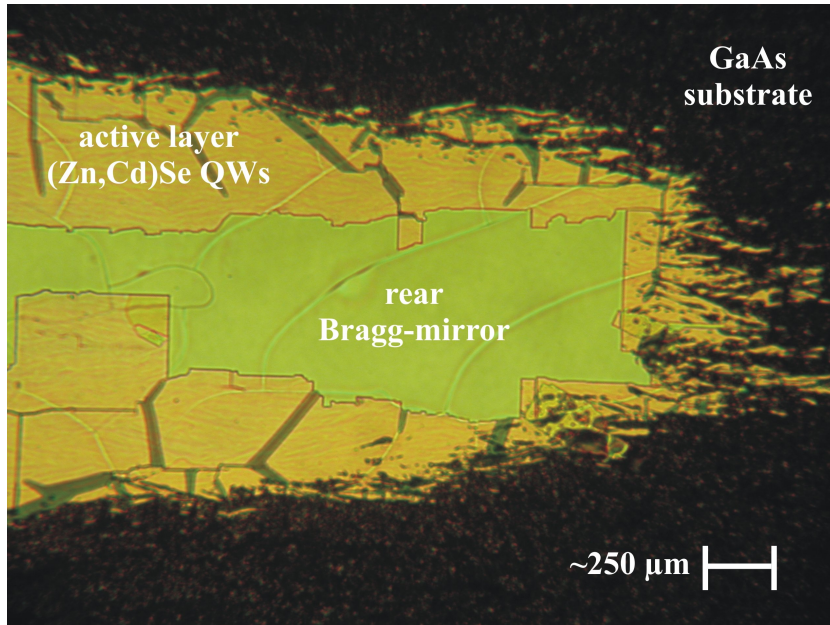


Figure 5.3: Microscope picture of a SL structure after selective wet etching. The GaAs substrate (brown) is removed in the center of the sample. The orange colored pieces near the border to the GaAs are parts of the active layer. The green region in the center of the picture shows the Bragg-mirror surface. The whole GaAs-free region is strewn with microcracks, which are the result of spontaneous relaxation of the active layer.

## 5.2 Investigation of a SL microcavity structure with ZnSe/YF<sub>3</sub> DBRs

Although the substrate removal process is critical in case of fully strained SL structures, the four-fold SL sample McS-851 has been successfully completed in a microcavity structure (sample PE-031) with an eight-fold stack of ZnSe/YF<sub>3</sub> DBRs on the rear side and a six-fold stack of ZnSe/YF<sub>3</sub> DBRs on the front side, respectively.

The structural properties of this sample are obtained from the x-ray measurements shown in Fig. (4.13). The nominal ZnSe barrier thickness is about 76 nm for each barrier, the thickness of the (Zn,Cd)Se QWs is about 3.9 nm and the QWs are separated by approximately 4.1 nm ZnSe spacers. From these data a resonator length of about 180 nm

is obtained.

The PL spectrum of this sample measured before mirror deposition and substrate removal, is illustrated in Fig. (4.18). A QW transition energy of 2.526 eV with a FWHM linewidth of about 23 meV is observed at room temperature. Using the structural parameters, which are obtained by x-ray diffraction, the transition energy can be calculated with the finite barrier model of biaxial strained QWs [Pa2000]. The theoretical value of 2.524 eV is in excellent agreement with the PL data and the x-ray measurements.

### 5.2.1 Measurement of the microcavity length gradient off-resonance

To gain information about the microresonator length gradient, the reflectivity of the microcavity is measured at room temperature on different positions on the sample. The reflectivity spot size is about 300  $\mu\text{m}$  and the spot position is moved in 250  $\mu\text{m}$  steps across the sample surface in direction of the resonator length gradient.

Three of these reflectivity spectra are illustrated in Fig. (5.4). The cavity mode is clearly resolved in each spectrum and has a FWHM value of about 48 meV. Furthermore a clear shift to lower energy with increasing sample thickness is observed.

The absorption peak energy of the cavity mode as a function of the position  $s$  on the sample up to 2000  $\mu\text{m}$  from the origin (black dots, left scale) is summarized in Fig. (5.5). From the linear approximation an energy shift of about  $\Delta E_C = 13 \text{ meV mm}^{-1}$  on the sample is obtained. Considering the refractive index of ZnSe, the resonator length is calculated from the absorption peak energies (grey dots, right scale). This results in a cavity length of  $L_C = 172.8 + 1.19 * 10^{-3} * s$ , which is in excellent agreement with the nominal cavity length of 180 nm measured by x-ray diffraction before the mirror deposition.

### 5.2.2 Reflectivity measurements in resonance condition

The position dependent cavity mode energy of the sample is obtained from the linear approximation  $E_C = 2.579 - 1.3 * 10^{-5} * s$  (eV). The transition energy of the (Zn,Cd)Se

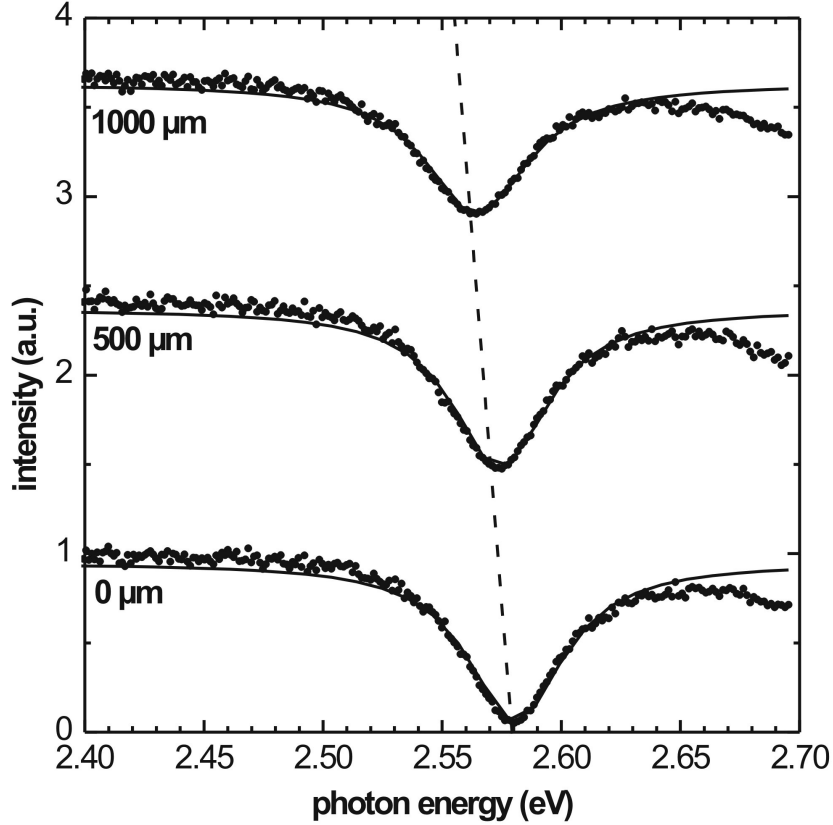


Figure 5.4: Reflectivity spectra of the SL microcavity PE-031 measured at various positions on the sample (0  $\mu\text{m}$ , 500  $\mu\text{m}$  and 1000  $\mu\text{m}$ ). A linear shift of the cavity mode to lower energy is observed (dashed line). The FWHM value of the cavity mode is about 48 meV.

QWs has been measured by PL at 2.526 eV. Therefore the resonance position between photonic and excitonic mode at room temperature is calculated of about 3500  $\mu\text{m}$  from the origin.

The spectra in Fig. (5.6) are measured near the calculated resonance position as a function of the position on the sample (dots). The spectra measured at 2250  $\mu\text{m}$ , 3100  $\mu\text{m}$  and 3200  $\mu\text{m}$  are each fitted by a Lorentzian function, where the spectra at 2500  $\mu\text{m}$ , 2750  $\mu\text{m}$  and 3000  $\mu\text{m}$  are each fitted with two Lorentzian peaks, respectively (full curves). The energetic peak positions, indicated by the arrows are obtained from the best fit of each measured spectrum.

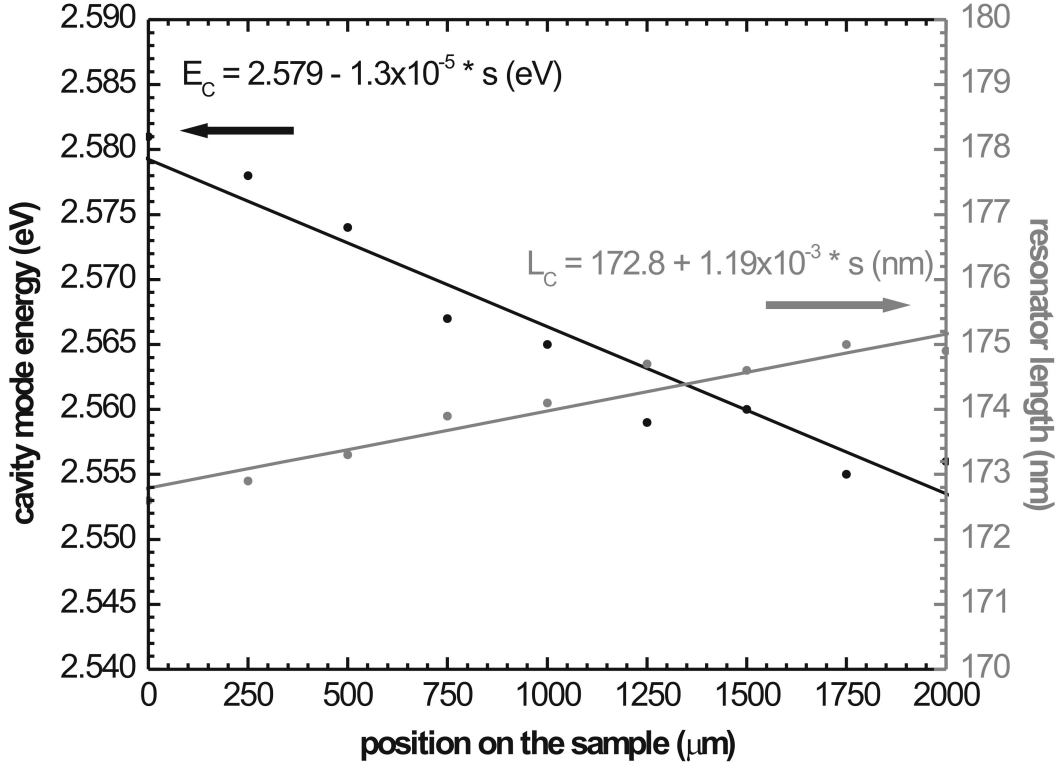


Figure 5.5: Absorption peak energy  $E_C$  of the cavity mode as a function of the position  $s$  on the sample PE-031 (black dots, left scale). From the linear approximation (black line, left scale) a cavity mode energy shift of about  $13 \text{ meV mm}^{-1}$  on the sample is obtained. The grey dots and the grey line, respectively, describe the resonator length gradient  $L_C$  (right scale).

In the spectrum measured at  $3000 \mu\text{m}$  two absorption peaks with an energy difference of about  $\Omega = 35 \text{ meV}$  and a FWHM value of  $15 \text{ meV}$  and  $47 \text{ meV}$  are clearly resolved (black and grey curve). The average linewidth (i.e. the splitting to linewidth ratio) of both absorption peaks is about  $32 \text{ meV}$ . The strong coupling condition in Sec. (2.1.1) denotes that the average linewidth of both polariton peaks should not exceed the splitting energy. This condition is barely fulfilled in the spectra in Fig. (5.6) and explains, that the polariton splitting is not resolved more pronounced.

In the spectra measured at  $2250 \mu\text{m}$ ,  $3100 \mu\text{m}$  and  $3200 \mu\text{m}$ , the splitting is not resolved any more, due to the fact that the cavity mode linewidth exceeds the splitting to linewidth ratio. In the spectra measured at  $2500 \mu\text{m}$  and  $2750 \mu\text{m}$  still a slight shoulder in the

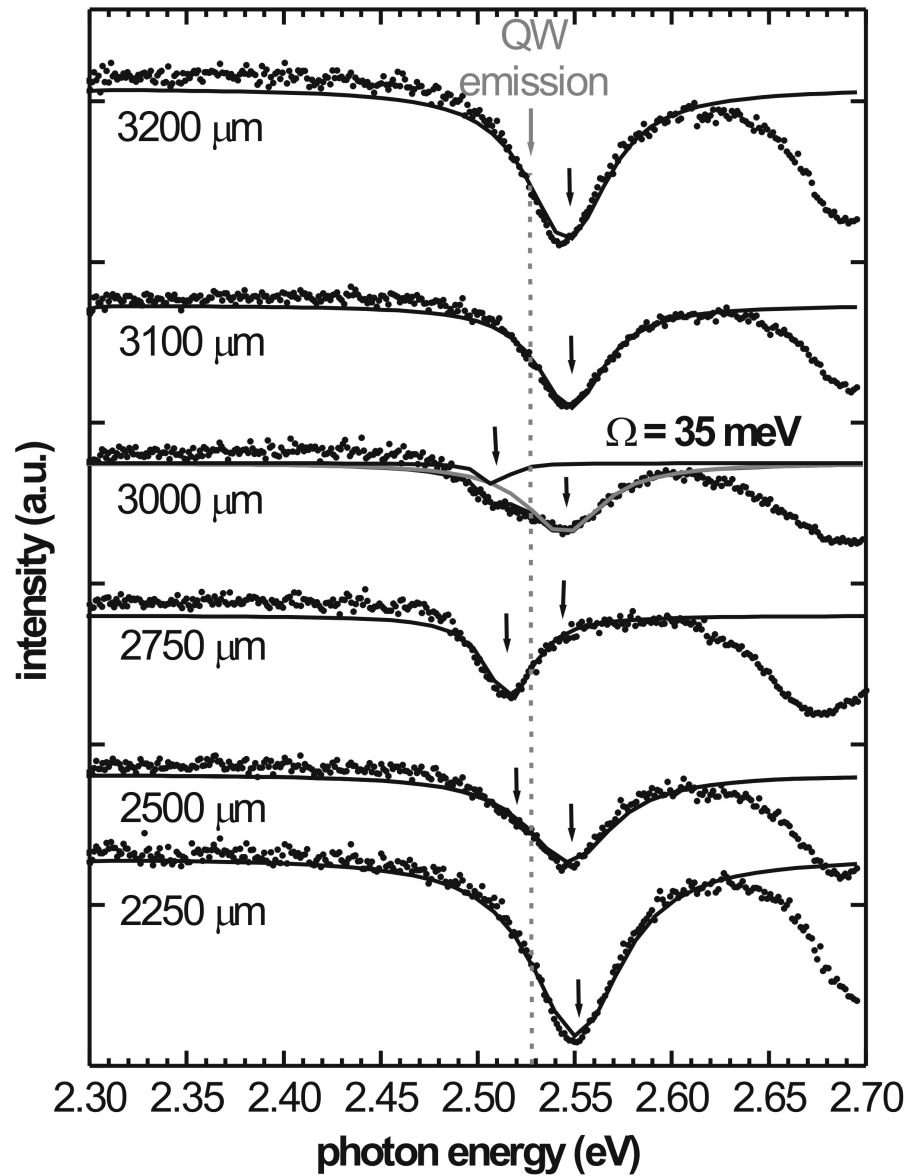


Figure 5.6: Room temperature reflectivity spectra of the SL microcavity PE-031 near the resonance position between photonic and excitonic mode. In the spectrum at 3000  $\mu\text{m}$  two absorption peaks with an energy difference of  $\Omega = 35$  meV and a FWHM value of 15 meV and 47 meV are resolved from a fit with two Lorentzian peaks (black and grey curve). In the spectra measured at 2500  $\mu\text{m}$  and 2750  $\mu\text{m}$  also a slight shoulder in the absorption peak is observed, while the other spectra show the cavity mode only. The fitted peak energies of each spectrum are indicated by the black arrows.

absorption peaks is observed, yielding that the coupling is at least stable in the range between  $2500 \mu\text{m}$  and  $3000 \mu\text{m}$ . However, there is a slight variation between the calculated and experimental resonance position (at  $3500 \mu\text{m}$  and  $3000 \mu\text{m}$ , respectively). This fact yields that the strain relaxation in the sample after the substrate removal process has a perceptible influence on QW emission energy.

The absorption peak energies of each spectrum in Fig. (5.6) is plotted as a function of the resonator detuning energy  $\hbar(\omega - \omega_0)$  (dots) in Fig. (5.7). The detuning energy (bottom scale) is calculated from the difference between QW transition energy and cavity mode energy, respectively. The full curves in Fig. (5.7) depict the theoretical polariton

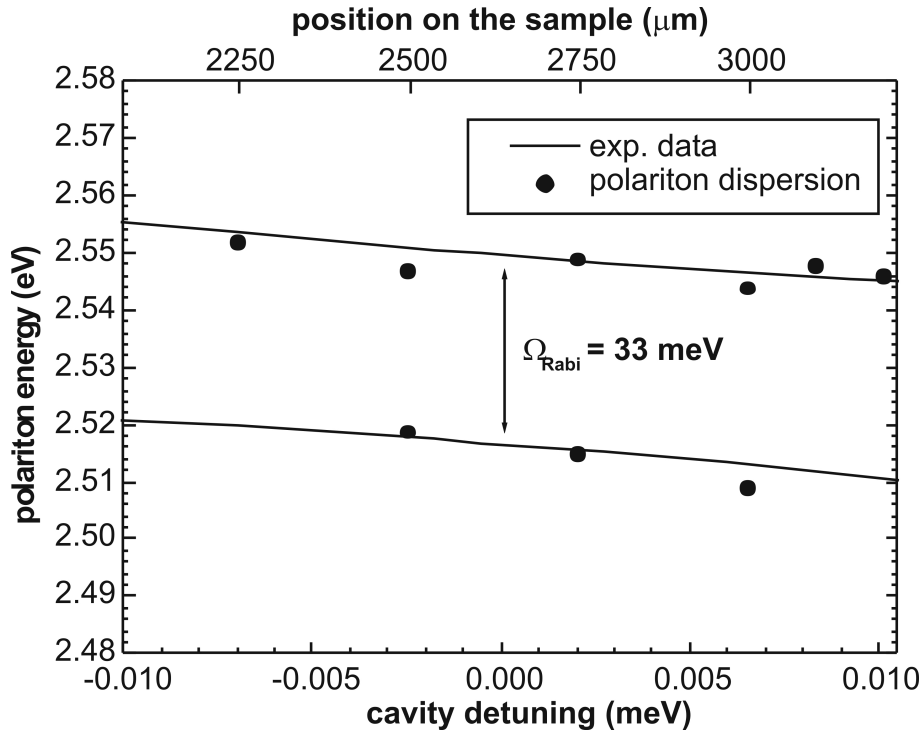


Figure 5.7: Absorption peak energy (dots) of each spectrum in Fig. (5.6) as a function of the resonator detuning energy  $\hbar(\omega - \omega_0)$  (bottom scale). The top scale denotes the position on the sample. The full curves depict the calculated polariton dispersion curves for the microcavity. However, a good agreement between experimental and theoretical data is achieved, yielding the typical anticrossing behavior of the polariton dispersion curves in the strong coupling regime. The calculated Rabi-splitting energy is about  $\Omega_{\text{Rabi}} = 33 \text{ meV}$  at zero detuning.

dispersion for the microcavity structure. For the calculation Eq.( 2.5) is used, where the photon dispersion  $E_C$  is given by the resonator length gradient as shown in Fig. (5.5). The exciton dispersion  $E_X$ , which is position independent, corresponds to the QW transition energy. The Rabi-splitting energy as well as the QW transition energy are used as fitting parameters, to achieve an agreement with the experimental data in Fig. (5.7).

From the calculation a Rabi-splitting energy of  $\Omega_{Rabi} = 33$  meV and a QW transition energy of  $E_X = 2.538$  eV is obtained. Both results are in good agreement with the experimental observations, yielding the typical anticrossing behavior of the polariton dispersion curves in Fig. (5.7). This calculation supposes the existence of the strong coupling in the SL microcavity PE-031 at room temperature.

### 5.3 Room temperature Rabi-splitting in a MQW microcavity with ZnS/YF<sub>3</sub> DBRs

In the previous section the exciton-photon coupling in a fully strained SL microcavity with four (Zn,Cd)Se QWs has been discussed. The relaxation process of the active layer after the GaAs substrate removal induces the formation of microcracks in the sample, which leads to surface destruction. This results in an increased FWHM value of the cavity mode and decreases the splitting to linewidth ratio.

Due to the partial strain relaxation of MQW structures, the damage of the active layer is significantly reduced although the optical and structural properties of MQW samples are not as good as in SL structures. The reduction of microcracks and surface roughness decreases the FWHM value of the photonic mode in the MQW structure and the Rabi-splitting condition is sufficiently fulfilled.

The cross-section drawing of the as-grown MQW microcavity PE-013 is illustrated in Fig. (5.8). The active layer contains four (Zn,Cd)Se QWs with a cadmium mole fraction of 0.31 and a QW thickness of 7 nm. The QWs are enclosed in ZnSe barriers of 68 nm and 72 nm, respectively. The nominal resonator length is about 197 nm. The structural

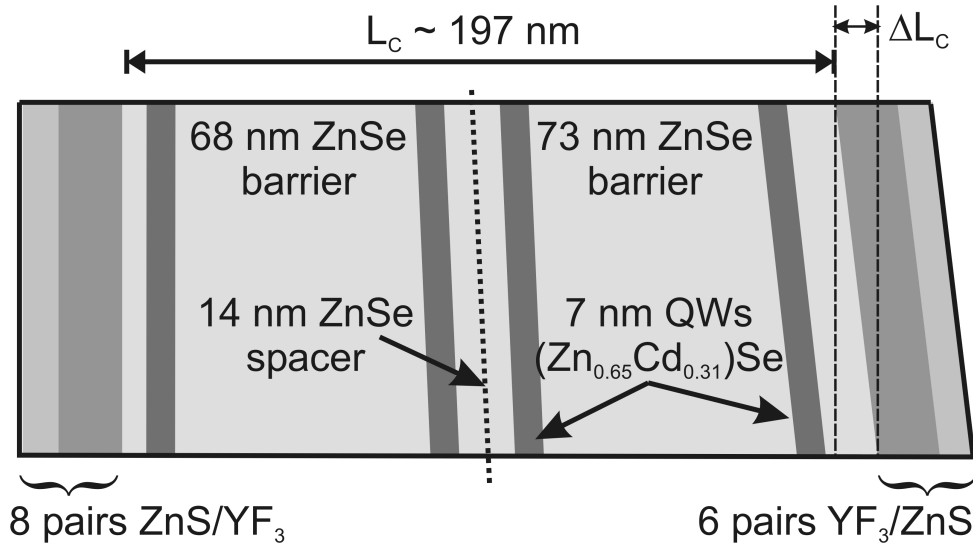


Figure 5.8: Cross-section drawing of the as-grown MQW microcavity PE-013 with six periods of ZnS/YF<sub>3</sub> DBRs on the front side and eight periods on the rear side, respectively. The (Zn,Cd)Se QWs are aligned in MQW configuration and enclosed in ZnSe barriers. The nominal resonator length is about  $L_C = 197$  nm plus the cavity length gradient  $\Delta L_C$ .

data are obtained from the  $\omega - 2\theta$ -scan in Fig. (4.5). The microcavity is completed by a six-fold stack of ZnS/YF<sub>3</sub> DBRs on the front side and an eight-fold stack of ZnS/YF<sub>3</sub> DBRs on the rear side.

For detailed information about the microcavity length gradient  $\Delta L_C$ , the reflectivity of the structure is measured off-resonance as a function of the position on the sample. Some of the spectra are summarized in Fig. (5.9) (dots). The cavity mode shifts to higher energy with increasing position on the sample and the dashed line reveals a nonlinear dependence. The cavity mode energy shift is sufficiently approximated by

$$E_C = 2.255 + 4 \times 10^{-6} * s + 8 \times 10^{-8} * s^2 \text{ (eV)}, \quad (5.1)$$

where  $E_C$  is the cavity mode energy in (eV) and  $s$  the position on the sample in ( $\mu\text{m}$ ). Each spectrum in Fig. (5.9) is fitted with a Lorentzian function, revealing cavity mode FWHM values between 10 meV and 16 meV, which is significantly smaller than it has

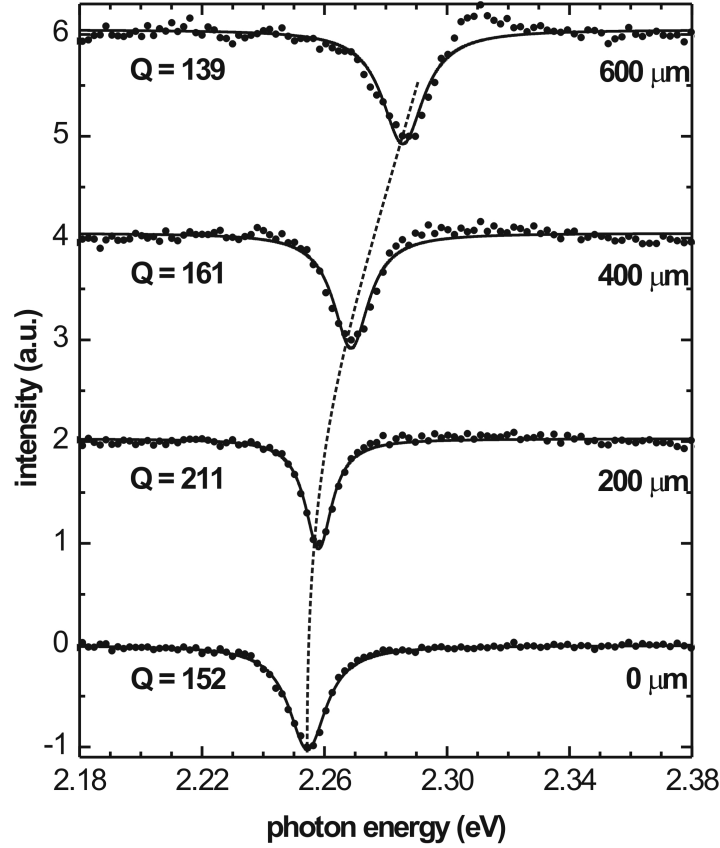


Figure 5.9: Room temperature reflectivity spectra of the MQW microcavity measured off-resonance on various positions on the sample (dots). The spectra denote a clear shift of the cavity mode  $E_C$  to higher energy with increasing sample position. This shift is indicated by the dashed line and shows a nonlinear behavior. Each spectrum is fitted with a Lorentzian function and the quality factor  $Q$  is calculated.

been obtained for the SL microcavity PE-031 (about 48 meV). The cavity quality factor is given by  $Q = E_C/\Delta E_C$ , where  $E_C$  is the energetic position of the photonic mode.

Fig. (5.10) shows the room temperature PL spectrum of the MQW microcavity structure PE-031 measured off-resonance. The grey curve depicts the Gauss fit of the spectrum, yielding a QW transition energy of 2.313 eV with a FWHM value of about 26 meV. This value is significantly smaller than that of the similar MQW-structure McS-1072

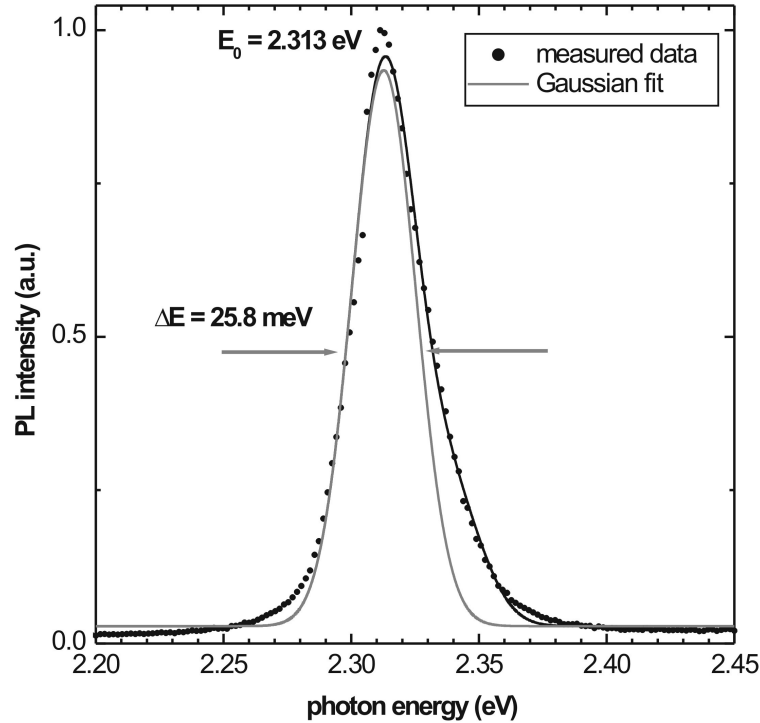


Figure 5.10: Room temperature PL spectrum of the MQW microcavity PE-013 measured off-resonance (dots). The spectrum is fitted with a Gaussian function (grey curve) and from that a QW transition energy of 2.313 eV with an FWHM of about 26 meV is obtained.

in Fig. (4.9), left side (about 33 meV). This observation reveals that the spontaneous emission rate of the active layer is enhanced due to the inclusion in the Bragg-mirrors.

### 5.3.1 Photoluminescence investigations of the MQW microcavity in resonance condition

Besides the position dependent reflectivity measurements, room temperature PL investigations have been performed at resonance between excitonic and photonic mode. In this case, the sample position and therefore the cavity mode energy is fixed, while the QW transition energy is tuned by varying the sample temperature.

Fig. (5.11) shows the luminescence spectra of the MQW microcavity PE-013 between

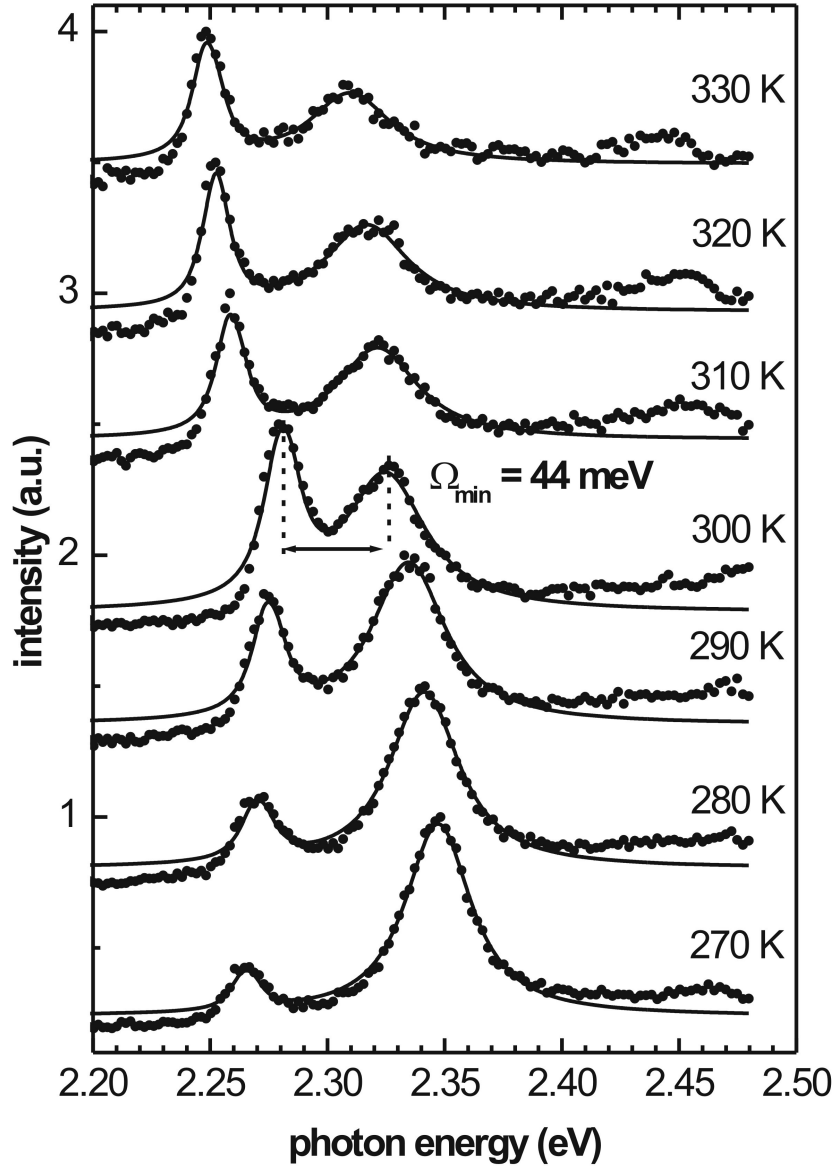


Figure 5.11: PL spectra of the microcavity PE-013 measured between 270 K and 330 K (dots). The curves represent Lorentzian fits. The increase of the temperature leads to a redshift of the QW emission, while the cavity mode energy is constant at  $E_C = 2.294$  eV. The experimental data show a clear anticrossing behavior and the minimum splitting  $\Omega_{\min} = 44$  meV is observed at 300 K.

270 K and 300 K (dots) and the full curves represent Lorentzian fit functions. The energy of the photonic mode is constant at  $E_C = 2.294$  eV. A QW transition energy redshift of about  $1 \text{ meV K}^{-1}$  with increasing temperature is estimated. This shift is confirmed by off-resonance PL measurements between 250 K and 270 K.

The experimental data in Fig. (5.11) show two well separated luminescence peaks in each spectrum. Furthermore a clear anticrossing behavior between both peaks is observed and denotes the strong coupling between photon and exciton in the MQW microcavity. The minimum splitting between the luminescence peaks of about  $\Omega_{min} = 44$  meV is measured at 300 K. From the FWHM values of both peaks, which are 15.5 meV and 39.7 meV, respectively, an average linewidth of 27.6 meV is obtained.

This results reveals that the conditions for the strong coupling (i.e. the splitting to linewidth ratio) are fulfilled. Furthermore in Fig. (5.11) a redistribution of the intensity from the upper to the lower polariton peak is observed with increasing temperature. This behavior is also a clear indication in the strong coupling regime.

Fig. (5.12) shows the peak energies of each spectrum in Fig. (5.11) plotted as a function of the temperature (dots). The full curves depict the best fit of the calculated temperature dependent polariton dispersion to the experimental data. For the calculation the cavity mode energy  $E_C = 2.294$  eV is derived from the cavity length gradient Eq. (5.1), while the temperature dependent QW transition energy is given by

$$E_X = 2.627 - 1.1 \times 10^{-3} \frac{\text{eV}}{\text{K}} * T, \quad (5.2)$$

where  $T$  is the sample temperature. The QW transition energy redshift of  $1.1 \text{ meV K}^{-1}$ , which has been assumed in Eq. (5.2) is in good agreement with the experimental data measured between 250 K and 270 K. The Rabi-splitting energy  $\Omega_{Rabi} = 52$  meV is obtained from the fit of the experimental data.

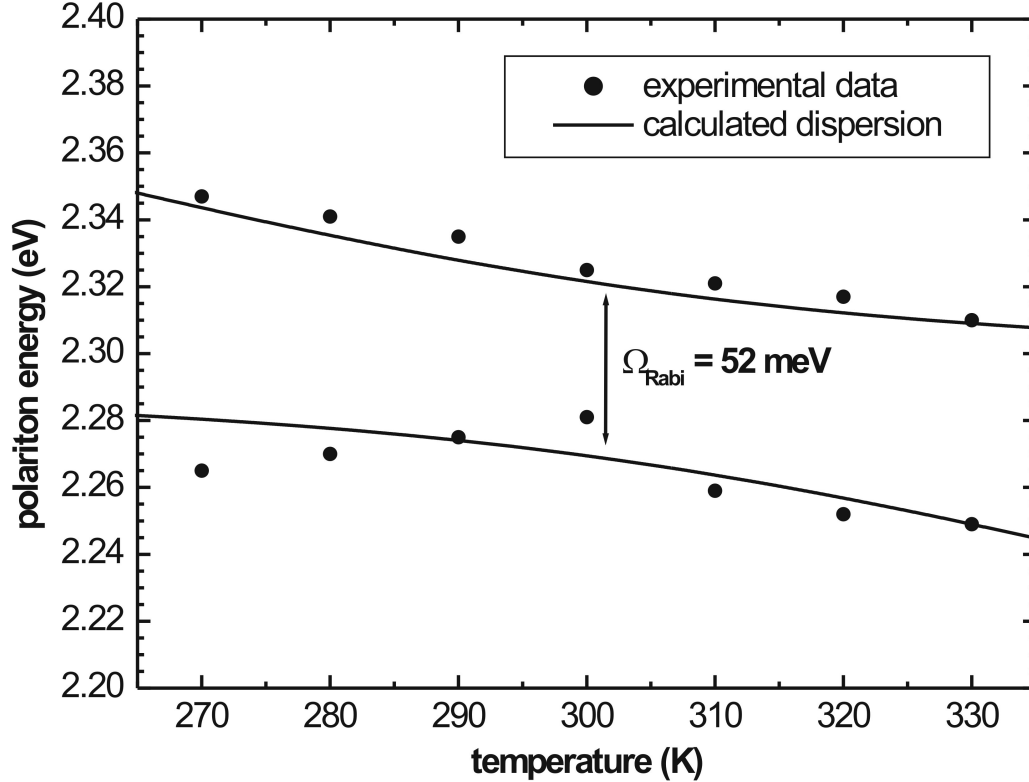


Figure 5.12: Temperature dependent polariton dispersion of the MQW microcavity PE-013. The luminescence peak energies, which were fitted with Lorentzian functions in Fig. (5.11), are plotted as a function of the temperature (dots). The full curves correspond to the calculated polariton dispersion. From this calculation a Rabi-splitting energy of  $\Omega_{Rabi} = 52$  meV is determined.

### 5.3.2 Reflectivity measurements of the MQW-microcavity in resonance condition

The information about the microcavity length gradient in Eq. (5.1) and the QW transition energy of 2.313 eV (see also Fig. (5.10)) are used to estimate the resonance position between the photonic and excitonic mode at room temperature. It is found to be about 830  $\mu\text{m}$  from the origin. Near the resonance position the reflectivity of the microcavity is measured as a function of the position on the sample. The measurements are performed with a 100  $\mu\text{m}$  spot focus on the sample.

The spectra measured at 200  $\mu\text{m}$ , 500  $\mu\text{m}$ , 700  $\mu\text{m}$  and 800  $\mu\text{m}$  from the origin (A, B, C

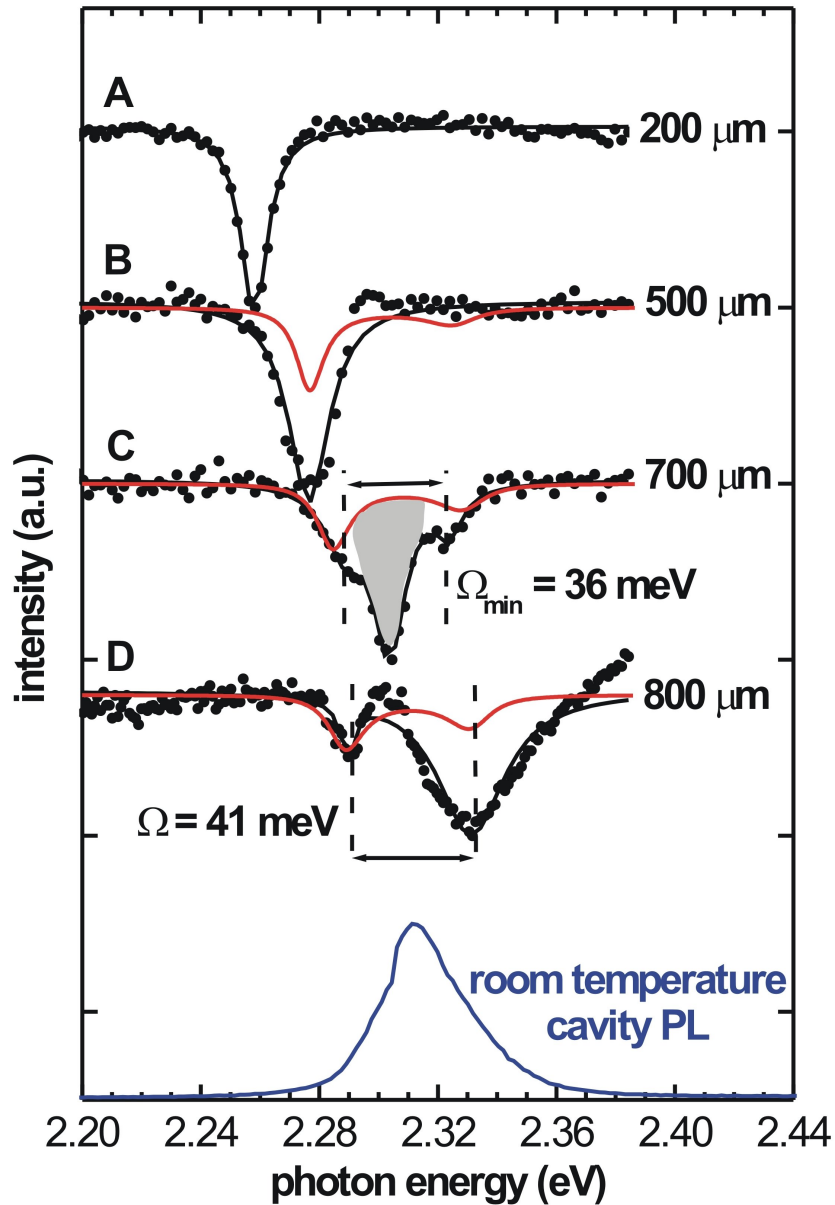


Figure 5.13: Overview of the room temperature reflectivity spectra (dots) of sample PE-013 measured in the range between  $200 \mu\text{m}$  and  $800 \mu\text{m}$  (A, B, C and D). Spectrum A and B show the cavity mode only, while in C and D a splitting into several absorption peaks is observed. The red full curves depict the polariton peaks calculated with the Transfer-Matrix model. The spectra B, C and D are in good agreement with the calculated curves and denote an anticrossing behavior of the polariton modes. From Lorentzian fits of the experimental data in spectrum C and D with three and two peaks, a splitting of  $36 \text{ meV}$  and  $41 \text{ meV}$  is extracted. The blue curve depicts the cavity photoluminescence. However, in the grey region in spectrum C additional absorption, which might be related to the QWs, is detected.

and D, respectively) are depicted in Fig. (5.13) (dots). Spectrum A and B show the cavity mode only, which is shifted to a higher energy with increasing position on the sample. Near the resonance position at 700  $\mu\text{m}$  (spectrum C) a splitting into three absorption peaks is observed. At 800  $\mu\text{m}$  two clearly separated peaks are resolved. The minimum splitting between the polariton peaks is about 41 meV.

The red full curves in spectrum B, C and D depict the polariton absorption peaks calculated with the Transfer-Matrix model. For this calculation the structural parameters of the MQW microcavity shown as well as the resonator length gradient Eq. (5.1) as the QW transition energy  $E_X = 2.313$  eV (blue curve), are used. A good agreement between the calculated polariton curves and the experimental spectra B, C and D is obtained. This result yields that two of the absorption peaks in spectrum C are related to the polariton splitting. From a Lorentzian fit of the experimental data with three peaks, a minimum Rabi-splitting energy  $\Omega_{min} = 36$  meV between the polariton absorption peaks at 2.288 eV and 2.324 eV, respectively, is extracted.

The third peak in spectrum C (grey region) as well as the enhanced FWHM value of the higher energy peak in spectrum D might be explained by QW absorption, which results from structural defects such as microcracks or holes in the front side DBR. In this case the polariton splitting is superimposed by the QW absorption in the range between 2.29 eV and 2.32 eV, which is in good agreement with the cavity PL spectrum (blue curve).

The average linewidth of the absorption peaks in spectrum C and D is about 13 meV and 17 meV, respectively. This observation is consistent with the calculated average linewidth  $\Delta E_{pol} = \frac{1}{2}(\Delta E_C + \Delta E_X) = 18$  meV and also significantly smaller than the Rabi-splitting energy  $\Omega_{min} = 36$  meV. Therefore the conditions of the strong coupling in the MQW microcavity are fulfilled.

The reflectivity spectra in Fig. (5.13) were fitted with Lorentzian functions and the absorption peak energies are plotted as a function of the microcavity detuning energy in Fig. (5.14) (black dots). The detuning energy is due the energy difference between the uncoupled excitonic and photonic mode. The resonance condition in the microcavity is

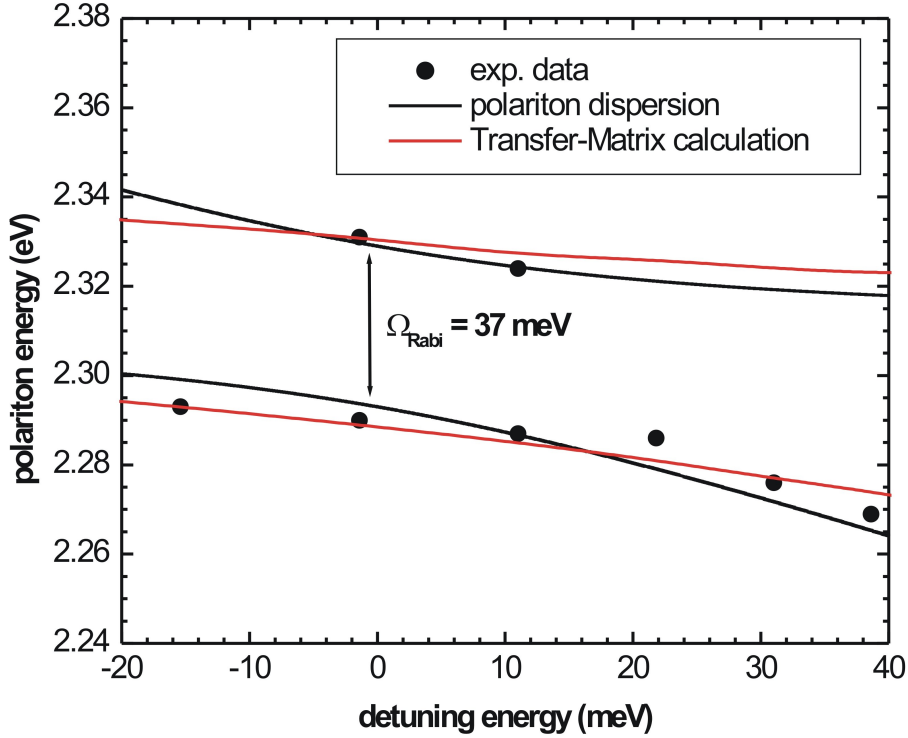


Figure 5.14: Absorption peak energies of the reflectivity spectra in Fig. (5.13) as a function of the microcavity detuning energy (black dots). The red curves denote the polariton dispersion curves calculated with the Transfer-Matrix model (i.e. the red curves in Fig. (5.13)). The anticrossing of the upper and lower polariton branch is well resolved. The black full curves are the calculated polariton dispersion curves using Eq. (2.5). From this calculation a Rabi-splitting energy of  $\Omega_{Rabi} = 37$  meV is obtained.

achieved at zero detuning energy. The red curves denote the polariton dispersion curves calculated with the Transfer-Matrix model (see also the red curves in Fig. (5.14)). A good agreement of the Transfer-Matrix calculation and the experimental data is obtained.

The black full curves in Fig. (5.14) depict the polariton dispersion curves calculated with Eq. (2.5), where  $E_C$  is given by Eq. (5.1) and the QW transition energy  $E_X$  as well as the Rabi-splitting energy  $\Omega_{Rabi}$  are used as fitting parameters. The best agreement with the experimental data in Fig. (5.14) as well as the Transfer-Matrix calculation is achieved for  $E_X = 2.308$  eV and  $\Omega_{Rabi} = 37$  meV. From the PL spectrum in Fig. (5.10) a QW transition energy of  $E_X = 2.313$  eV is obtained. Finally the good agreement between

the reflectivity measurements in Fig. (5.14) and the calculated polariton dispersion curves confirms the strong coupling in the MQW microcavity PE-013.

Although the Rabi-splitting energy is larger in the PL measurements of the MQW microcavity (about 44 meV), calculated and experimental data of both, PL and reflectivity investigations, are in good agreement with the expected polariton properties.

### 5.3.3 Calculation of the QW oscillator strength per unit area

In Sec. (2.1) it has been shown that the Rabi-splitting energy  $\Omega_{Rabi}$  depends on the number of QWs, the effective length of the microcavity  $L_{eff.} = L_C + L_{DBRs}$  and the oscillator strength per unit area  $\frac{f}{S}$ . Therefore the oscillator strength per unit area can be calculated from the experimental Rabi-splitting values  $\Omega_{min}$  for both, the SL microcavity and the MQW microcavity, respectively. The penetration depth  $L_{DBRs}$  of the photonic mode into the Bragg-mirrors is obtained from

$$L_{DBRs} = \frac{\lambda}{2n_C} * \frac{n_L n_H}{n_H - n_L} \quad (5.3)$$

where  $n_C$  is the refractive index of the active layer and  $n_H$  and  $n_L$  are the higher and lower refractive index of the Bragg-mirrors, respectively [Sk1998].

sample	x(Cd)	$\Omega_{Rabi}$ (meV)	$L_{eff.}$ (nm)	$E_{resonance}$ (eV)	$\frac{f}{S}$
SL, reflection	0.20	35	176	2.541	0.037±0.005
MQW, reflection	0.35	36	200	2.308	0.044±0.005
MQW, photoluminescence	0.35	44	201	2.298	0.067±0.005

Table 5.1: Calculation of the QW exciton oscillator strength per unit area from the Rabi-splitting energies measured on the SL and MQW microcavity, respectively. The SL microcavity has a significantly smaller oscillator strength of 0.037±0.005 compared to the average oscillator strength of the MQW microcavity of about 0.056±0.005.

The oscillator strength per unit area for both, the SL and MQW microcavity, are summarized in Tab. (5.1). The average oscillator strength from the reflectivity and PL inves-

tigations of the MQW microcavity is about 0.056, which is significantly larger than the oscillator strength in the SL microcavity (about 0.037).

This observation is consistent with the difference of the cadmium mole fraction in the (Zn,Cd)Se QWs of both structures. With decreasing cadmium mole fraction, the exciton confinement in the QWs is reduced, yielding a delocalization of the exciton wavefunction. This results in a decrease of the electron- and hole-wavefunction overlap integral, which is related to the oscillator strength. In [Di1993] an oscillator strength per unit area of about 0.02 is obtained for a  $\text{Zn}_{0.76}\text{Cd}_{0.24}\text{Se}$  QW structure enclosed between relaxed ZnSe barriers. This value is slightly smaller than that obtained with the SL microcavity. This maybe due to the fact that the ZnSe barriers enclosing the (Zn,Cd)Se QWs in the SL structure are still partial strained, yielding an additionally confinement of the QWs and therefore an increased oscillator strength.

## 6 Conclusions

Since Weisbuch et. al. 1992 has demonstrated the existence of a new quasi-particle, the polariton, which results from the strong coupling between excitons and photons in semiconductor microcavities, this phenomenon has been studied with expanding interest in common high quality III-V semiconductors such as GaAs, AlAs and their alloys. However, it has been found out that the polariton properties strongly depend on the exciton binding energy and the oscillator strength in the semiconductor material, yielding that GaAs and AlAs are unsuitable for the development of room temperature polariton applications and -devices.

The focus of this thesis has been the development and investigation of a semiconductor microcavity based on the II-VI materials ZnSe and CdSe and enclosed in dielectric DBRs of ZnS/YF<sub>3</sub> or ZnSe/YF<sub>3</sub>, respectively.

First of all dielectric Bragg-mirrors of ZnS/YF<sub>3</sub> were grown on standard GaAs substrate by thermal evaporation. From optical characterization, high reflectivity coefficients between 0.92 and 0.95 are obtained in the visible spectral range with six up to ten Bragg-mirror pairs. Simulations of the spectral reflectivity with the Transfer-Matrix model indicate that sulphur interdiffusion between the mirror interfaces decreases the refractive index difference between ZnS and YF<sub>3</sub> and reduces shape and reflectivity of the Bragg-mirror stop-band. Furthermore structural investigations by AFM yield a significant increase of the surface roughness, which is proportional to the number of periods and limits the maximal reflectivity.

In dielectric Bragg-mirrors of ZnSe/YF<sub>3</sub>, the sulphur was exchanged by selenium. There-

fore interdiffusion effects are significantly reduced and the larger refractive index difference between ZnSe and YF<sub>3</sub> induces a better photonic confinement in the DBRs. From the reflectivity investigations of ZnSe/YF<sub>3</sub> Bragg-mirrors, high reflectivity coefficients of 0.993 up to 0.999 are achieved with five up to ten mirror periods. However, the increased reflectivity compared to that of ZnS/YF<sub>3</sub> DBRs is only obtained for a wavelength larger than 470 nm, since strong bandgap absorption in ZnSe occurs in the blue and near UV light region.

In the second part of this work, MBE grown ZnSe/(Zn,Cd)Se MQWs with up to four, and SL structures with up to six (Zn,Cd)Se QWs as the active layer in II-VI microcavities were investigated. The main issue was the in-situ and ex-situ control of the structural properties as well as the implementation of a cavity length gradient in the ZnSe barrier layers, which allows the resonance tuning in the microcavity.

With high-resolution x-ray diffraction it is shown that MQW structures are partial relaxed, due to the large strain field near the first (Zn,Cd)Se QW closely to the interface between GaAs and ZnSe. This fact leads to an inhomogeneous strain distribution along the growth direction of the MQW structure. Additionally to this, a degeneration of the crystallographic quality is measured with x-ray rocking curves. Due to the inhomogeneous strain distribution, a large QW transition linewidth up to 33 meV at room temperature and 27 meV at 4 K is obtained from PL investigations.

In contrast to this, the SL structures with four (Zn,Cd)Se QWs have significantly better crystallographic quality and are also fully strained on the GaAs substrate. Therefore a homogenous strain distribution along the QWs is achieved, yielding a smaller QW transition linewidth of 22 meV at room temperature and of 20 meV at 4.3 K. Furthermore up to six QWs are successfully included into SL structures without significant degradation of the structural and optical properties of the active layer.

The main issue in the last part of this work was the combination of the ZnSe/(Zn,Cd)Se quantum structures with the dielectric Bragg-mirrors to a complete microcavity. Therefore a SL microcavity with ZnSe/YF<sub>3</sub> DBRs as well as a MQW microcavity with ZnS/YF<sub>3</sub>

---

mirrors were successfully performed into complete microcavities.

The interaction of the photonic and excitonic mode was characterized in both structures by room temperature reflectivity measurements at various positions on the sample. Therefore the photonic mode was tuned into resonance with the excitonic mode via the microcavity length gradient. In both structures the anticrossing dispersion of the two polariton states was measured. A minimum Rabi-splitting energy of 35 meV and 36 meV is obtained with the SL and MQW microcavity, respectively. Calculations of the polariton dispersion are in good agreement with the experimental data of both structures. This fact yields that the strong coupling regime is successfully demonstrated at room temperature with the SL as well as the MQW microcavity.

Additionally to this temperature dependent photoluminescence measurements were performed on the MQW microcavity. Both polariton luminescence peaks were resolved clearly. A minimum Rabi-splitting of 44 meV is measured in the resonance condition at 300 K and the typical anticrossing behavior is observed. These results are in good agreement with the experimental results of the position dependent reflectivity measurements.

Furthermore the QW oscillator strength per unit area was calculated from the Rabi-splitting energy. For the SL microcavity with four  $\text{Zn}_{0.8}\text{Cd}_{0.2}\text{Se}$  QWs a value of  $\frac{f}{S} = 0.037$  is obtained. In case of the MQW microcavity with four  $\text{Zn}_{0.65}\text{Cd}_{0.35}\text{Se}$  QWs the oscillator strength per unit area is about  $\frac{f}{S} = 0.056$ , averaged from the PL and reflectivity measurements. The comparison between both structures yields that the oscillator strength increases with an increased cadmium mole fraction in the (Zn,Cd)Se QWs.



# List of Figures

2.1	Interaction of excitons and photons in a semiconductor microcavity. . . . .	16
2.2	Calculation of the polariton dispersion of a microcavity . . . . .	20
2.3	Reflection and transmission of an electromagnetic wave on a plane layer surface. . . . .	21
2.4	Complex refractive index dispersion relations of ZnS and ZnSe. . . . .	23
2.5	Alignment of the evaporation cells in our MBE chamber to implement growth gradient in the active layer. . . . .	26
2.6	Principle of temperature detuning of a microcavity. . . . .	27
3.1	Reflectivity of an eight-fold stack of ZnS/YF <sub>3</sub> DBRs. . . . .	30
3.2	Reflectivity of a ten-fold stack of ZnS/YF <sub>3</sub> DBRs. . . . .	31
3.3	Reflectivity of a five-fold stack of ZnS/YF <sub>3</sub> DBRs. . . . .	33
3.4	AFM picture of a 20 $\mu\text{m} \times 20 \mu\text{m}$ scan of the ZnS surface of a six-fold stack of ZnS/YF <sub>3</sub> DBRs. . . . .	34
3.5	RMS surface roughness of several ZnS/YF <sub>3</sub> DBRs. . . . .	35
3.6	Maximum reflectivity of several ZnS/YF <sub>3</sub> DBRs as a function of the number of periods. . . . .	36
3.7	Reflectivity spectrum of a ten-fold stack of ZnSe/YF <sub>3</sub> DBRs. . . . .	38
3.8	Reflectivity spectrum of a five-fold stack of ZnSe/YF <sub>3</sub> DBRs. . . . .	39
3.9	AFM picture of a 20 $\mu\text{m} \times 20 \mu\text{m}$ scan of the ZnSe surface of a ten-fold stack of ZnSe/YF <sub>3</sub> DBRs. . . . .	41
3.10	Reflectivity and surface roughness of different ZnSe/YF <sub>3</sub> DBRs. . . . .	42

4.1	Intensity oscillations of the specular spot during deposition of ZnSe on GaAs surface. . . . .	47
4.2	Intensity oscillations of the specular spot during deposition of a (Zn,Cd)Se QW. . . . .	48
4.3	Cross-section drawing of MQW structures with up to four (Zn,Cd)Se QWs.	50
4.4	Reciprocal space map around the GaAs-(224) reflex of the MQW structure.	51
4.5	Symmetric (004)-reflex $\omega - 2\theta$ -scan of a MQW structure. . . . .	52
4.6	Symmetric $\omega$ -scan of the (004)-reflex of ZnSe in MQW structure McS-1072.	54
4.7	Symmetric $\omega - 2\theta$ -scan of a double QW structure and x-ray simulation spectrum. . . . .	55
4.8	Symmetric $\omega$ -scan of the ZnSe-(004)-reflex of the double QW structure McS-775. . . . .	56
4.9	PL spectra of a MQW structure at room temperature and 4.3 K. . . . .	57
4.10	PL spectra of a double QW structure at room temperature and 4.3 K. . . . .	59
4.11	Cross-section drawing of SL structures with four and six (Zn,Cd)Se QWs. .	60
4.12	Reciprocal space map around the GaAs-(224)-reflex of the SL-QW structure McS-851. . . . .	61
4.13	Symmetric (004)-reflex $\omega - 2\theta$ -scan of a SL structure (dots) with four QWs.	62
4.14	ZnSe-(004)-reflex $\omega$ -scan of the four-fold SL structure McS-851. . . . .	64
4.15	ZnSe-(004)-reflex $\omega - 2\theta$ -scan of a six-fold SL structure. . . . .	65
4.16	ZnSe-(004)-reflex $\omega$ -scan spectrum of the six-fold SL structure McS-1014. .	66
4.17	Cross section TEM-picture of a six-fold SL structure. . . . .	67
4.18	PL spectra (dots) of the four-fold SL structure McS-851 at room temperature (left side) and 4.3 K. . . . .	69
4.19	PL spectra (dots) of the six-fold SL structure McS-1014 at room temperature (left side) and 4.3 K. . . . .	70
5.1	Cross-section drawing of a typical ZnSe/(Zn,Cd)Se SL structure with four QWs. . . . .	72

5.2	Reflectivity spectra of the microcavity structure as a function of $L_C$ . . . . .	73
5.3	Microscope picture of a SL structure after selective wet etching. . . . .	75
5.4	Position dependent reflectivity spectra of the SL microcavity. . . . .	77
5.5	Absorption peak energy $E_C$ of the cavity mode as a function of the position $s$ on the sample. . . . .	78
5.6	Room temperature reflectivity spectra of the SL microcavity near the resonance position. . . . .	79
5.7	Absorption peak energy of each spectrum in Fig. (5.6) as a function of the resonator detuning energy. . . . .	80
5.8	Cross-section drawing of the as-grown MQW microcavity PE-013. . . . .	82
5.9	Room temperature reflectivity spectra of the MQW microcavity measured off-resonance. . . . .	83
5.10	Room temperature PL spectrum of the MQW microcavity measured off-resonance. . . . .	84
5.11	PL spectra of the microcavity PE-013 between 270 K and 330 K. . . . .	85
5.12	Temperature dependent polariton dispersion of the MQW microcavity PE-013. . . . .	87
5.13	Overview of the room temperature reflectivity spectra of sample PE-013 near the resonance. . . . .	88
5.14	Absorption peak energies of the reflectivity spectra of PE-013 as a function of the microcavity detuning energy. . . . .	90



# List of Tables

2.1	Parameters for the calculation of the complex refractive index dispersions of ZnSe, ZnS and GaAs . . . . .	24
3.1	Experimental (left side) and theoretical (right side) parameters of different ZnS/YF <sub>3</sub> DBRs. . . . .	32
3.2	Experimental and theoretical parameters of different ZnS/YF <sub>3</sub> DBRs. . . . .	40
5.1	Calculation of the QW exciton oscillator strength per unit area from the Rabi-splitting energies. . . . .	91



# Bibliography

- [Af1974] M.A. Afromowitz,  
Solid State Comm. **15**, 1974, p. 59.
- [Al1975] L. Allen and J.H. Eberly,  
*"Optical resonance and two-level atoms"*,  
Wiley, New York, 1975.
- [An2000] R. André, F. Boef, R. Romestain, Le Si Dang, E. Péronne, J.F. Lampin,  
D. Hulin and A. Alexandrou  
J. Chrystal Growth 214/215, 2000, p. 1002.
- [Ar2003] C. Arens,  
*"Herstellung und Charakterisierung von Quantenstrukturen in Mikroavitäten"*,  
Diplomarbeit, Fakultät für Naturwissenschaften,  
Universität Paderborn, 2003.
- [Ba1995] V. Bardinal, R. Legros and C. Fontaine,  
Appl. Phys. Lett. **67**, 1995, p. 3390.
- [Ba2002] J.J. Baumberg,  
Physics World, March 2002.
- [Ba2003] M. Bartels,  
*"Self-assembled epitaxial growth of CdSe Quantum Dot Structures"*

Dissertation, Fakultät für Naturwissenschaften,  
Universität Paderborn, submitted 2003.

- [Be1994] P.R. Berman,  
"Cavity quantum electrodynamics",  
Academic, Boston, 1994.
- [Bl1998] J. Bloch, T. Freixanet, J.Y. Marzin, V. Thierry-Mieg and R. Planel,  
Appl. Phys. Lett. **73** Nr. 12, 1998, p. 1694.
- [Ca1989] H.J. Carmichael, R.J. Brecha, M.G. Raizen, H.J. Kimble and P.R. Rice,  
Phys. Rev. A **40**, 1989, p. 5516.
- [Ci2002] M. Saba, C. Ciuti, J. Bloch, V. Thierry-Mieg, R. André, Le Si Dang, S. Kundermann, A. Mura, G. Bongiovanni, J.L. Staehli and B. Deveaud,  
Nature 414, 2002, p. 731.
- [Di1993] J. Ding, M. Hagerott, T. Ishihara, H. Jeon and A.V. Nurmikko,  
Phys. Rev. B **47**, Nr. 16, 1993, p. 10528.
- [Di2001] J.H. Dickerson, E.E. Mendez, A.A. Allerman, S. Manotas, F. Agulló-Rueda and  
C. Pecharromán  
Phys. Rev. B, /bf 64, 2001, p. 155302.
- [Ea1995] D.B. Eason, Z. Yu, W.C. Hughes, W.H. Roland, C. Boney, J.W. Cook Jr. and  
J.F. Schetzina,  
G. Cantwell and W.C. Harsch,  
Appl. Phys. Lett. **66** Nr. 2, 1995, p. 115.
- [Ge1998] J.M. Gérard, B. Sermage, B. Legrand, E. Costard and V. Thierry-Mieg,  
Phys. Rev. Lett. **81**, 1998, p 1110.
- [Gu1982] H.E. Gumlich, D. Theis and D. Tschierse,  
"Physics of II-VI and I-VII compounds, semimagnetic semiconductors",

edited by O. Madelung, Landolt Börnstein,  
New Series, Group III, Vol. 17b, Springer-Verlag Berlin, 1982.

- [He1979] E. Hecht and A. Zajac,  
*"Optics"*,  
Addison-Wesley Publishing Company, 1979.
- [Ho1958] J. J. Hopfield,  
Phys. Rev. **112** 1958, p. 1555.
- [Je1995] H. Jeon, V. Kozlov, P. Kelkar and A.V.Nurmikko, C.-C. Chu, D.C. Grillo,  
J. Han, G.C.Hua and R.L.Gunshor  
Appl. Phys. Lett. **67** Nr. 12, 1995, p. 1668.
- [Ke1995] P. Kelkar, V. Kozlov, H. Jeon and A.V. Nurmikko, C.-C. Chu, D.C. Grillo,  
J. Han, C.G. Hua and R.L. Gunshor  
Phys. Rev. B **52** Nr. 8, 1995, p. R5491.
- [Kh1999] G. Khitrova and H.M. Gibbs, F. Jahnke, M. Kira and S.W. Koch,  
Rev. Mod. Phys. **71**, 1999, p 1591.
- [Kh2003] A. Kharchenko,  
*"A new x-ray diffractometer for the online monitoring of epitaxial processes"*,  
Dissertation, Fakultät für Naturwissenschaften,  
Universität Paderborn, 2003.
- [No1999] T.B. Norris,  
*"Excitons in strongly coupled microcavities"*,  
ed. by A. Miller and D. Finlayson,  
Institute of Physics, 1999, p.121.
- [Pa2000] A. Pawlis,

*"Epitaktisches Wachstum und Charakterisierung von Mikrokavitäten"*,  
Diplomarbeit, Universität Paderborn, 2000.

- [Pa2001] A. Pawlis, A. Kharchenko, O. Husberg, D. Schikora and K. Lischka,  
phys. stat. sol. (a) **188**, 2001, p. 983.
- [Sa1974] M. Sargent, M.O. Scully and W.E. Lamb,  
*"Laser Physics"*,  
Addison Wesley, Reading, 1974.
- [Sa2002] M. Saba, C. Ciuti, S. Kundermann, J.L. Staehli, B. Deveaud, J. Bloch,  
V. Thierry-Mieg, R. André, Le Si Dang, G. Bongiovanni and A. Mura,  
phys. stat. sol. (a) **190** Nr. 2, 2002 p. 315.
- [Se2000] T. Seedorf, M. Cornelißen, K. Leonardi, D. Hommel, H. Selke and P.L. Ryder,  
J. Cryst. Growth **214/215**, 2000, p. 602.
- [Sk1998] M.S. Skolnick, T.A. Fisher and D.M. Whittaker,  
Sem. Sci. Tech. **13**, 1998, p. 645.
- [Ta1997] Ch. Tanguy, P. Lefebvre, H. Mathieu and R.J. Elliot,  
J. Appl. Phys. **82** Nr. 2, 1997, p. 798.
- [Ta2000] T. Tawara, H. Yoshida, T. Yogo, S. Tanaka and I. Suemune,  
J. of Crystal Growth **221** 2000, p. 699.
- [Tr1996] A. Tredicucci, Y. Chen, V. Pellegrini, M. Börger and F. Bassani  
Phys. Rev. B **54** Nr. 4, 1996, p. 3493.
- [Uu1995] P. Uusimaa, K. Rakenus, A. Salokatve and M. Pessa,  
T. Aherne, J.P. Doran, J. O'Gorman and J. Hegarty  
Appl. Phys. Lett. **67**, 1995, p. 2197.

- [We1971] S.H. Wemple and M. DiDomenico, Jr.  
Phys. Rev. B **3** Nr. 4, 1971, p. 1339.
- [We1992] C. Weisbuch, M. Nishioka, A. Ishikawa and Y. Arakawa  
Phys. Rev. Lett. **69** Nr. 23, 1992, p. 3214.
- [We2000] C. Weisbuch, H. Benisty and R. Houdré,  
J. of Luminescence **85**, 2000, p. 271.
- [Wo1995] K. Wolf, S. Jilka, A. Rosenauer, G. Schütz, H. Stanzl, T. Reisinger and W. Gebhardt,  
J. Phys. D **28**, 1995, p. A120.
- [Wo2000] D. Wolframm, D.A. Evans, D.I. Westwood and J. Riley  
J. Cryst. Growth **216**, 2000, p. 119.
- [Ya2002] Y. Yamamoto, F. Tassone and H. Cao,  
*"Semiconductor cavity quantum electrodynamics"*,  
Springer-Verlag Berlin Heidelberg, 2000.
- [Yo1995] H. Yokoyama and K. Ujihara,  
*"Spontaneous emission and laser oscillation in microcavities"*,  
CRC Press, Boca Raton, 1995.



# 7 Appendix

## List of publications

**A. Pawlis\***, O. Husberg, A. Kharchenko, K. Lischka and D. Schikora,  
*"Structural and optical investigations of ZnSe based semiconductor microcavities"*,  
phys. stat. sol. (a) **188** Nr. 3, 2001, p. 983.

**A. Pawlis\***, A. Kharchenko, O. Husberg, D.J. As, K. Lischka and D. Schikora,  
*"Large room temperature Rabi-splitting in a ZnSe/(Zn,Cd)Se semiconductor microcavity structure"*,  
Solid State Comm. **123**, 2002, p. 235.

**A. Pawlis\***, A. Kharchenko, O. Husberg, D.J. As, K. Lischka and D. Schikora,  
*"Large room temperature Rabi-splitting in II-VI semiconductor microcavity quantum structures"*,  
Microelect. J. **34**, 2003, p. 439.

**A. Pawlis\***, A. Kharchenko, O. Husberg, K. Lischka and D. Schikora,  
*"Preparation and properties of ZnSe/(Zn,Cd)Se multi quantum well structures for room temperature polariton emission"*,  
submitted to J. of Phys. Cond. Matter, 2003.

T. Frey\*, D.J. As, M. Bartels, A. Pawlis, K. Lischka, A. Tabata, J.R.L. Fernandez, M.T.O. Silva, J.R. Leite, C. Haug and R. Brenn,

*"Structural and vibrational properties of MBE grown cubic (Al,Ga)N/GaN heterostructures"*,

J. of Appl. Phys. **89** Nr. 5, 2001, p. 2631.

## Conference contributions

**A. Pawlis\***, D. Schikora and K. Lischka,

*"High reflectivity ZnS/YF<sub>3</sub> distributed Bragg-mirrors for microcavities in the green/blue spectral range"*,

DPG conference 2001, Hamburg.

**A. Pawlis\***, D. Schikora, O. Husberg, A. Kharchenko and K. Lischka,

*"II-VI semiconductor microcavities for light emission in the green spectral range"*,

II-VI conference 2001, Bremen.

**A. Pawlis\***, M. Bartels, A. Khartchenko, O. Husberg, D. Schikora and K. Lischka,

*"ZnSe/(Zn,Cd)Se semiconductor microcavities with dielectric Bragg mirrors of ZnS and YF<sub>3</sub>"* ,

DPG conference 2002, Regensburg.

---

## Acknowledgements

I would like to thank **Prof. Dr. Klaus Lischka** who gave me the opportunity to work in his group and for the valuable discussions during my PhD thesis.

The same gratitude goes to **Dr. Detlef Schikora** who supported me with all his knowledge in epitaxy. My thanks also goes to **Apl. Prof. Dr. Donat Josef As** for the profoundly discussions and his help regarding optical properties in semiconductors and semiconductor microcavities.

Furthermore my gratitude goes to **Prof. Le Se Dang**, **Prof. Gerard** and **Dr. Ballocci** during my stay at the University of Grenoble for their experience regarding the theory of strong coupling and optical phenomena in microcavities.

I would like to thank the PhD students **Christof Arens**, **Martin Bartels**, **Alexander Kharchenko**, **Olaf Husberg**, **Ulrich Köhler**, **Stefan Potthast** and **Jörg Schörmann** and the master degree student **Kathrin Friedrich** for their cooperation and helpful discussions.

My gratitude goes also to **Ralf Winterberg** for his help regarding the preparation of microcavities.

I would like to thank the "Optoelectronic" staff namely **Irmgard Zimmermann** and **Bernard Volmer** for their help in bureaucratic things and **Siegfried Igges** for the enormous and excellent technical engagement and support during the set-up of the new MBE machine.

Furthermore my gratitude goes to our collaborators **Prof. Yamamoto** and **Dr. Weihs** from Stanford University for their valuable work and contributions.

Moreover I have to thank **Andrea Bartels** for her love and encouragement she gave me during the "hot-phase" of my PhD work.

Last but not least I would like to express thanks to my parents **Monika Pawlis** and **Gunter Pawlis** for their love, encouragement and financial support as well as to my best friend **Uwe Klingeberg** for encouragement and some good advice in bad days of my work.

This work was supported by the European Network Project "Photon Mediated Phenomena", HPRN-CT-2002-00298.